SYNTHESIS AND CHARACTERIZATION OF PRUSSIAN BLUE ANALOGUE AND LAYERED TRANSITION METAL OXIDE CATHODES FOR HIGH PERFORMANCE SODIUM-ION BATTERIES

CHEN YUNCAI

FACULTY OF SCIENCE
UNIVERSITI MALAYA
KUALA LUMPUR

2023

SYNTHESIS AND CHARACTERIZATION OF PRUSSIAN BLUE ANALOGUE AND LAYERED TRANSITION METAL OXIDE CATHODES FOR HIGH PERFORMANCE SODIUM-ION BATTERIES

CHEN YUNCAI

THESIS SUBMITTED IN FULFILMENT OF THE REQUIREMENTS FOR THE DEGREE OF DOCTOR OF PHILOSOSPY

FACULTY OF SCIENCE
UNIVERSITI MALAYA
KUALA LUMPUR

2023

UNIVERSITY OF MALAYA

ORIGINAL LITERARY WORK DECLARATION

Name of Candidate: **CHEN YUNCAI**

Matric No: **17221263**

Name of Degree: **DOCTOR OF PHILOSOPHY**

Title of Project Paper/Research Report/Dissertation/Thesis ("this Work"):

SYNTHESIS AND CHARACTERIZATION OF PRUSSIAN BLUE ANALOGUE AND LAYERED TRANSITION METAL OXIDE CATHODES FOR HIGH PERFORMANCE SODIUM-ION BATTERIES

Field of Study:

PHYSICS

I do solemnly and sincerely declare that:

(1) I am the sole author/writer of this Work;
(2) This Work is original;
(3) Any use of any work in which copyright exists was done by way of fair dealing and for permitted purposes and any excerpt or extract from, or reference to or reproduction of any copyright work has been disclosed expressly and sufficiently and the title of the Work and its authorship have been acknowledged in this Work;
(4) I do not have any actual knowledge nor do I ought reasonably to know that the making of this work constitutes an infringement of any copyright work;
(5) I hereby assign all and every rights in the copyright to this Work to the University of Malaya ("UM"), who henceforth shall be owner of the copyright in this Work and that any reproduction or use in any form or by any means whatsoever is prohibited without the written consent of UM having been first had and obtained;
(6) I am fully aware that if in the course of making this Work I have infringed any copyright whether intentionally or otherwise, I may be subject to legal action or any other action as may be determined by UM.

Candidate's Signature Date: 16/Aug/2023

Subscribed and solemnly declared before,

Witness's Signature Date:

Name:

Designation:

SYNTHESIS AND CHARACTERIZATION OF PRUSSIAN BLUE ANALOGUE AND LAYERED TRANSITION METAL OXIDE CATHODES FOR HIGH PERFORMANCE SODIUM-ION BATTERIES

ABSTRACT

Energy storage must be applied to these renewable energies, such as solar, wind, and tidal energy, due to their intermittent nature. The sodium-ion battery is one of the most competitive candidates due to its low cost and abundant availability of sodium. In this study, we focus on the cathode materials, namely Prussian blue analogues and P2-type transition metal oxides. Na-rich PB-4M was synthesized by controlling the concentration of Na^+ ions during the synthesis process. PB-C with the cage-like porous structure was synthesized via the re-heating method and acid etching. P2-type transition metal oxide $Na_{0.67}(Li_{0.5}Mg_{0.5})_{0.1}(Ni_{0.33}Mn_{0.67})_{0.9}O_2$ (LMNM), with Li/Mg co-substitution, was synthesized via a solid-state method. TGA, (in-situ) XRD, FTIR, and SEM, GITT, CV were used to investigate the materials. PB-4M exhibited a specific capacity of 130 mAh/g at RT and 120 mAh/g at 80 ℃. At 80 ℃, PB-4M could still deliver a reversible specific capacity of 57 mAh/g at 2 C after 500 charge-discharge cycles. PB-C exhibited a specific capacity of 112 mAh/g at 0.2 C and 97 mAh/g at 10 C and no obvious capacity fading, with more than 80% capacity retention after the 1000th cycle. LMNM exhibited enhanced cycling performance with a reversible capacity of 127 mAh/g and a capacity retention of 75% over 100 cycles at 0.5 C.

Keywords: Sodium-ion batteries, cathode materials, Prussian blue analogue, transition metal oxide.

SINTESIS DAN CIRI-CIRI ANALOG PRUSSIAN BLUE DAN OKSIDA LOGAM PERALIHAN BERLAPIS SEBAGAI KATOD UNTUK BATERI NATRIUM-ION BERPRESTASI TINGGI

ABSTRAK

Penyimpanan tenaga perlu digunakan untuk tenaga boleh diperbaharui, seperti tenaga suria, angin dan pasang surut, kerana sifat intermiten mereka. Bateri ion natrium adalah salah satu calon yang paling kompetitif kerana kosnya yang rendah dan ketersediaan natrium yang melimpah. Dalam kajian ini, kami memberi tumpuan kepada bahan katod, iaitu analog Prussian blue dan oksida logam peralihan jenis PB-4M yang kaya dengan Na telah disintesis dengan mengawal kepekatan ion Na^+ semasa proses sintesis. PB-C dengan struktur berliang seperti sangkar telah disintesis melalui kaedah pemanasan semula dan goresan asid. Oksida logam peralihan jenis P2 $Na_{0.67}(Li_{0.5}Mg_{0.5})_{0.1}(Ni_{0.33}Mn_{0.67})_{0.9}O_2$ (LMNM), dengan penggantian bersama Li/Mg, telah disintesis melalui kaedah keadaan pepejal. TGA, XRD (in-situ), FTIR, dan SEM, GITT, CV digunakan untuk menyelidiki bahan-bahan tersebut. PB-4M menunjukkan kapasiti spesifik 130 mAh/g pada suhu bilik dan 120 mAh/g pada suhu 80 °C. Pada suhu 80 °C, PB-4M masih dapat memberikan kapasiti spesifik bolehbalik sebesar 57 mAh/g pada 2 C selepas 500 kitaran cas-discas. PB-C menunjukkan kapasiti spesifik 112 mAh/g pada 0.2 C dan 97 mAh/g pada 10 C tanpa menunjukkan penurunan kapasiti yang jelas, dan mengekalkan retensi kapasiti lebih dari 80% selepas kitaran ke-1000. LMNM menunjukkan prestasi kitaran yang lebih baik dengan kapasiti bolehbalik 127 mAh/g dan mengekalkan retensi kapasiti 75% lebih daripada 100 kitaran pada 0.5 C.

Kata Kunci: Bateri ion natrium, bahan katod, analog Prussian blue, oksida logam peralihan.

ACKNOWLEDGEMENTS

My life as a PhD student will soon come to an end, and I would like to take this opportunity to express my heartfelt gratitude to all the individuals who have supported and accompanied me throughout these three years.

First and foremost, I am immensely grateful to my supervisor, Dr. Woo Haw Jiunn, who has provided invaluable guidance and assistance in both my personal and research endeavors. His friendly, tolerant, and gentle nature has made a significant impact on my journey. I genuinely wish him a wonderful life and a happy family. I would also like to extend my deepest appreciation to the members of the research group, including Professor Dr. Abdul Kariem Mohd Arof, Associate Professor Dr. Mohd Hamdi Ali, Dr. Teo Liping, Dr. Lee Yap Chen, Dr. Kim Cheng Kim, and others. We have shared countless joyful and exciting memories during my master's and PhD studies. Additionally, I would like to express my sincere thanks to Professor Deng Yonghong, Professor Wang Jun, and their respective team members. During my visiting period at the Southern University of Science and Technology, they provided invaluable support and guidance.

I am also filled with immense gratitude towards my beloved wife, Wen Min. Despite dedicating an extensive amount of time to my research, she has consistently encouraged me to complete my PhD. Despite my many shortcomings, she has remained by my side. Moreover, during my PhD journey, we were blessed with the arrival of our adorable son, Chen Zhiyue, affectionately known as "little battery." With the companionship of my wife and son, the once monotonous research life has become vibrant and colorful.

Finally, I would like to express my deepest gratitude to my parents and extended family for their unwavering support throughout this entire journey. Their love, encouragement, and belief in my abilities have been the pillars of strength that kept me going.

TABLE OF CONTENTS

LIST OF FIGURES

LIST OF TABLES

LIST OF SYMBOLS AND ABBREVIATIONS

Al	aluminum
Ar	argon
C	carbon
Cu	copper
EDS	energy dispersive spectroscopy
EV	electric vehicle
FESEM	Field Emission Scanning Electron Microscope
FTIR	Transform Infrared Spectroscopy
GCD	Galvanostatic Charge/Discharge
h	hour
H	hydrogen
H.S.E	hydrogen standard electrode
He	helium
HRTEM	High Resolution Transmission Electron Microscope
ICP-MS	Inductively Coupled Plasma Mass Spectrometry
IR	infrared radiation
Li	Lithium
Li/MoS_2	Lithium/Molybdenum disulfide
LIB	lithium-ions battery
LiCoO2	Lithium cobalt oxide
LMNM	$Na_{0.67}[(Li_{0.05}Mg_{0.05}(Ni_{0.33}Mn_{0.67})_{0.9}]O_2$
LNM	$Na_{0.67}[(Li_{0.1}(Ni_{0.33}Mn_{0.67})_{0.9}]O_2$
M	mole per liter
MNM	$Na_{0.67}[(Mg_{0.1}(Ni_{0.33}Mn_{0.67})_{0.9}]O_2$

N	nitrogen
Na	Sodium
NaCl	Sodium chloride
TMO	Transition metal oxide
Ni-Cd	Nickel-cadmium
Ni-MH	Nickel-metal hydride battery
NPD	Neutron Profile Depth
PB	Prussian blue
PB-A	Prussian blue analogue
pH	potential of hydrogen
PVP	Poly(vinylpyrrolidone)
TGA	Thermogravimetric Analysis
TM	transition metal
vs	versus
Zn-Mn	Zinc-manganese

CHAPTER 1: INTRODUCTION

1.1 Research Background

Nowadays, non-renewable power sources, such as oil, gas and coal, have become the main energy in our daily lives. (X.-B. Cheng, Zhao, Yao, Liu, & Zhang, 2019; Q. Liu et al., 2020; Syed Mohd Fadzil, Woo, Azzahari, Winie, & Kufian, 2023; Zeng et al., 2019) However, with the high-speed development of our society, the demand for energy is increasing rapidly. The overuse of these carbon-based power sources brings significant environmental issues, such as excess green-house gas emissions, global warming and the enlarging ozone hole. (Meinshausen et al., 2009; Yabuuchi, Kubota, Dahbi, & Komaba, 2014) Thus, it is critical to develop renewable power sources such as wind, solar, tidal and nuclear energy. However, most of these renewable power sources are intermittent. The application of energy storage systems is very important to act as the mediator between intermittent energy and power demand. (Kerman, Luntz, Viswanathan, Chiang, & Chen, 2017; B. Liu, Zhang, & Xu, 2018; Winter, Barnett, & Xu, 2018)

Among energy storage systems, electrochemical energy storage systems such as secondary batteries are widely used methods because of their high energy density, stability, and mature technology. (X.-B. Cheng, Zhang, Zhao, & Zhang, 2017; Y. Guo, Li, & Zhai, 2017; X. G. Han et al., 2017) So far, lead-acid batteries, sodium-sulfur batteries and lithium-ions batteries have been the commercial applications. (Cabana, Monconduit, Larcher, & Palacín, 2010; Gopalakrishnan et al., 2016; X. Yang & Rogach, 2020) The oldest secondary battery, the lead-acid battery, was applied in the 18th century, and continues to be used today. Compared to other secondary batteries, the energy density of the lead-acid battery is low, and its product life is short. Also, lead is a heavy metal which can cause environmental pollution. The sodium-sulfur battery is another choice for energy storage, but the operation temperature of more than 300 ℃ might raise safety

concerns. The most wildly used secondary battery is lithium-ion battery (LIB) with the advances of high-energy density and long product life. (W. Lee et al., 2020) LIBs started to be used in 1980s by SONY company on portable devices such as headphones and laptops. With the development of technology, LIBs are now applied in large-scale systems such as electric vehicles (EVs), and the demand for LIBs has increased quickly in recent years, leading to the depletion of Li and related resources. According to an early report, the consumption of Li might double from 2012 to 2030. (H. Yoshida et al., 2014)

Na is in the same group as Li, meaning that the characteristics of Na are similar to Li. Additionally, the reserve of Na is abundant and exists in sea water, and the price of Na salt is low. Thus, sodium-ion batteries (SIBs) should be a promising alternative to LIBs. In the battery level, the working mechanism of SIBs is similar with that of LIBs. It can be described as a "rocking batteries" concept, which is the same as LIBs. (Guyomard & Tarascon, 1994; Megahed & Scrosati, 1994) A SIB consists of a cathode, anode, electrolyte, separators and a case. Diagram 1.1 shows the working process during charge/discharge. The cathode, separators and anode are stacked in an orderly manner with the electrolyte, and a case wraps all the components. During the charge process, Na^+ ions move from the cathode side to the anode side through the separator, facilitated by the Na conductivity of the electrolyte. At this moment, the cell is in high potential state, storing electrochemical energy. During the discharge process, Na^+ ions move from the anode to the cathode, releasing the electrochemical energy. The reaction equations are shown in Equation (**1.1)** - Equation (1.3).

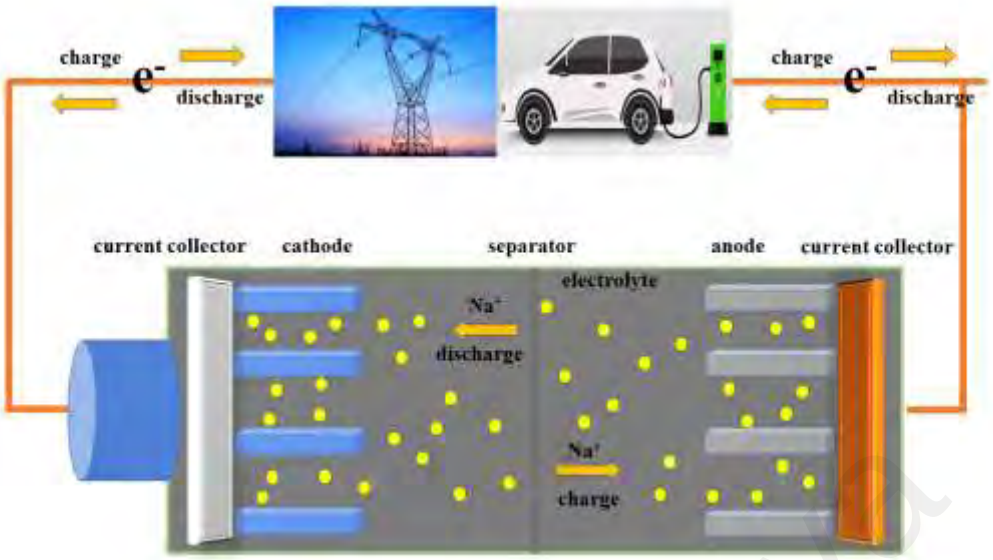

Diagram 1.1 The diagram working process during the charge/discharge of SIBs.

Cathode side: $Na_xMO_2 \rightleftharpoons Na_{1-x}MO_2 + xNa^+ + xe^-$ **(1.1)**

Anode side: $C + yNa^+ + ye^- \rightleftharpoons Na_yC_n$ **(1.2)**

Full cell: $Na_xMO_2 + C \rightleftharpoons Na_{x-y}MO_2 + Na_yC_n$ **(1.3)**

1.2 Problem Statement

Compared to LIBs, SIBs have some advantages such as low cost and abundant reserves. However, SIBs also have their disadvantages. The energy density of SIBs is still not high enough. The first reason is that the atomic mass of Na^+ ions is 23 while that of Li^+ ions is only 7, which means that the movement of Na^+ ions is harder than that of Li^+ ions. The second reason is that the potential of Na^+ ions versus the hydrogen standard electrode (H.S.E) is higher than that of Li^+ ions, which means the working potential of SIBs is lower than that of Li^+ ion. As a result, the energy density of SIBs is lower than that of LIBs. To improve the energy density of SIBs, more studies should be carried out.

Furthermore, unlike LIBs, SIBs have only recently caught people's attention, and the mechanism of SIBs, especially on the cathode side, is still not completely clear. Thus, the

cathode material for commercial application has not been confirmed. The two main cathode candidates are Prussian blue analogue (PBA) and Na layer oxides (NaTMO,). For PBA, the presence of interstitial water and the low specific capacity become barriers to its commercial application. As for NaTMO, especially the P2-type NaTMO, it is a potential cathode candidate due to its high specific capacity. However, it is unstable at high voltage. In this study, these two materials will be the objects of investigation.

1.3 Objectives of the Research

In view of the problem descried above, the objectives of this work include.

1. To synthesize PBA with surface modification and P2-type TMO with elemental substitution.
2. To investigate the structural and morphological properties of the synthesized PBA and P2-type TMO.
3. To evaluate the electrochemical performance of SIBs based on the synthesized PBA and P2-type TMO as cathode materials.

1.4 Dissertation Organization

This thesis comprises 7 chapters, including an introduction, literature review, experimental methods, results & discussion, and conclusions & future work.

Chapter 1 serves as the introduction of this thesis, encompassing the research background, problem statement, objective of the research and dissertation organization.

Chapter 2 reviews and discusses the electrode materials for SIBs. Furthermore, advanced characterization techniques are also examined and discussed in this chapter.

Chapter 3 comprises the experimental methods. PBA was prepared using the coprecipitation synthesis method, while P2-type TMOs were synthesized using a high-

temperature solid-state method. In addition, the characterization methods for these two materials are presented. Since all the samples will be used as the cathode materials for SIBs, the electrochemical characterization methods are also presented.

Chapters 4-6 of this thesis form the main body, discussing the structure, morphology, electrochemical performance, and other findings of two types of PBAs and P2-type TMO. The research on PBAs focuses on improving electrochemical properties and performance through component regulation and morphology modification. For P2-type TMO, modifying its structure through element substitution has an impact on its structure, morphology, and electrochemical performance.

Chapter 7 serves as the final chapter of this thesis, containing the conclusion of this work and recommendations of future research.

CHAPTER 2: LITERATURE REVIEW

2.1 Introduction

LIBs have become the most widely use secondary batteries. (Y. Li et al., 2022) Due to the increasing demand of LIBs, the LIBs related row material is in short supply and the price of these row materials has increased drastically over last decade. The alternative candidate of LIBs is necessary and after a lot of research, SIBs seem be the first choice (Delmas, 2018). The similar working mechanism with LIBs, abundance of Na resources, low cost and non-toxicity make SIBs potential candidates to replace a portion of the applications currently relaying on LIBs. In the 1970s, the energy crisis compelled the adoption of renewable energies. In addition, portable devices began to be widely used in daily life. As a result, the traditional secondary batteries would not meet the high energy density demand. Although Li-based batteries and Na-based batteries were proposed around the same time as energy storage devices. LIBs emerged victorious in this "war" due to the widespread adoption of inventions like application of $LiCoO_2$ and graphite. In recent year, with the increasing demand of secondary batteries and the limiting supply of LIBs, SIBs have once again come into focus. PBA and P2-type TMO have become the most popular candidate of cathode material of SIBs (Q. Liu et al., 2020; Peng et al., 2022; Shi et al., 2022; Tan et al., 2022; Vanaphuti et al., 2022). This chapter presents a brief history of batteries, including LIBs and SIBs. It is followed by an introduction to electrode materials, including various types and methods of synthesis. Lastly, this chapter will discuss the importance of in-situ characterization in this study, which will be covered in the final section.

2.2 Development of Batteries

Energies play a key role in our daily life and have propelled the society into 'Age of Civilization'. The primary application of energies is the release of heat, such as fire and

the thermal radiation. Furthermore, the application of energies has evolved to other forms, such the use of waterwheel. The mechanism of batteries involves the conversion of energy into electrochemical form. In 1800, the first battery was introduced by Volt, known as the Volt reactor. Since then, a series of batteries have been developed, with some being abandoned over time while others continue to be utilized to this day. In 1836, the Daniell battery was used as a power source for signal lights. In 1839, Grove introduced the concept of the air battery. In 1860, G. Planté invented the lead-acid battery, which has been used as a starting battery for its high discharge rate performance ever since. In 1868, Leclanché developed the Zn-Mn dry battery. The lead-acid battery was commercialized in 1882. In 1888, the Zn-Mn dry battery was also introduced to the market. J. Waldmar invented the Ni-Cr battery in 1899 and the Ni-Fe battery in 1901. During World War II, the alkaline Zn-Mn cell battery was utilized. In the 1980s, Ni-Cd batteries gained widespread use, followed by the application of Ni-MH batteries in 1985. The energy crisis has propelled the search for alternatives to fossil fuels, but many renewable energy sources remain intermittent. Therefore, there is a growing need for high-energy density storage systems.

Lithium, Li as the lightest metal in the periodic table, has been proposed as an electrode material for rechargeable batteries. However, the high reactivity of Li metal has hindered its widespread application. In the 1970s, lithium primary batteries were introduced, while research on secondary batteries was underway. In 1980, Goodenough suggested $LiCoO_2$ as the cathode material for secondary lithium batteries, and in 1985, carbon was proposed as an anode material. These developments laid the foundation for lithium-ion batteries (LIBs). In 1986, the commercialization of Li/MoS_2 batteries took place, but it was discontinued due to safety concerns. In 1991, Sony successfully introduced LIBs with a $LiCoO_2$ cathode, carbon anode, and LiPF6@EC/DEC electrolyte, marking a significant achievement in the field (Hwang, Myung, & Sun, 2017).

When it comes to sodium-ion batteries (SIBs), the challenges of selecting suitable electrode materials and the unsatisfactory electrochemical performance have hindered their commercialization, keeping SIBs at the research level. The research on SIBs was initiated in the last century in response to the urgent need brought about by the energy crisis. Na_xTMO (where TM = Co, Ni, Cr, Mn, Ti, Nb, etc.) has been used as a cathode material for SIBs. Delmas proposed the nomenclature known as Na_xTMO (O3/P2), based on the TM stacking (Delmas, Fouassier, & Hagenmuller, 1980). In 1987, Delmas reported a SIBs cathode material with a NASICON structure, $Na_3TM(PO_4)_3$ (where TM = Ti, V, Cr, Fe, etc.), as well as $NaTi_2(PO_4)_3$ (Delmas, Cherkaoui, Nadiri, & Hagenmuller, 1987). Despite the focus on commercializing LIBs, the research on SIBs has never stopped. Dahn introduced a P2-type SIB cathode material, $Na_2/3Ni_{1/3}Mn_{2/3}O_2$. With the ever-increasing demand for LIBs, there is now an urgent need to explore alternative candidates. As a result, SIBs have regained attention and seen significant developments since 2010. Resources of Na and other materials such as Mn, Fe, Al, and Ni are more abundant compared to the raw materials used in LIBs. Consequently, the price of these raw materials is relatively low. Moreover, aluminum (Al) can be used as the anode current collector for SIBs, whereas copper (Cu) is required for LIBs due to the reaction between lithium and aluminum at low potentials. The use of Al as the current collector not only reduces the weight of the cell but also lowers the cost. Furthermore, the manufacturing technology for SIBs is similar to that of LIBs, allowing most production lines designed for LIBs to be repurposed for SIBs. The cost-effectiveness of SIBs positions them as a promising alternative to LIBs (Shi et al., 2022) .

2.3 Anode Materials for SIBs

SIB anode materials can be devised into four kinds: carbon-based materials, Ti-based materials, organic materials and alloying materials. Carbon-based materials typically refer to amorphous carbon with a low standard hydrogen electrode (S.H.E.) potential,

high specific capacity, minimal volume change, good cycling performance, and ease of synthesis. Currently, they are the most promising anode candidates for SIBs, with production reaching a medium-scale level. Organic materials offer advantages such as multiple electrochemical activity, low cost, environmental friendliness, and compositional diversity. However, they suffer from drawbacks such as low electron conductivity and solubility in organic solvents (Q. Zhao, Lu, & Chen, 2016). Metal-based materials encompass both elemental metals and alloys (J. Zhao et al., 2017). These anode materials exhibit high specific capacity but are prone to large volume changes and poor cycling performance (Chevrier & Ceder, 2011; C. Yang, Xin, Mai, & You, 2021).

2.3.1 Carbon-Based Anode Materials

2.3.1.1 Graphite

Graphite is used as the commercial anode for LIBs, but it is not suitable for use in SIBs due to its low sodiated potential and specific capacity. Based on the thermodynamic calculation, the interaction force between Na^+ ions and graphite is very weak (Rinaldo et al., 2015). So, it is hard to form stable Na-graphite composite, leading in a low specific capacity of graphite for Na^+ ions storage chemistry. Nevertheless, some studies have been conducted to explore the Na^+ storage capabilities of graphite. By incorporating ethers such as DEGDME (Lao et al., 2017), the Na^+ storage performance was improved to some extent. However, the specific capacity remained too low for practical application in SIBs. Additionally, ethers have a relatively low decomposition voltage, which restricts the working electrochemical window of SIBs and limits the use of high-voltage cathode materials.

2.3.1.2 Amorphous Carbon

Amorphous carbon does not exhibit a periodic arrangement of carbon atoms. While certain regions of amorphous carbon may show some crystal-like characteristics, its

overall crystallinity at a macro-level is low. Amorphous carbon can be categorized into two types: hard carbon and soft carbon, based on their graphitization ability. After high-temperature heat treatment (typically above 2800 ℃), certain types of amorphous carbon may undergo long-range ordering and transform into a graphite structure, known as soft carbon. Other types of amorphous carbon, referred to as hard carbon, do not undergo this transformation. Prior to heat treatment, these two types of amorphous carbon exhibit similar properties (Irisarri, Ponrouch, & Palacin, 2015; Y. Li, Hu, Titirici, Chen, & Huang, 2016; K. Wang et al., 2019).

2.3.1.3 The Na^+ Ions Storage Mechanism of Carbon-Based Anode Materials

Like LIBs, the sodium-ion storage mechanism in amorphous carbon involves the adsorption of Na^+ ions. However, due to thermodynamic constraints, it is difficult for Na^+ ions to insert into the carbon layers of graphite. In addition, the low surface area of graphite limits the adsorption of Na^+ ions, resulting in a very low specific capacity. In 2000, Stevens et al. (Stevens & Dahn, 2000) reported a hard carbon material derived from pyrolytic glucose. Their research revealed a plateau at low voltage and a curve at high voltage, indicating the presence of two distinct Na^+ storage mechanisms in hard carbon. They proposed the "house of cards" model to explain this mechanism, suggesting that numerous microcrystals within the hard carbon structure allow Na^+ ions to both insert into the microcrystals and adsorb onto the surfaces and void spaces between them. However, the precise corresponding mechanism remains unclear.

Dahn et al. proposed an “intercalation–adsorption” model, which is shown in Figure 2.1(a) to explain the behavior of Na^+ ions in hard carbon (Stevens & Dahn, 2000; Zuo et al., 2020). According to this model, the high voltage sloping region corresponds to the insertion of Na^+ ions into the carbon layer. As the Na^+ ions are inserted, the voltage decreases, and the plateau observed at low voltage represents the adsorption of Na^+ ions.

While this model provides some insights into the movement of Na^+ ions, there are still certain unexplained phenomena. For instance, low-temperature pyrolyzed hard carbon with numerous micropores exhibits a single curve without a plateau, and as the number of micropores decreases with increasing pyrolysis temperature, the specific capacity during the plateau increases (Qiu et al., 2017) .

The second model is the "adsorption-intercalation" model, as shown in Figure 2.1(b). Cao et al. introduced a polyaniline (PANI) pyrolyzed hard carbon and proposed an opposite viewpoint to the "insertion-filling" model. In-situ XRD analysis revealed a shift in the (002) pattern at low voltage (0.0–0.1 V), indicating a change in layer spacing, which corresponds to the insertion of Na^+ ions (NaC_x). As the pyrolysis temperature increased and the void spaces decreased, the specific capacity during the plateau phase increased (Y. Cao et al., 2012).

The third model is the "absorption-voids filling" mechanism. Hu et al. investigated hard carbon tubes using ex-situ TEM and observed no change in layer spacing in different state of charge, suggesting the absence of an insertion process during charge-discharge cycles. Thus, they proposed the "absorption-voids filling" mechanism. Furthermore, Xu et al. filled the hard carbon with sulfur (S) without any structural changes, causing the plateau voltage to vanish and reappear at approximately 1.4 V. By increasing the carbonization temperature to reduce the number of voids, the specific capacity decreased, indicating a relationship between the specific capacity and the number of voids (Bai et al., 2018).

The last model is the "adsorption-intercalation-voids filling" mechanism. Ji et al. utilized galvanostatic intermittent titration technique (GITT) to investigate ion transfer (Bommier, Surta, Dolgos, & Ji, 2015). The diffusion coefficient observed during the curve phase was found to be higher than that during the plateau phase and exhibited a

rapid increase at a voltage of 0.05 V, suggesting the presence of an additional Na^+ ions storage mechanism below 0.05 V. Therefore, the "adsorption-intercalation-voids filling" mechanism was proposed. It involves absorption behavior at high voltage, followed by intercalation behavior and voids filling behavior below 0.05 V. Various studies present different perspectives on the Na^+ ions storage mechanism, and a unified view has not yet been established.

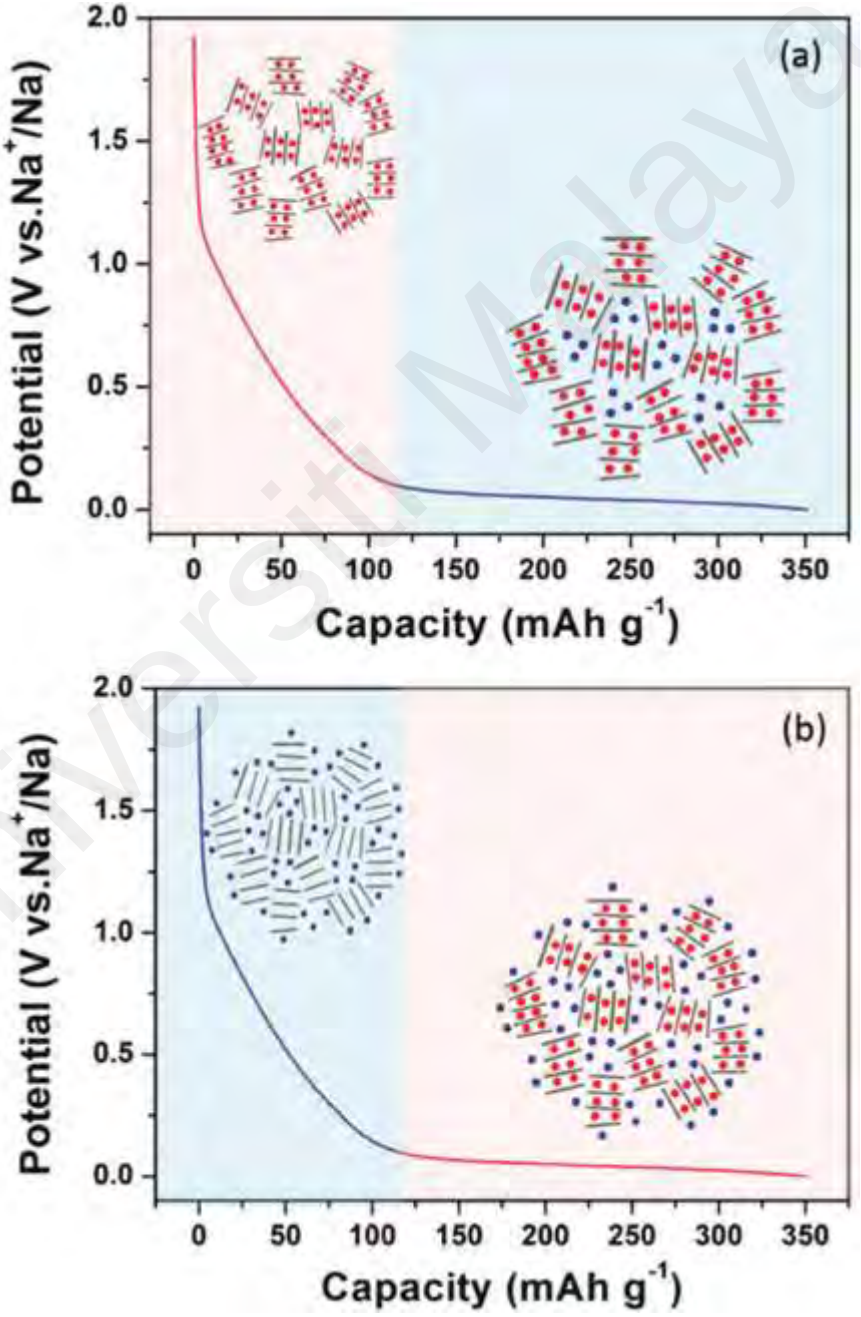

Figure 2.1: Schematic illustration of the mechanisms for Na-ion storage in hard carbon: (a) "intercalation–adsorption" mechanism; (b) "adsorption–intercalation" mechanism (Qiu et al., 2017).

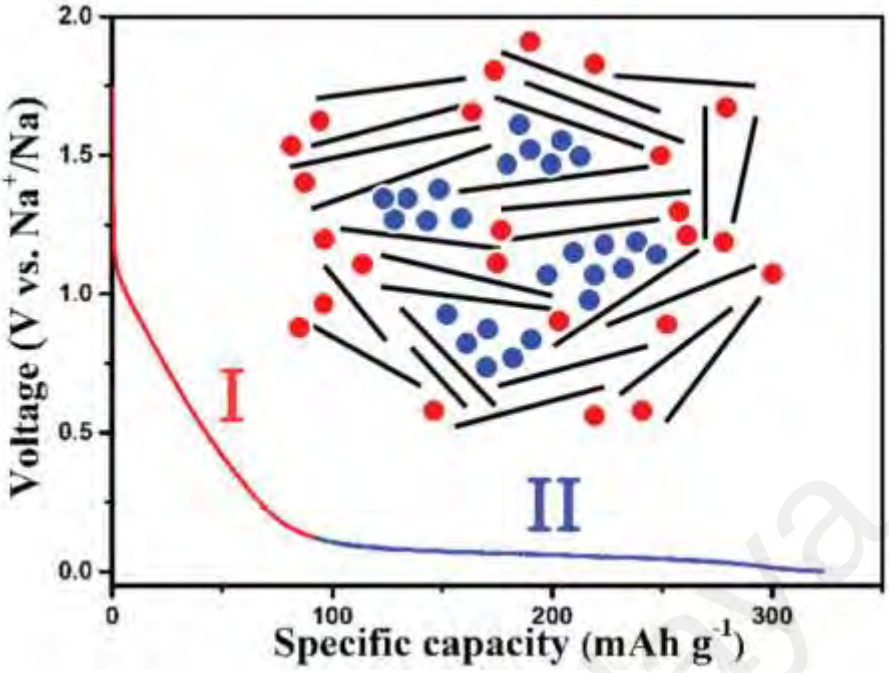

Figure 2.2: schematic of "adsorption-voids filling" mechanism (Y. Li et al., 2016).

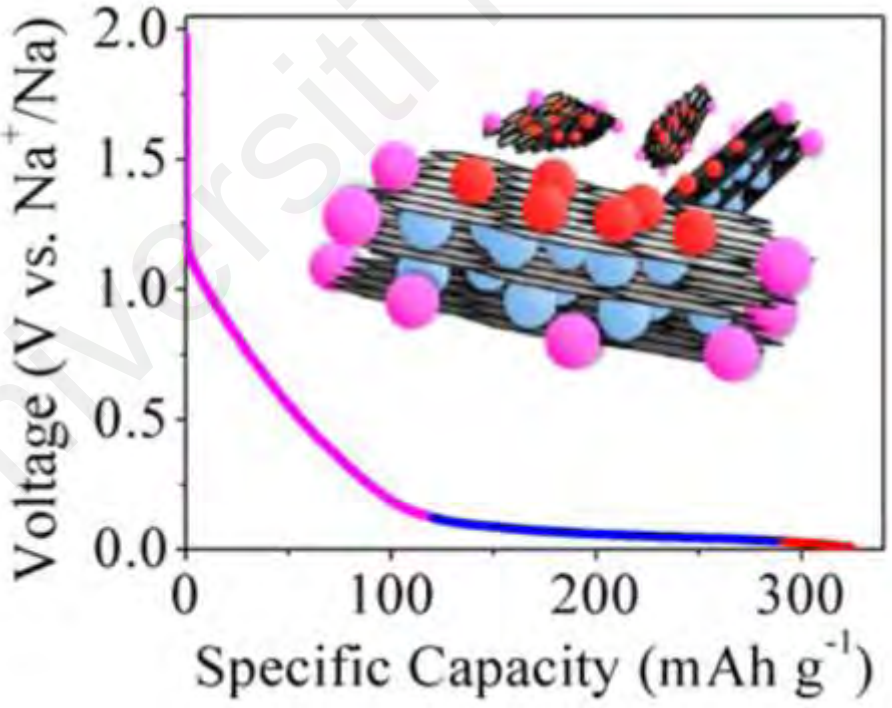

Figure 2.3: schematic of "adsorption- intercalation-voids filling" mechanism (Bommier et al., 2015).

2.3.2 Ti-Based Materials

$Li_4Ti_5O_{12}$ is known for its exceptional cycling durability and serves as an anode material in LIBs with an impressively long lifespan (B. Zhao, Ran, Liu, & Shao, 2015). Similarly, Ti-based materials show great potential to be electrode materials for SIBs.

$Na_2Ti_3O_7$ possesses a monoclinic structure with a space group of P21/m. Within this structure, a titanium (Ti) atom is surrounded by six oxygen (O) atoms, forming a Ti-O octahedron (TiO_6). Furthermore, three (TiO_6) octahedra combine to form a single unit. Furthermore, three (TiO_6) octahedra combine to form a single unit (Pan et al., 2013). These units are interconnected at the top to create a layered structure, with Na^+ ions occupying the space between the layers. In 2011, Palacin et al. reported the Na^+ ion storage ability of $Na_2Ti_3O_7$ with a potential of about 0.3 V and a specific capacity of 200 mAh/g (Senguttuvan, Rousse, Seznec, Tarascon, & Palacín, 2011).

$Li_4Ti_5O_{12}$ has been applied in high-rate LIBs due to the "zero-strain" factor. $Li_4Ti_5O_{12}$ has a spinel structure with the space group $Fd\bar{3}m$. O^{2-} is located in 32e to form the face-centered cubic, while some Li^+ is located in 8a and Li^+/Ti^{4+} is located in 16d. Thus, the formula is $[Li]8a[Li_{1/3}Ti_{5/3}]16d[O_4]32e$. $Li_4Ti_5O_{12}$ was also applied as an SIB anode material by Hu et al., exhibiting a specific capacity of about 145 mAh/g with 3 Na+ ion insertions/desertions (L. Zhao, Pan, Hu, Li, & Chen, 2012).

$Na_{0.66}[Li_{0.22}Ti_{0.78}]O_2$ with the space group of $P6_{3/mmc}$, is a layered oxide. Li atoms and Ti atoms occupy the transition metal layer, and Na atoms occupy the 2b and 2d sites to form a triangular prism. The specific capacity of $Na_{0.66}[Li_{0.22}Ti_{0.78}]O_2$ is 116 mAh/g, and the voltage is about 0.75 V (Y. Wang et al., 2013).

Other Ti-based layer oxides for SIB anodes, such as $Na_{0.6}[Cr_{0.6}Ti_{0.4}]O_2$, (Y. Wang, Xiao, Hu, Avdeev, & Chen, 2015) with similar radii but different redox voltages between

Cr and Ti, result in Na/vacancy disorder, leading to satisfactory cycling and rate performance. Ti-based phosphates can also serve as anode materials for SIBs. $NaTi_2(PO_4)_3$ with the NASICON structure is widely studied due to its structural stability (Mu et al., 2016). The open framework allows easy migration of Na^+ ions, but due to the low ionic conductivity, the rate performance is poor.

2.3.3 Organic Materials

In comparison to inorganic anode materials for SIBs, organic materials offer several advantages such as low cost, adjustable composition, multiple active sites, and rapid ion transport. However, the low electrical conductivity of many organic materials necessitates the addition of conductive carbon to the electrode, thereby reducing the energy density of the electrode. Additionally, organic materials tend to have high solubility, which can result in electrode instability.

The hydroxyl group (C=O) serves as the active site for SIBs, facilitating the storage of Na^+ ions. Hu et al. introduced a carboxylate-based organic material ($Na_2C_8H_4O_4$), disodium terephthalate, with two active Na^+ sites. To enhance the Na^+ ion storage performance, the research group applied an Al_2O_3 layer coating on the electrode surface. This material demonstrated a low Na^+ insertion voltage of 0.29 V and a reversible capacity of 250 mAh/g (L. Zhao, Zhao, et al., 2012). Furthermore, they also prepared a $Na_2C_6H_2O_4$/CNT nanocomposite via a spray drying method. The resulting material exhibited a reversible capacity of 259 mAh/g and 142 mAh/g at 7 C (X. Wu et al., 2015). Armand et al. reported the synthesis of several polymeric Schiff bases through a simple condensation reaction involving aromatic dialdehydes and diamines. These Schiff bases displayed a remarkable reversible specific capacity of 350 mAh/g (Castillo-Martínez, Carretero-González, & Armand, 2014).

2.3.4 Alloy Materials

Similar to the alloying anode materials used in LIBs, alloying materials such as Sn, Sb, and P exhibit high specific capacities in SIBs. However, these materials face similar challenges as those encountered in LIBs, including significant volume changes and capacity fading. As a result, many research efforts were directed aiming to address and mitigate these volume change-related issues.

The theoretical specific capacity of Sn is 847 mAh/g, making it a promising candidate as the anode material for SIBs. However, the mechanism of Sn intercalation remains unclear. Chevrier and Ceder pointed out that there were 4 plateaus below a certain voltage, corresponding to the product of $NaSn_5$, NaSn, Na_9Sn_4 and $Na_{15}Sn_4$ (Chevrier & Ceder, 2011). Conversely, Ellis suggested that these plateaus represent $NaSn_3$, NaSn, Na_9Sn_4 and $Na_{15}Sn_4$ (Ellis, Hatchard, & Obrovac, 2012).

Sb, with a theoretical specific capacity of 660 mAh/g, displays an intercalation potential of 0.52 V vs. Na^+/Na. Throughout the discharge process, Na^+ ions react with Sb to form Na_xSb, followed by the formation of Na_3Sb upon further reaction with Na^+. During the charge process, Na_3Sb is converted back to Sb (Darwiche et al., 2012).

As for P, it is commonly represented by red phosphorus. P exhibits an impressive theoretical specific capacity of 2596 mAh/g, with an intercalation potential of approximately 0.4 V vs. Na^+/Na. The reaction process for P is akin to that of Sb, where Na and P combine to form Na-P during discharge, and subsequently transition to Na_3P. During the charge process, Na_3P is converted back to P (Marbella et al., 2018).

2.4 Cathode Materials for SIBs

Cathode materials play a pivotal role in the development of SIBs. Currently, research efforts primarily focus on transition metal oxides (TMO), Prussian (PB), and polyanion materials as potential cathode candidates. TMOs are particularly appealing due to their high specific capacity, favorable Na^+ ion insertion/desertion voltage, cost-effectiveness, and ease of synthesis. However, their instability and limited reversibility pose challenges for their practical implementation. PB, characterized by its open-framework structure, allows for high current charge/discharge rates. Nonetheless, it exhibits sensitivity to moisture, which can impact its performance and stability in SIBs.

2.4.1 Prussian Blue Analogue (PBA)

The Prussian Blue Analogues (PBA) has the formula $A_xMM'(CN)_6$ (A = K, Na, M and M′ = Co, Fe, Mn, Ni et.al). The 3D open-framework structure of PBA with a space group $Fm\bar{3}m$ is shown in Figure 2.4. In this structure, M and M′ are bridged by C≡N linkages and Na^+ ions occupy the active sites of M or M′. However，there are vacancies and interstitial water present within the crystal, resulting the exact formula of $A_xM_yM'[(CN)_6]_z\square_{1-z}$ where □ represents the vacancies rate. Theoretically, there are two Na^+ ions in PBA, leading to a specific capacity of 170 mAh/g. Co-precipitation is the low-cost method commonly used for synthesizing PBA. The open-framework structure provides the fast transport path of Na^+ ions, thus enhancing its performance. These favorable characteristics contribute to the potential commercialization of PBA. Prussian blue was historically employed as a blue pigment in the 1800s. In 2011, Goodenough et al. synthesized a series of PBAs and studied their electrochemical properties in SIBs (Y. Lu, Wang, Cheng, & Goodenough, 2012), marking a significant milestone. Since then, PBAs have been extensively studied as cathode materials for SIBs, achieving great success.

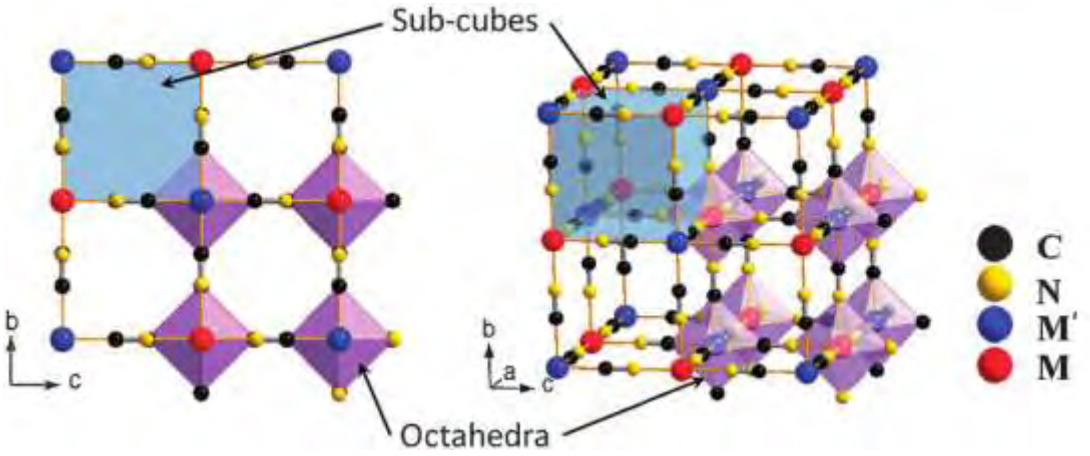

Figure 2.4: Framework of Prussian blue analogues. (Y. Lu et al., 2012)

2.4.1.1 $Na_xFeFe(CN)_6$

As previously mentioned, the theoretical specific capacity is 170 mAh/g. However, experimental results have shown that the actual specific capacity falls short of this value, and the cycling performance is unsatisfactory. To investigate the impact of defects, Yang et al. synthesized single crystal $FeFe(CN)_6$ without any defects and compared it with pristine PBA. The high crystallinity single crystal PBA delivered a specific capacity of 120 mAh/g, with nearly 100% Coulombic efficiency and 87% specific capacity retention after 500 cycles (Wu et al., 2013).

The researchers discovered that the inferior electrochemical performance was due to the presence of vacancies and interstitial water. Interstitial water likely occupied the active sites for Na^+ ions and reacted with the electrolyte during the charge/discharge process, leading to poorer electrochemical performance. In a subsequent study, Guo et al. successfully prepared high crystallinity $Na_{0.6}FeFe(CN)_6$ using a single Fe source, which delivered a specific capacity of 170 mAh/g (You, Wu, Yin, & Guo, 2014). The $Na_{0.6}FeFe(CN)_6$ material exhibited a vacancy rate of 6% and interstitial water content of 15.7. Chou et al. synthesized Na-rich $Na_{1.56}FeFe(CN)_6$ (W.-J. Li et al., 2015), where the higher Na content resulted in low vacancies and interstitial water. Employing this

strategy, Guo et al. (You, Yu, Yin, Nam, & Guo, 2015) synthesized $Na_{1.63}FeFe(CN)_6$ while Huang et al. (Yang Liu et al., 2015) synthesized $Na_{1.70}FeFe(CN)_6$, both showing improved electrochemical performance with increased Na content. The interstitial water can be removed through vacuum drying. In another study, Goodenough et al. obtained a rhombohedral $Na_{1.92}FeFe(CN)_6$, which exhibited a specific capacity of 160 mAh/g and retained 80% of its capacity after 800 cycles (L. Wang et al., 2015).

2.4.1.2 $Na_xMnFe(CN)_6$

The active site Fe in $Na_xFeFe(CN)_6$ can be substituted by other Na-active M^{2+}/M^{3+} ions and Mn has emerged as a promising candidate. Among transition metal, Mn^{2+}/Mn^{3+} offers the advantages of low cost and the ability to store Na^+ ions. Similar to $Na_xFeFe(CN)_6$, both Mn and Fe in $Na_2MnFe(CN)_6$ can provide active sites for Na^+ ions insertion. Cui et al. reported the synthesis of an open framework $Na_2MnMnFe(CN)_6$, which delivered a specific capacity of 209 mAh/g and 75% capacity retention after 100 cycles (H.-W. Lee et al., 2014). It is noted that the tri-electron reaction was responsible for the high specific capacity of $Na_2MnMnFe(CN)_6$. However, it should be noted that the Mn^+/Mn^{2+} redox couple operates at a low voltage range, resulting in a lower energy density for this part of the reaction. While the substitution of Mn increases the specific capacity of PBA, the lattice distortion caused by the Jahn-Teller effect and the dissolution of Mn presented challenges for the practical application of $Na_xFeFe(CN)_6$.

2.4.2 Transition Metal Oxides

Transition metal oxides in the form of Na_xTMO (M = Fe, Co, Ni, Mn, etc.), is a promising cathode material for SIBs since 1980s. In 1981, Delmas et al. reported that Na_xCoO_2 layered oxide can effectively store Na^+ ions within the voltage range of 2.0-3.5 V (Delmas, Braconnier, Fouassier, & Hagenmuller, 1981). Subsequently, in 1986, Tarascon et al. expanded the research to include other transition metals such as Ti, Fe, Cr,

Ni, and Mn, reporting the electrochemical characteristics of Na_xMoO_2 with five distinct plateaus (Tarascon & Hull, 1986). However, the arrival of commercial LIBs led to a decline in the study of SIBs, including investigations into cathodes, anodes, and electrolytes. This trend persisted until around 2010 when the rising demand for LIBs and the challenges faced by LIB technology revitalized interest in SIBs as a potential candidate for energy storage systems (Delmas, 2018),

2.4.2.1 P2-Type Transition Metal Oxides

P2-type TMOs are commonly reported as P-type materials. These layered oxides are characterized by a stacking arrangement of $[TMO_6]$ and $[NaO_6]$ units in an orderly manner. In the crystal structure, Na^+ ions occupy either the *2d* or *2b* sites but are typically not fully occupied, ranging from 0.6 to 1, to maintain structural stability. Its XRD pattern exhibits characteristic peaks at approximately 15.8° (002) and 38.9° (102) with a space group of $P6_3/mmc$ (T. Zhang et al., 2022).

A pioneering study of a typical P2-type TMO Na_xCoO_2 was conducted by Hagenmuller in 1973. He reported P2-type -$Na_{0.70}CoO_{1.96}$, which delivered a specific capacity of about 90 mAh/g (Fouassier, Matejka, Reau, & Hagenmuller, 1973). In a study by Goodenough et al. in 2005, the researchers studied the structural transition and Na^+ ions diffusion coefficient of $Na_{0.8}CoO_2$ during the charge/discharge process (W. Y. Zhang et al., 2005). In 2011, Delmas et al. studied the structural transition of Na_xCoO_2 and found that the presence of multiple plateaus in the charge/discharge curves was attributed to the ordering of Na/vacancies (Berthelot, Carlier, & Delmas, 2011).

In 2011, Carlier et al. synthesized P2-type -$Na_{2/3}Mn_{1/3}Co_{2/3}O_2$ which delivered a specific capacity of 112 mAh/g within the voltage range of 1.5-4.0 V. During the charge process, Co^{3+} ions change to Co^{4+} while the valence of Mn^{4+} ions remained unchanged. On the other hand, during discharge, Co^{4+} ions converted back to Co^{3+} and below a voltage of 2.5 V, Mn^{4+} ions changed to Mn^{3+} followed by the conversion of Co^{3+} to Co^{2+}

(Carlier et al., 2011). Another promising material, P2-type-$Na_{2/3}Fe_{1/2}Mn_{1/2}O_2$ demonstrated a specific capacity of 190 mAh/g in the voltage range between 1.5-4.3 V and exhibited satisfactory rate and cycling performances (M. H. Han et al., 2015). However, this material faced challenges regarding the migration of Fe ions during the charge/discharge process. To overcome this issue, substitution with Ni or Cu was explored, effectively restraining the migration of Fe ions. Another concern is the voltage decay, with the underlying mechanism yet to be fully understood. Another drawback was the low initial Na content of P2-type -$Na_{2/3}Fe_{1/2}Mn_{1/2}O_2$, requiring additional Na resources to achieve the theoretical specific capacity in full-cell applications. In addition, the poor air-stability of P2-type-$Na_{2/3}Fe_{1/2}Mn_{1/2}O_2$ limited its practical applications. Lastly, the strong Jahn-Teller effect leaded in huge structural changes during charge/discharge process.

Another important layered TMO is $Na_{2/3}Mn_{1/3}Ni_{2/3}O_2$, which has found application as a precursor for cathode materials in LIBs. In 2001, Dahn reported on the use of this material as a cathode material for SIBs, demonstrating a specific capacity of about 150 mAh/g in the voltage range between 2.0-4.5 V (Z. Lu & Dahn, 2001). Similar to P2-type -$Na_{2/3}Mn_{1/3}Co_{2/3}O_2$, the charge/discharge curve of $Na_{2/3}Mn_{1/3}Ni_{2/3}O_2$ exhibited multiple plateaus. However, the high-voltage phase transition induced significant volume changes, resulting in rapid capacity fading. It is noted that a recent study reported that this material delivered additional specific capacity due to the O^{2-} redox reactions occurring above 4.2 V when some element was substituted (Rong et al., 2018) The substitution of Ti in the Mn sites has been shown to efficiently improve the cycling performance of $Na_{2/3}Mn_{1/3}Ni_{2/3}O_2$ (Tapia-Ruiz et al., 2018). This substitution reduced the volume change and the multi-plateaus. However, it leads to a decrease in specific capacity due to the incorporation of non-electrochemically active elements.

2.4.2.2 O3-type Layer oxides

By adjusting the element ratios and synthesis conditions, different structural types of target materials can be obtained. The transition metals (TMs) commonly selected for O3-type structures were Sc, Ti, V, Cr, Mn, Fe, Co, Ni, and Cu. Among them, there is no sodium ion activity of $NaScO_2$. O3-$NaTiO_2$, with a redox potential of approximately 1.0 V, is more suitable as an anode material for SIBs (D. Wu et al., 2015). Similarly, O3-$NaVO_2$ could deliver a specific capacity of around 126 mAh/g but possessed a low redox potential, rendering it unsuitable as a cathode candidate (Didier et al., 2011). O3-$NaCrO_2$, reported by Braconnier et al. in 1982, demonstrated a specific capacity of approximately 110 mAh/g in the voltage range of 2.5-3.6 V (J. Braconnier, Delmas, & Hagenmuller, 1982). O3-$NaMnO_2$, exhibited a specific capacity of 185 mAh/g, corresponding to the 0.8 Na^+ ions insertion/desertion, as reported by Ceder et al. in 2011 (X. Ma, Chen, & Ceder, 2011). However, the phase transition behavior is complex and the stability is low. O3-$NaFeO_2$, another promising cathode candidate for SIBs, was first reported by Takeda et al. in 1994 and delivered a specific capacity of 120 mAh/g, corresponding to the insertion/desertion of 0.2 mol Na^+ ions (Takeda et al., 1994). It is worth noting that Fe-based cathode materials exhibited the highest redox potential. O3-$NaCoO_2$ was first reported by Delmas in 1980 and it delivered a specific capacity of 140 mAh/g at the voltage range between 2.5 and 4.0 V (J.-J. Braconnier, Delmas, Fouassier, & Hagenmuller, 1980). However, the multiple charge/discharge plateaus limited its practical applications. Similarly, multiple charge/discharge plateaus have also been observed in O3-$NaNiO_2$ (J. Braconnier et al., 1982).

The utilization of dual-TM O3-type layered oxides is an effective strategy to enhance the complex phase transition behavior. An example of this is $NaNi_{0.6}Co_{0.4}O_2$ which exhibited a specific capacity of about 95 mAh/g, showing two charge/discharge plateaus of 2.25 V and 2.4 V, corresponding to two-phase transitions.= (Saadoune, Maazaz,

Menetrier, & Delmas, 1996). Nanba et al. discovered that the chemical valence of Fe and Ni in $NaFe_{0.5}Ni_{0.5}O_2$ is +3, while that of Ni in $NaNi_{0.5}Ti_{0.5}O_2$ is +2 and that of Ti is +4, resulting a lower working potential of $NaFe_{0.5}Ni_{0.5}O_2$ (Nanba et al., 2016).

$NaFe_{0.5}Co_{0.5}O_2$ showed a higher specific capacity of 160 mAh/g in 2.5-4.0 V corresponding to the insertion/desertion of 0.7 mol Na^+ ions, along with excellent cycling stability (Hiroaki Yoshida, Yabuuchi, & Komaba, 2013). In-situ XRD analysis revealed a phase transition of O3-P3-P'3-O3 during the charge/discharge process without the presence of O'3 phase. This absence of a tetrahedral configuration in the Na layer (the absence of O'3 phase) has contributed to the improved structural stability (Kubota et al., 2016). This is due to the migration path of TM occurring through the TM layer octahedra and Na layer tetrahedra. As a result, the overall structural stability was further enhanced. Ceder et al. synthesized $Na[Fe_{1/3}Co_{1/3}Ni_{1/3}]O_2$ and $Na[Fe_{1/4}Co_{1/4}Ni_{1/4}Mn_{1/4}]O_2$ with the specific capacity of 165 mAh/g and 180 mAh/g, respectively (X. Li et al., 2014). The Jahn-Teller effect of Fe ions acted positively by restraining Na desertion at high voltages. However, it also contributed to poorer Fe migration. Ceder also pointed out that Fe migration only occurred when the Fe content was below 0.3.

Mn-based O3 materials have garnered attention as promising layered oxides because of the low price of Mn. O3-$NaFe_{0.5}Mn_{0.5}O_2$ was first reported by Komaba et al. with a specific capacity of about 170 mAh/g at 1.5-4.0 V (Yabuuchi et al., 2012). Building upon this material, Hu et al. synthesized Cu-substituted O3-$Na_{0.9}Cu_{0.22}Fe_{0.3}Mn_{0.48}O_2$ with a specific capacity of 100 mAh/g (2.5-4.05 V) and Fu et al. synthesized Cr-substituted O3-$Na_{0.9}Cr_{1/3}Fe_{1/3}Mn_{1/3}$ with specific capacities of 165 mAh/g (1.5-4.1 V) and 186 mAh/g (1.5-4.2 V), respectively (M.-H. Cao et al., 2017; Mu et al., 2015). It is noted that $Na_{0.9}Cu_{0.22}Fe_{0.3}Mn_{0.48}$ is air and moisture stable. O3-$NaNi_{0.5}Mn_{0.5}$ was first report by Komaba et al. with specific capacities of 125 mAh/g (2.2-3.8 V) and 200 mAh/g (2.2-4.5 V) (Komaba et al., 2009).

2.4.3 Other cathode materials for SIBs

Polyanion compounds are a type of cathode material for SIBs. They offer several advantages over TMO and PBA. One advantage is their thermal stability, attributed to the presence of P-O bonds. Additionally, polyanion compounds exhibit a fast diffusion path for Na^+ ions due to their three-dimensional structure. However, they do suffer from low electron conductivity.

A widely studied polyanion compound is $Na_3V_2(PO_4)_3$, with a space group of $R\bar{3}c$. It is built from VO_6 octahedra corner- sharing with three PO_4 tetrahedra. $Na_3V_2(PO_4)_3$ has a high theoretical specific capacity of 235 mAh/g (Jian et al., 2013). However, its application is hindered by the presence of toxic vanadium (V) element. Another widely studied V-based polyanion compound is $NaVPO_4F$, which has a theoretical specific capacity of 143 mAh/g (Law & Balaya, 2018). Nevertheless, it suffers from low electron conductivity and toxicity issues. Other V-based polyanion compounds, including $Na_3V_2(PO_4)_2F_3$, $Na_3(VOPO_4)_2F$, $Na_3V(PO_3)_3N$ have also been studied (M. Bianchini et al., 2014; Z. Liu et al., 2014; Y. Qi et al., 2018; S. Wang et al., 2021). These materials hold promise for SIBs but have their own specific challenges to overcome.

$NaFePO_4$ is another promising cathode material for SIBs and exists in two structures: maricite and triphylite shown in Figure 2.5 (Moreau, Guyomard, Gaubicher, & Boucher, 2010). The triphylite form of $NaFePO_4$ can transform into maricite $NaFePO_4$ at high temperatures. However, maricite $NaFePO_4$ is inactive for Na^+ ion migration due to the absence of suitable pathways. Direct synthesis of triphylite $NaFePO_4$ is not feasible and is typically achieved through ion exchange methods (Whiteside, Fisher, Parker, & Islam, 2014). Triphylite $NaFePO_4$ showed a specific capacity of about 120 mAh/g with an operating voltage of about 2.8 V. Its long cycling performance is attributed to the stable olivine structure of $NaFePO_4$ (Oh, Myung, Hassoun, Scrosati, & Sun, 2012). More recently, Niu et al. reported the synthesis of graphene optimized $Na_{6.24}Fe_{4.88}(P_2O_7)_4$

composite nanofibers using the electrospinning method. This composite material showed a specific capacity of approximately 100 mAh/g after 320 cycles. However, further improvements are needed to enhance its efficiency (Niu, Xu, Shen, Dai, & Li, 2016).

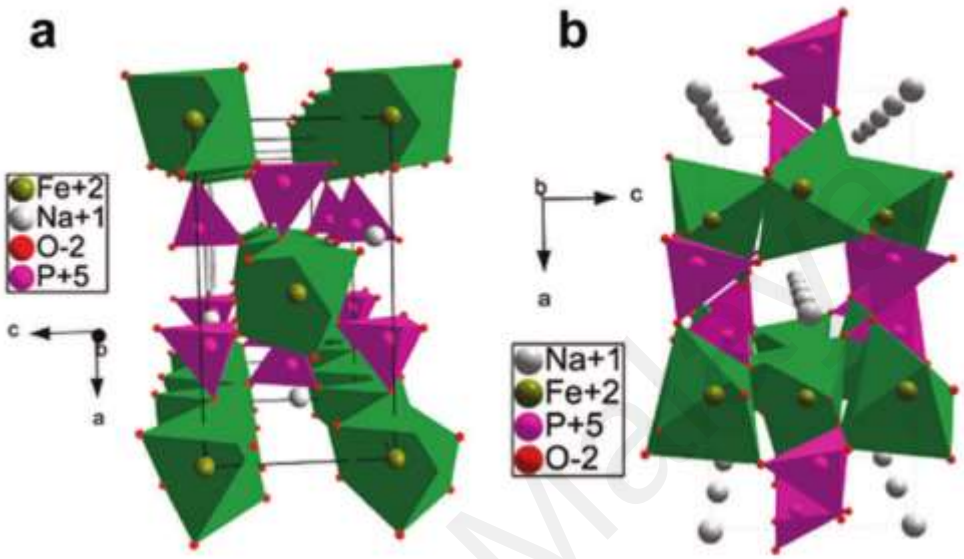

Figure 2.5: The crystal structure of (a) maricite $NaFePO_4$ and (b) triphylite $NaFePO_4$ (Moreau et al., 2010).

In addition to the cathode materials mentioned above, other types of materials have also been explored for their potential application in sodium-ion batteries. These include sulfates, fluorosulfates, carbonophosphates, and organic compounds (Y. Gao et al., 2021; Hassanzadeh & Sadrnezhaad, 2021; M. Lee et al., 2017; Ni, Bai, Wu, & Wu, 2017; Q. Wang, Madsen, Owen, & Weller, 2013).

2.5 Advanced Characterization Techniques

2.5.1 In-Situ X-Ray/Neutron Tomography

In-situ X-ray powder diffraction (XRD) is a powerful technique that can record the diffraction patterns of materials during electrochemical reactions. The X-ray scans the battery electrode cycle by cycle, and the resulting diffraction patterns provide valuable insights into the evolving crystal structure. The diagram of the cell is shown in Figure

2.6a. The coin cell can be holed, with a polymer material serving as the observation window (J. Wang et al., 2016; Li Zhang et al., 2020). This transparent window allows X-rays to pass through and interact with the battery electrode, enabling the collection of diffraction data without disturbing the electrochemical processes occurring inside the cell.. By analyzing the changes in diffraction patterns throughout the cycling of the battery, researchers can identify and characterize the various phases and structural transformations that take place during charge and discharge. This information is crucial for understanding the electrode degradation and capacity fading upon cycling (M. H. Han, Gonzalo, Casas-Cabanas, & Rojo, 2014; Wei, Wang, An, Han, & Mai, 2017; Yabuuchi et al., 2012), and can guide the development of improved energy storage systems. The X-ray scanning time for one cycle can be short, depending on the resolution of X-ray resources. However, it can be challenging to unravel the redox reactions within complex electrode material systems. This is primarily because the formation of interphases is closely associated with the changes in alkali ion content within the host material.

Metastable interphases that form during cycling are thermally unstable and can be challenging to detect once the electrochemical process is stopped (Matteo Bianchini, Wang, Clément, & Ceder, 2018; S. Guo et al., 2016; C. Zhao, Wang, et al., 2020). The phase reactions involving these interphases occur rapidly upon removal of the external voltage, making them difficult to observe and characterize. These phenomena highlight the need for in-situ techniques such as in-situ X-ray diffraction to capture the dynamic nature of the electrochemical processes and the associated interphase formation. Recently, an *in-situ* XRD (Z. Li et al., 2022) was carried out to investigate the phase evolution of the Bi anode in SIBs as depicted in Figure 2.6 (b). The reaction mechanism of electrode during the sodiation/desodiation process was studied. Notably, characteristic peaks corresponding to the interphase of NaBi and $NaBi_3$ were observed during charge

and discharge cycles. These results reveal the alloying/dealloying reaction mechanism of metal Bi involves highly reversible conversion reaction.

The layer oxide is one of the most promising positive materials for SIBs. However, their structural evolution during sodiation and desodiation processes is complex. Adelhelm et al. (Liangtao Yang et al., 2021) recently introduced Li ions as additives in P2-type layered oxides and employed in-situ XRD to investigate the phase evolution during Na^+ extraction and reinsertion. The extracted a and c lattice parameters from the XRD data exhibited changes, but the parameter deviation before Na^+ ion extraction and complete reinsertion was much smaller compared to the reported phase evolution. These findings suggest that Li-substituted sodium layered oxides follow a conversion-based sodium storage mechanism. These reported results highlight the power of in-situ XRD as a valuable technique for studying the structural evolution of electrode materials during the extraction and insertion of alkali ions in electrochemical cycling. It provides crucial structural information that contributes to a deeper understanding of the ion storage mechanisms within the electrode material.

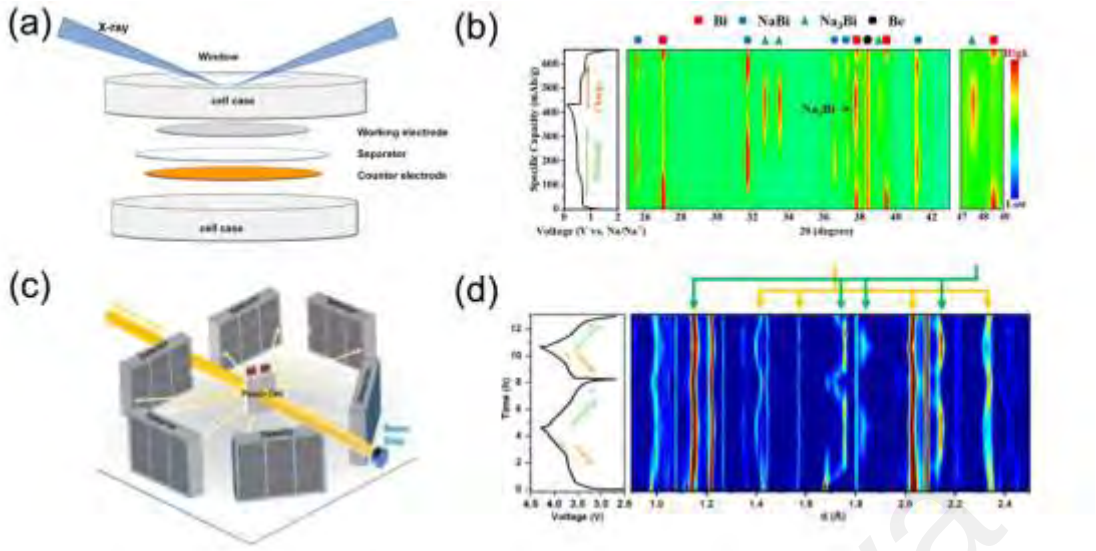

Figure 2.6: (a) Schematic of the in-situ XRD cell, (b) The galvanostatic charge/discharge curves of Na//Bi half battery during the in situ XRD test and corresponding 2D color-filled contour plot (Z. Li et al., 2022), (c) Schematic of in operando neutron diffraction study and (d) a typical first two cycles charge/discharge curve of cell and corresponding surface contour plots of cathode and anode neutron diffraction (C. Wang et al., 2022).

Understanding the redox reactions of both cations and anions in rechargeable batteries is crucial for comprehending the capacity origin of electrode materials (Rong et al., 2018; Rozier et al., 2015; C. Zhao et al., 2017). Therefore, the oxidation states of the cations and anions should be elucidated during electrochemical charging and discharging, particularly in complex systems with multiple types of ions (Dai et al., 2019; Kobayashi et al., 2019; Risthaus et al., 2018; Rong et al., 2019).

The substitution of metallic ions into transition metal sites is now a leading strategy to improve the electrochemical performance of layered oxides (Xia et al., 2021; J. Xu et al., 2014; W. Zhao et al., 2014). Jie and coworkers investigated the cations redox behavior of a Mn/Fe/Ni ternary sodium layered oxide. Their work confirmed the redox reactions of $Fe^{3+<->4+}$, $Ni^{2+<->3+<->4+}$, while the Mn ions remained inactive during the electrochemical processes (Risthaus et al., 2018; D. Zhou et al., 2020). High-entropy oxides, which consist

of more than 5 ions occupying transition metal sites, have demonstrated enhanced ion storage properties compared to oxides with fewer than 3 metal ions (C. Zhao, Ding, Lu, Chen, & Hu, 2020). Recently, Lin et al. investigated the cation redox reactions in a high-entropy sodium layered oxide using *in-situ* X-ray absorption spectroscopy (XAS). Their findings revealed the electrochemically active redox behavior of Cu^{2+} <—> Cu^{3+} during de/sodiation, while Ti^{4+} remained unchanged (Lin et al., 2022). It is still challenging to probe the atomic- and molecular-scale structure information of electrode materials for the rechargeable batteries. This is because the conventional XRD is only sensitive to the particle-level structure change during the electrochemical charge and discharge(Hou et al., 2021; Senthilkumar, Johnson, & Senguttuvan, 2022). However, the atomic- and molecular-level structure information is critical to understand the electrochemical properties of the rechargeable batteries. In-situ neutron powder diffraction (NPD) is a technique that is sensitive to alkali ion migration during electrochemical processes (Avdeev et al., 2013; J. Liu et al., 2020; Q. Shen, Liu, Jiao, Qu, & Chen, 2021). Furthermore, it is also able to probe the bulk structure information due to its high penetration depth (Brant et al., 2014). The typical schematic and plot of *in-situ* NPD study is shown in Figure 2.6c and d. The *in-situ* NPD was conducted to study the bulk reaction of the carbonation of Na_2ZrO_3 (Pavan & Ling, 2022). The diffractions show the carbonation and regeneration of the carbonated Na_2ZrO_3. This *in situ* NPD also enabled the probing of alkali ion diffusion behavior during electrochemical processes (C. Wang et al., 2022). The result unveiled that the mixing between alkali and transition metal ions varies and alkali ions hopping between tetrahedral sites during the electrochemically charging process.

2.5.2 In-Situ Microscopy

Scanning/transmission Electron Microscopies (SEM/TEM) are useful and powerful tools to probe the morphology and local structure of the electrode materials(M. Liu & Li, 2022). They have been extensively and intensively used to probe the morphology and local structure information of the as-synthesized materials. Many studies suggested that the decay of ion storage property is related to the morphology change of the electrode materials, such as particle cracking (C. Chen et al., 2022; G.-L. Xu et al., 2022). Additionally, the volume expansion and contraction of the electrode has also been reported as the cause of the capacity fading upon alkali ion extraction and insertion (Tan et al., 2022; H. Wang, Liu, Yu, & Wu, 2022). It is highly desired to directly observe the morphology change during the electrochemical process. The hard carbon is considered as the most promising negative material for commercial sodium-ion batteries. The volume expansion and the microstructural change upon de/sodiation have been probed using *in-situ* TEM (Figure 2.7a-d). The *in-situ* observation clarified the Na^+ ion storage mechanism that the Na^+ ion inserted into the surface porous and then into the graphene interlayers (K. Wang et al., 2019). The thermal stability of the layered oxides is important for its practical application. The *in-situ* STEM combining the SAED was conducted to probe the structure information during the thermal process of the P2-type -Ni/Mn-based material (Figure 2.7e). The result shows that this P2 is thermally stable below 300 °C. When the temperature was further increased, new and weak diffraction spots were observed, indicating generation of the nano-grains on the particle surface (Hou et al., 2022).

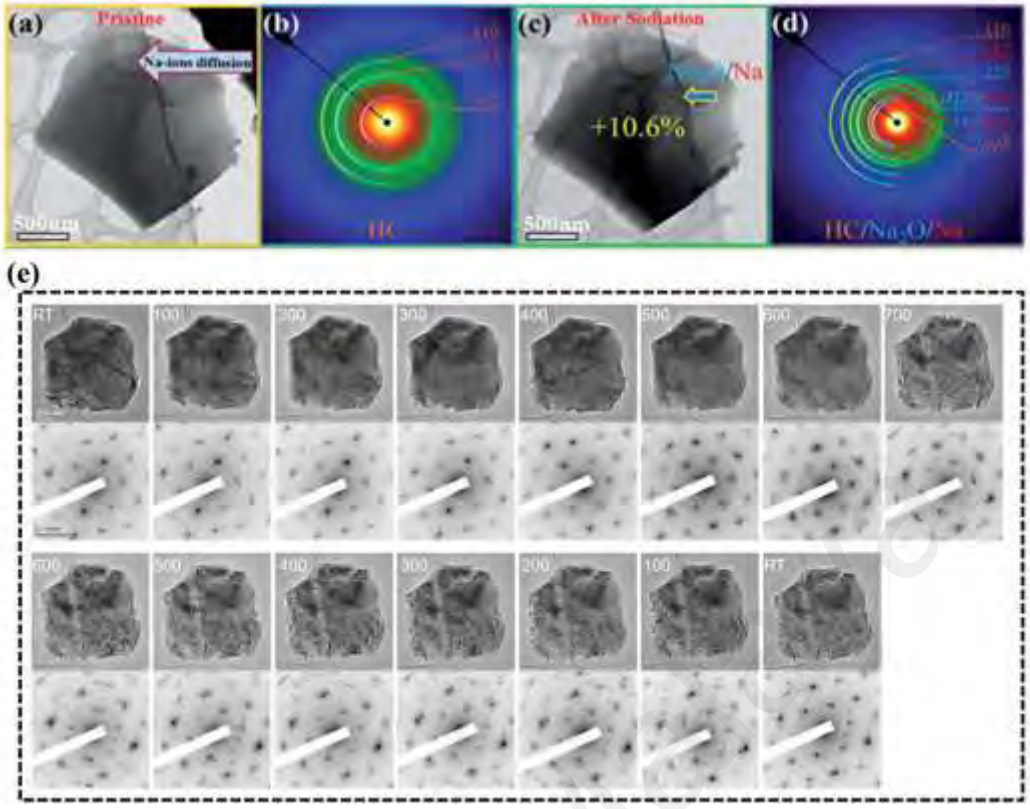

Figure 2.7: (a) Sodiation of hard carbon studied by in situ TEM. The (a) TEM image and (b) electron diffraction pattern of the pristine hard carbon. The (c) TEM image and (d) electron diffraction pattern of the sodiated hard carbon. (K. Wang et al., 2019) Real-time bright-field images and SAED patterns of the polycrystalline PNNMO particle at different temperatures (Hou et al., 2022).

The X-ray Computed Tomography (CT) is a non-destructive technique (Figure 2.8a) known for its exceptional spatial and temporal resolutions. Due to these advances, it is very suitable for the visualization and quantification of electrochemical and mechanical degradation of rechargeable batteries (Wood, 2018). It has been frequently used in sodium-oxygen battery, where the Na^+ ions diffuse through the electrolyte and react with the oxygen, forming sodium superoxide, resulting in precipitation within the cathode structure (Hartmann et al., 2013). The CT tomography shows that the discharge NaO_2 product penetrate deeply into the layers of the cathode, providing crucial insights. It has also been widely used to investigate electrode degradation in rechargeable batteries.

The Atomic Force Microscopy (AFM) contains a sharp tip (probe) that is used to scan the specimen surface (Maeda, Kitta, & Kuratani, 2022). By combining forces and Hooke's law, it can be used to image and characterize atoms and structures on various surfaces. It is suitable to study the electrode-electrolyte interfacial reactions (Shadike et al., 2018). In a study focused MoS_2 electrode surface, *in-situ* AFM was conducted to observe the electrode-electrolyte interface generation (Figure 2.8 b-e) (Lacey et al., 2015). When the voltage reached 0.4 V, the permanent wrinkling behavior was observed. Furthermore, force tomography revealed the formation of a solid-electrolyte interphase at 1.5 V.

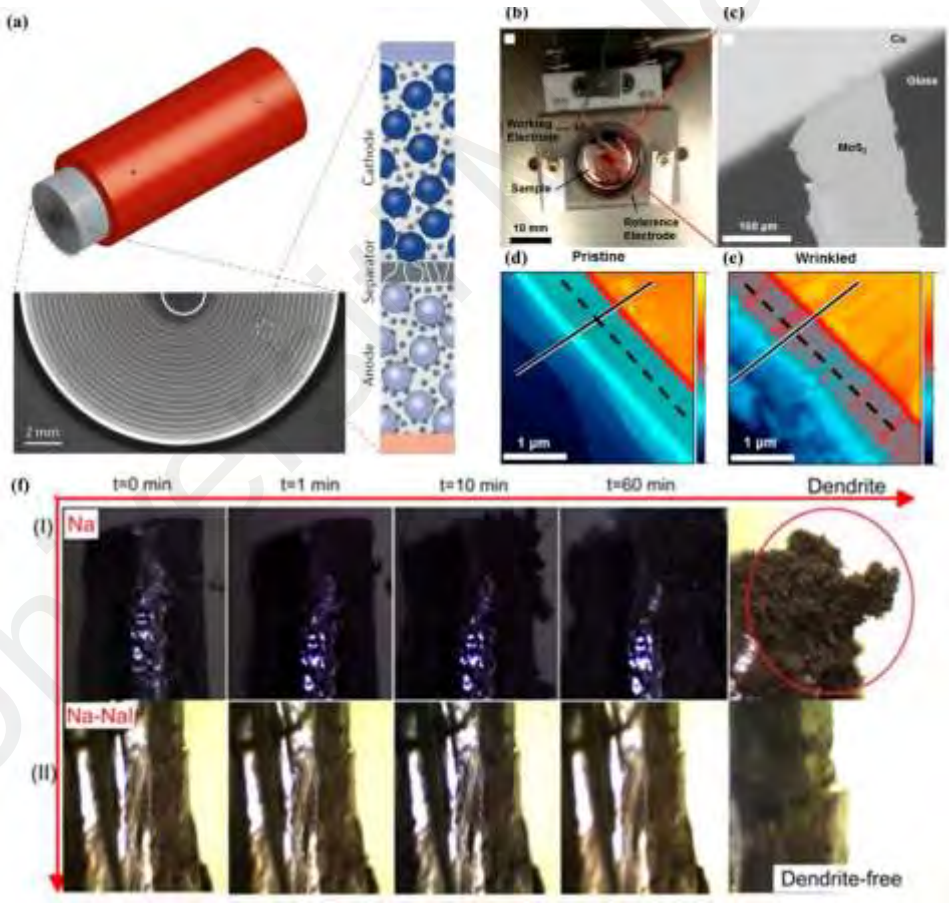

Figure 2.8: (a) Schematic and X-ray tomographic cross section of an example battery cell (Wood, 2018), (b) a digital image of the planar microscale battery within a liquid electrochemical cell which is used to conduct in situ CT, (c) an image of MoS_2 flakes partially coated by Cu, (d) (e) in situ AFM images (Lacey et al., 2015) and (f) In situ optical microscopy observations of sodium electrodeposition process in Na/Na and Na-NaI/Na-NaI symmetrical cells in carbonate electrolyte at a constant current of 1.0 mA cm^{-2}. (Tian et al., 2019)

Optical Microscopy is based on the reflection and refraction of transmitting light on an object (J. Gao et al., 2022; Yousaf et al., 2022). It offers several advantages such as nonvacuum manipulation, ease of access, and nondestructive nature (Zhu, Liu, Feng, & Guo, 2018). It enables direct visual observation from mesoscale to microscale (B. Chen, Zhang, Xuan, Offer, & Wang, 2020). In the realm of electrochemical storage systems, the interphase layer between electrode material and electrolyte holds significant interest. However, traditional characterization techniques often fail to provide direct observations of this interface. Recently, The Na-NaI electrode and electrode interface growth has been observed by *in-situ* Optical Microscopy (Tian et al., 2019). The presence of NaI significantly suppressed the growth of dendrites after 10 mins of sodium electroplating. As an observed by the *in-situ* Optical Microscopy, the surface of the Na-NaI is much smoother. Additionally, the diffusion of the Mn from the electrode Mn-materials to the electrolyte during cycling caused the capacity fading and poor capacity retention. By using *in-situ* Optical Microscopy, the temporal and spatial distribution of Mn^{2+} from the electrode material to the electrode in the $LiMn_2O_4$ electrode material could be visualized. It should be noted that the Optical Microscopy is a useful tool and can also be used for more applications. This report merely highlights the two *in-situ* applications as examples.

2.5.3 In-Situ Spectroscopy

Raman Spectroscopy is another valuable tool in material science to probe the vibrational modes of the molecules (Heber, Hofmann, & Hess, 2022; Kuwata et al., 2022). The local structural change usually influences the change of the vibrational modes. It is therefore recently used to study of the ion storage mechanism. Sun et al. studied the Na^+ ion storage mechanism in carbon nanosheets during the electrochemical charging and discharging using the *in-situ* Raman spectroscopy (Figure 2.9a). The D and G band were detected during the charge and discharge process, while the peak intensity ratio (I_D/I_G) changed. Notably, the ID/IG ratio increased to 0.99 when charged to 3.0 V and returned

to its original value upon discharge, indicating that the Na^+ ion diffusion is reversible (Sun et al., 2022). In a separate study, in-situ Raman Spectroscopy was employed to explore the oxygen redox activity of P2-type sodium layered oxide (X. Cao et al., 2020). When the voltage was above 4.0 V, a new chemical shift peak appeared at around 825 cm^{-1}. And this peak disappeared during discharge. This peak was assigned to the peroxo-like species. Another chemical shift at 1140 cm^{-1} appeared during the first charge and persisted in subsequent processes. This was assigned to the generation of superoxol species. These findings suggested the occurrence of the anionic redox reactions during electrochemical charge and discharge.

The Fourier-transform infrared spectroscopy (FTIR) is a technique used to obtain the infrared spectrum of absorption or emission of a material (Roberts et al., 2022), providing insights into the functional groups present. The FTIR can be applied to identify the presence of organic and inorganic compounds qualitatively and quantitatively in the sample (Shraer et al., 2022). The *in-situ* FTIR was performed to study the nucleation and growth upon synthesis (Figure 2.9b and c) (Y. Xu et al., 2019). This technique has also been applied to study the Na^+ ion storage mechanism in carbon materials (Huangfu et al., 2021). The reversible interactions between functional groups, such as C=O and N-related groups, with Na^+ ions were probed, indicating a synergistic Na^+ ion storage mechanism.

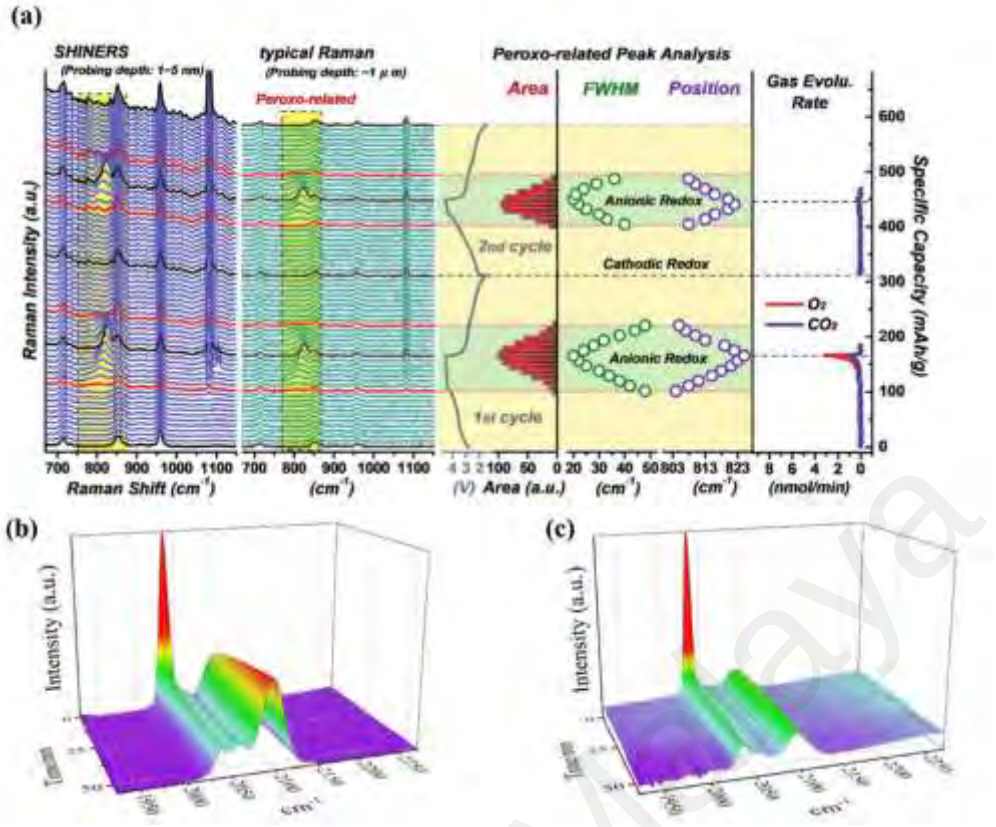

Figure 2.9: (a) In situ SHINERS and in situ bulk Raman spectra during first and second cycles, as well as the corresponding in situ DEMS results of gas evolution rate. In situ infrared spectroscopy during the synthesis process (X. Cao et al., 2020), (b) in situ infrared spectroscopy during the synthesis process and (c) without complexing agent control.

Differential Electrochemical Mass Spectrometry (DEMS) is a technique used to detect gaseous species released during the electrochemical process (Dang et al., 2022; Darbar et al., 2022; J. Li et al., 2022). While the oxygen redox reaction has been observed using the SXAS technique, a more advanced technique is required to observe gas evolution during ion insertion and extraction. On the other hand, electrolyte decomposition occurs during electrochemical processes, leading to the generation of gases and increasing the risk of fires (Dreyer, Kondrakov, Janek, & Brezesinski, 2022). In-situ DEMS technique enables the quantitative analysis of gas release during electrochemical charging and discharging. A recent study by Qi et al. utilized DEMS to investigate Li-substituted Mn/Fe-based positive materials (X. Qi et al., 2022). The detection of O_2 and CO_2 during desodiation

provided insight into the capacity fading observed during cycling, attributed to the detrimental effects of these gases on the lattice structure. In another study, the gas evolution of sodium layered oxide ($NaNi_{0.45}Zn_{0.05}Mn_{0.4}Ti_{0.1}O_2$) with a hard carbon anode was investigated using in-situ DEMS (Figure 2.11) (Leiting Zhang, Tsolakidou, Mariyappan, Tarascon, & Trabesinger, 2021). The detection of C_2H_4, H_2, and CO_2 during electrochemical charge and discharge provided further insights into the capacity fading mechanisms in sodium-ion batteries. These findings offer valuable insights into understanding the capacity fading phenomena in sodium-ion batteries.

.

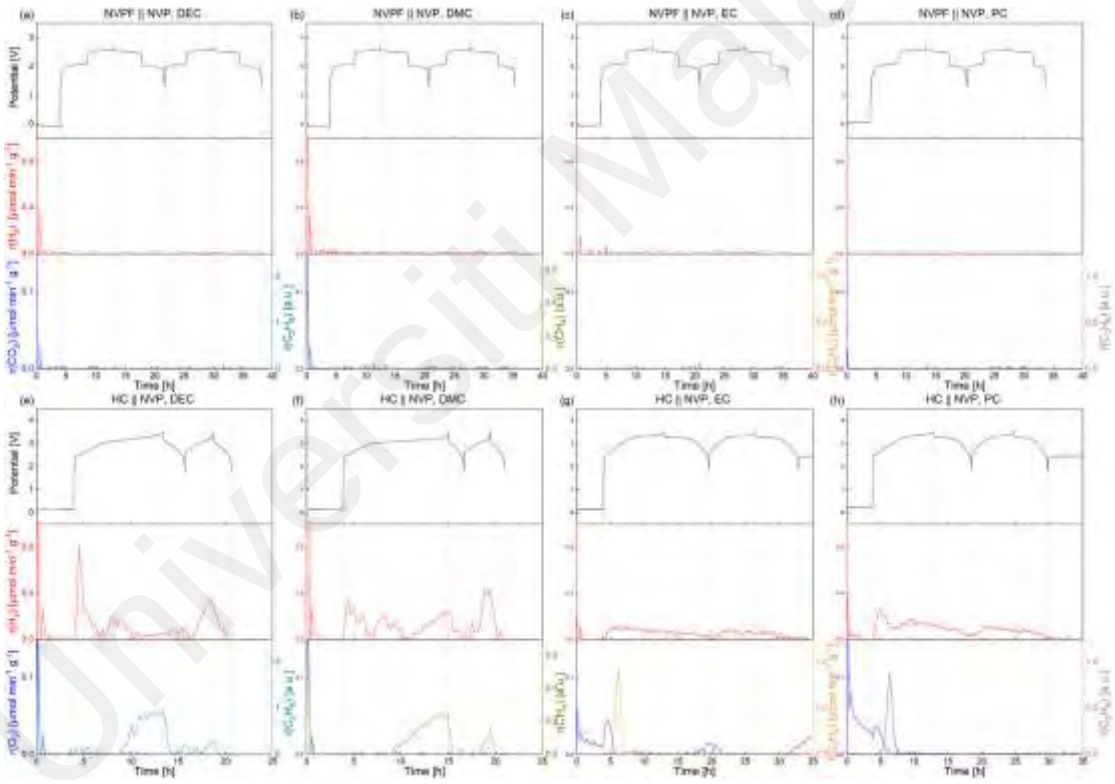

Figure 2.10: Gas evolution upon oxidation (a-d) and reduction (e-h) of single-solvent electrolytes studied on NVPF || NVP and HC || NVP model systems, respectively. The solvent used is specified on top of individual figure panels. All gas rates are normalized to the cathode mass. Note that the left y-axis label only appears in the far-left figure and the right y-axis label in the far-right figure, if they are the same. All individual gas rates are presented at the same scale. (L. Zhang et al., 2021)

The Nuclear Magnetic Resonance spectroscopy (NMR) is technique that uses the magnetic properties of atoms (Billaud et al., 2014; Grey & Dupré, 2004). It is widely employed in organic and inorganic chemistry, serve as a tool to characterize chemical composition, structure, kinetics, and thermodynamics. It has been used to probe the local environment of the key elements, so as to reveal the electrochemical reactions and ion storage mechanisms in rechargeable batteries (Pecher, Carretero-González, Griffith, & Grey, 2017). To the best of our knowledge, there is no *in-situ* NMR study on the sodium cathode due to the difficulties associated with configuring *in-situ* sodium-ion battery setup (Gonzalo, Zarrabeitia, Drewett, López del Amo, & Rojo, 2021). Most studies have relied on ex-situ NMR investigations. Nevertheless, the in-situ NMR technique has been successfully applied to explore electrode materials in other rechargeable battery systems, such as sodium metal batteries and lithium-ion batteries (L. Gao, Chen, Chen, & Kong, 2022; Šić et al., 2022).

2.6 Summary

- The increasing demand for LIBs has led to the development of the next generation of rechargeable battery system.
- SIB is one of the promising candidates for the next generation of rechargeable batteries.
- Anode materials for SIBs encompass carbon-based materials, Ti-based materials, organic materials, alloy materials and more.
- Cathode materials for SIBs include transition metal oxides, Prussian blue analogues, polyanion compounds, organic compounds, polymers and others.
- The introduction of in-situ X-Ray/neutron tomography, in-situ microscopy and in-situ spectroscopy has significantly advanced battery research.

CHAPTER 3: EXPERMENTAL METHODS

3.1 Introduction

There are three sections in these chapter, including the synthesis method of PBA and P2-type TMO, characterizations of as-prepared PBA and P2-type TMO as cathode material and electrochemical testing of SIBs using the as-prepared PBA and P2-type TMO as cathode material.

3.2 Synthesis Methods

3.2.1 Synthesis of Prussian Blue Analogues

Using a conventional method, $FeCl_3$ and $K_4[Fe(CN)_6]$ are employed as the starting materials to synthesize PB as a pigment. In an acidic solution, the mixture solution undergoes a conversion process, resulting in the precipitation of blue PB. However, the electrochemical performance of PB synthesized through this method is considerably low due to the high interstitial water and vacancies rates. To ensure PB's suitability as cathode material for SIBs, it is crucial to minimize the interstitial water content and vacancies. Consequently, we have made modifications to the synthesis process to decrease both the interstitial water and vacancies rates by hydrothermal method

In Chapter 4, the synthesis of Na-rich PBA using a single iron source and an excess of Na source is described. The specific process is presented in Figure 3.1. Initially, NaCl was added to a 100 ml solution of 0.1 M HCl, resulting in mixtures with varying NaCl concentrations (0M, 1M, 2M, 4M). Subsequently, 484 mg of $Na_4Fe(CN)_6 \cdot 10H_2O$ was added to each solution under magnetic stirring at room temperature. After stirring for 30 minutes, clear yellow solutions were obtained. The beakers containing the solutions were then heated at 80 °C and placed in an oven for 12 hours. The resulting precipitation was collected through centrifugation and washed with ethanol and distilled water. The washed precipitation was subsequently transferred to a vacuum oven and maintained at 100 °C

for 24 hours to obtain the PBA. The PBA samples synthesized with different NaCl concentrations (0M, 1M, 2M, 4M) were labeled as PB-0M, PB-1M, PB-2M, and PB-4M, respectively.

In Chapter 5, a surface modification method is employed to synthesize PBA, specifically PB-A. The synthesis procedure for PB-A follows a typical method outlined in Figure 3.2. Initially, 4 mmol of $Na_4Fe(CN)_6 \cdot 10H_2O$ and 5 g of PVP (K30) are added to 500 mL of 0.1 M HCl solution under stirring at a temperature of 65 °C for 4 hours. The resulting light-yellow solution is then transferred to an oven and heated at 80 °C for an additional 20 hours. After aging the dark blue precipitate for 48 hours, the supernatant is removed, and the precipitate is washed several times with ethanol and distilled water. The product is collected through high-speed centrifugation and vacuum dried at 80 °C for 24 hours.

For the etching process, 100 mg of the as-synthesized product and 200 mg of PVP are added to a Teflon vessel containing 40 ml of 1 M HCl solution. After half an hour, the vessel is transferred to an autoclave and heated at 150 °C for 12 hours. The resulting material is collected using the same method as before and labeled as PB-A.

In the preparation of PB-C, all the steps are repeated, with the exception of the first heating process after the formation of the light-yellow solution. Instead, the heating in an electric oven at 80 °C for 20 hours is repeated for another round (re-heating) after it cools down.

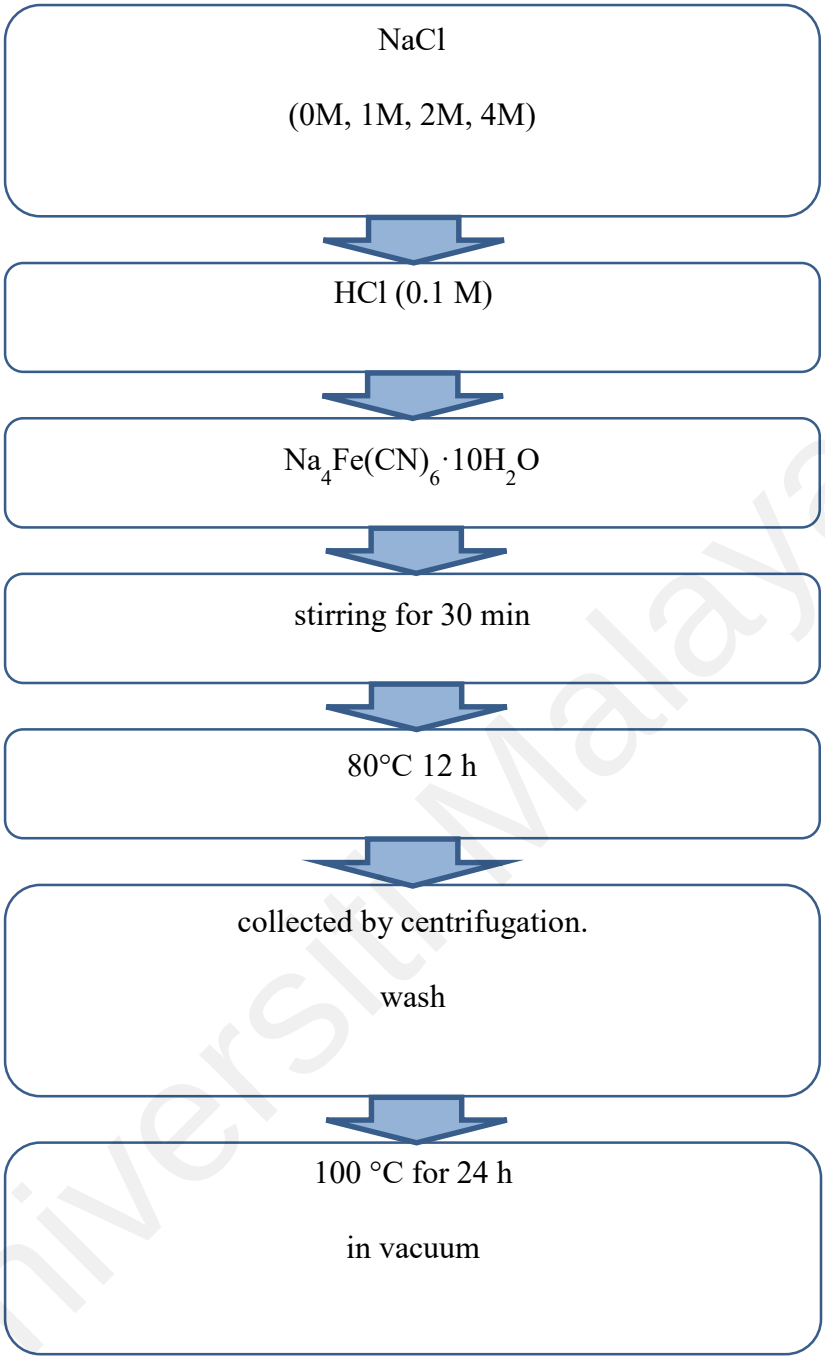

Figure 3.1: The process of synthesis of Na-rich PBA.

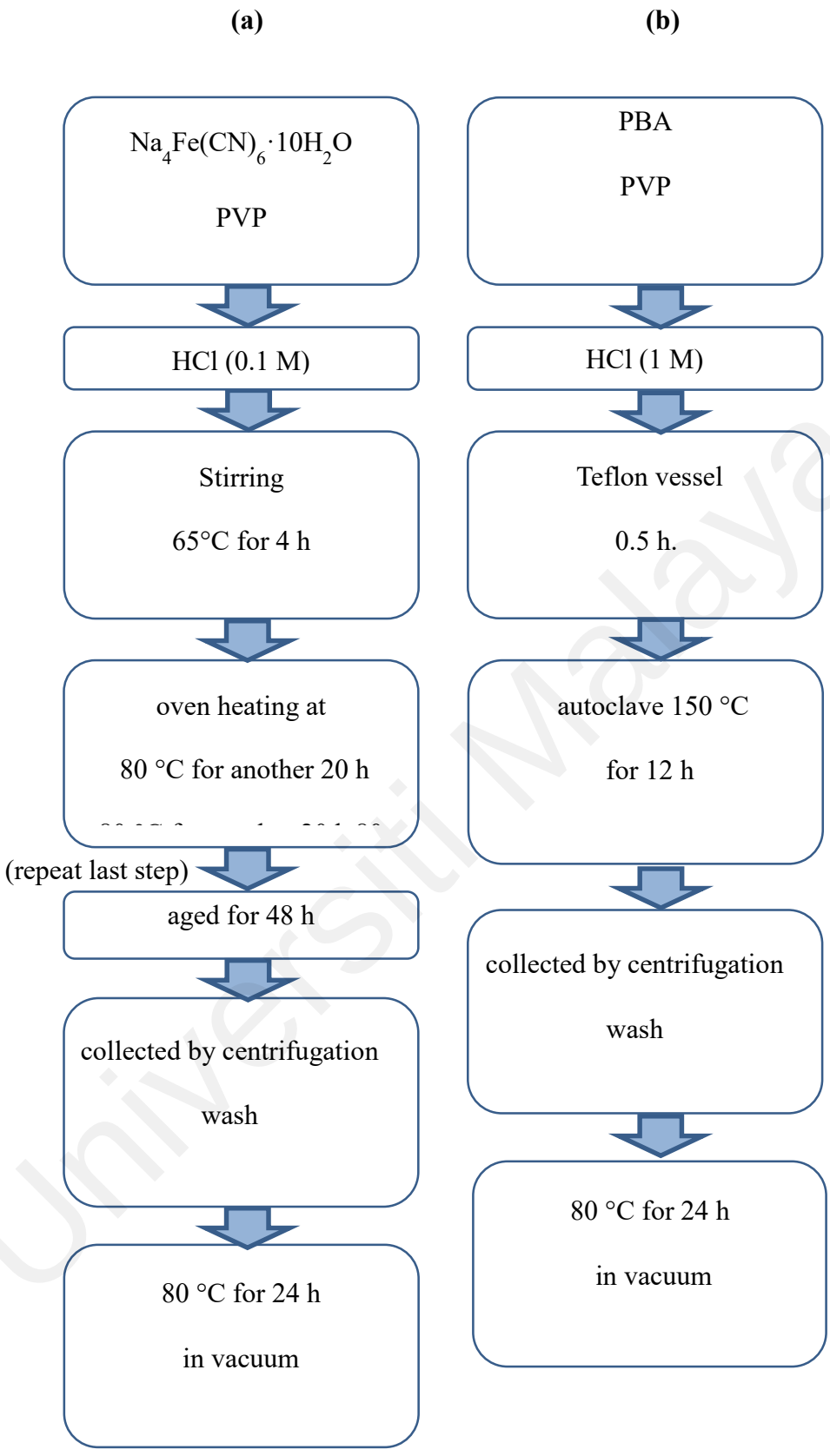

Figure 3.2: (a) The synthesize process PBA precursor of and (b) the etching process of PBA (The oven heating at 80 °C for another 20 h was repeated to obtain PB-C).

3.2.2 Synthesis Of P2-type Transition Metal Oxides

In this study, we employed a solid-state method to synthesize the target P2-type TMO materials. The synthesis process is depicted in Figure 3.3. The precursor, $Ni_{0.33}Mn_{0.67}(OH)_2$, was synthesized through a co-precipitation method. In this method, an aqueous solution containing stoichiometric amounts of $Ni(CH_3COO)_2 \cdot 4H_2O$ and $Mn(CH_3COO)_2 \cdot 4H_2O$ was co-precipitated with an aqueous solution of NaOH (1 M) and $NH_3 \cdot H_2O$ (0.1 M). The pH value of the slurry was maintained at 11, and the mixture was continuously stirred at 60 °C for 12 hours. The resulting powder was filtered, washed with water, and dried under vacuum conditions. Next, stoichiometric amounts of the dried $(Ni_{0.33}Mn_{0.67})(OH)_2$ powder and Na_2CO_3 were thoroughly mixed using ball-milling. The mixture was then calcined at 500 °C for 5 hours, followed by a second calcination at 850 °C for 24 hours with a heating rate of 5 K min^{-1}, resulting in the formation of $Na_{0.67}Ni_{0.33}Mn_{0.67}O_2$ (NM) material. For samples with Li substitution, Mg substitution, and Li/Mg co-substitution, denoted as LNM, MNM, and LMNM, respectively, LiOH and/or MgO precursors were added during the ball milling process according to the target stoichiometric compositions while maintaining the other conditions the same. To provide a clearer understanding of the number of starting materials used, Table 3.1 presents an example for each of the as-prepared P2-type TMO materials.

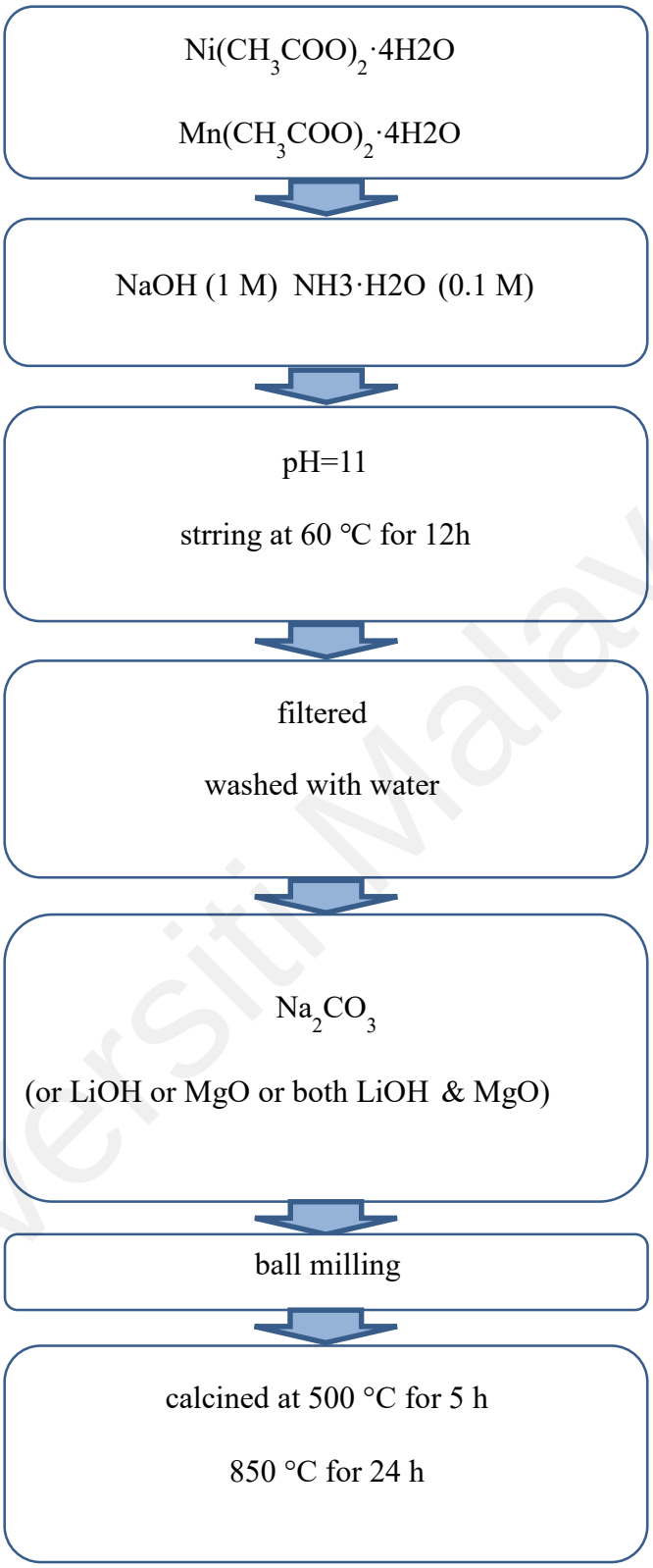

Figure 3.3: The process of synthesis of P2-type TMO.

Table 3.1: The ratios of starting materials of P2-type TMO.

Material	NM (mmol)	LNM (mmol)	MNM (mmol)	LMNM (mmol)
$Ni_{0.33}Mn_{0.67}(OH)_2$	0.9	0.9	0.9	0.9
Na_2CO_3	0.335	0.335	0.335	0.335
LiOH	/	0.1		0.05
MgO	/		0.1	0.05

3.3 Material Characterizations Section

3.3.1 Elemental Analysis

Elemental analysis is a method used to identify the types of elements present in a sample and determine the ratio of each element. Common elements analyzed include carbon (C), hydrogen (H), nitrogen (N), and others. The analytical procedure involves combusting the sample in the presence of catalysts and in an oxygen-enriched atmosphere, resulting in the formation of carbon dioxide, water, and nitrogen oxides. The nitrogen oxides are then reduced to nitrogen, and these components are separated and quantified using a thermal conductivity detector. This analytical technique allows for the precise determination of elemental composition in the sample.

The procedure for elemental analysis is shown in Figure 3.4. (Farina, Piergallini, Doldo, Salsano, & Abballe, 1991) The use of this instrument can automatically determine the content of carbon (C), hydrogen (H), and nitrogen (N) in a sample. This can be done either in a dynamic or static mode. The sample is combusted in a helium atmosphere

enriched with oxygen. The combustion products are then separated using a programmed temperature desorption system, and the concentrations of C, H, and N are measured using a thermal conductivity detector. By conducting elemental analysis, the aim is to confirm the formula of the PBA material, with particular focus on determining the presence and ratio of interstitial water within PBA. This analytical technique provides valuable information regarding the composition of the PBA material, specifically the relative amounts of carbon, hydrogen, and nitrogen, which can help confirm the molecular structure and the presence of interstitial water within PBA.

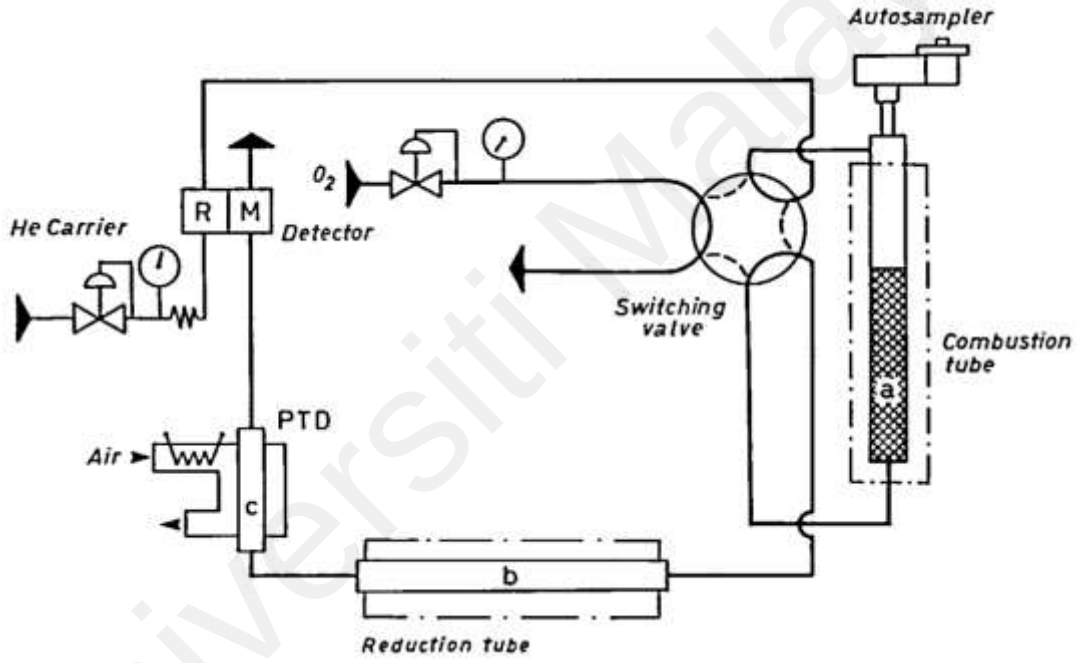

Figure 3.4: Scheme of elemental analyzer; tube fillings: (a) chromium oxide, cobalt (II, III) oxide, silver tungstate, silver gauze; (b)copper wire, silver gauze; (c) molecular sieve (Farina et al., 1991).

3.3.2 Inductively Coupled Plasma Mass Spectrometry (ICP-MS)

Inductively coupled plasma (ICP) has emerged as the primary method for multi-element analysis due to its exceptional attributes, including a broad linear dynamic range, low detection limits, and high precision. The ICP involves the generation of a partially ionized gas within a quartz torch. Samples are typically introduced into the central region of the plasma after atomization. The emitted light from the plasma is focused onto the

entrance slit of a monochromator or polychromator, allowing for the simultaneous detection of emission from various elements. Spectra from singly charged ions are typically strong for most elements, while spectra from atoms are more pronounced for elements with higher ionization potentials and the alkali metals. After the spectral analysis, the elements of interest are detected using a mass spectrometer (MS), which further enhances the sensitivity and specificity of the analysis. The combination of ICP and MS enables accurate and efficient detection and quantification of multiple elements in a sample. This analytical technique is widely employed in various fields for elemental analysis and has significantly contributed to scientific research and industrial applications.

As show in Figure 3.5, a 2 or 3 stage, A differentially pumped interface is utilized to transfer ions from the atmospheric-pressure plasma to the low-pressure mass spectrometer. This interface enables the efficient extraction of ions by maintaining a pressure gradient between the plasma region and the mass spectrometer. The process involves the passage of ions through a water-cooled nickel (Ni) or copper (Cu) sampling cone with an orifice, which is positioned within the plasma region. The sampling cone serves as the initial interface between the plasma and the mass spectrometer, allowing the ions to enter the low-pressure environment. To further optimize the ion transfer, a skimmer is employed. The skimmer is a cone with a sharper angle compared to the sampling cone. It is positioned downstream from the sampling cone, allowing only a small fraction of the expanding gas to pass through. The skimmer serves as a differential pumping stage, helping to maintain the pressure gradient and ensure efficient ion transmission into the mass spectrometer. By utilizing a differentially pumped interface with sampling and skimmer cones, the system can effectively extract ions from the atmospheric-pressure plasma and introduce them into the low-pressure mass spectrometer for analysis. This interface plays a crucial role in facilitating the transfer of ions while

maintaining the desired pressure conditions for accurate mass spectrometric measurements (Olesik, 1991). In this study, ICP-MS was used to analyze the element of as prepared samples.

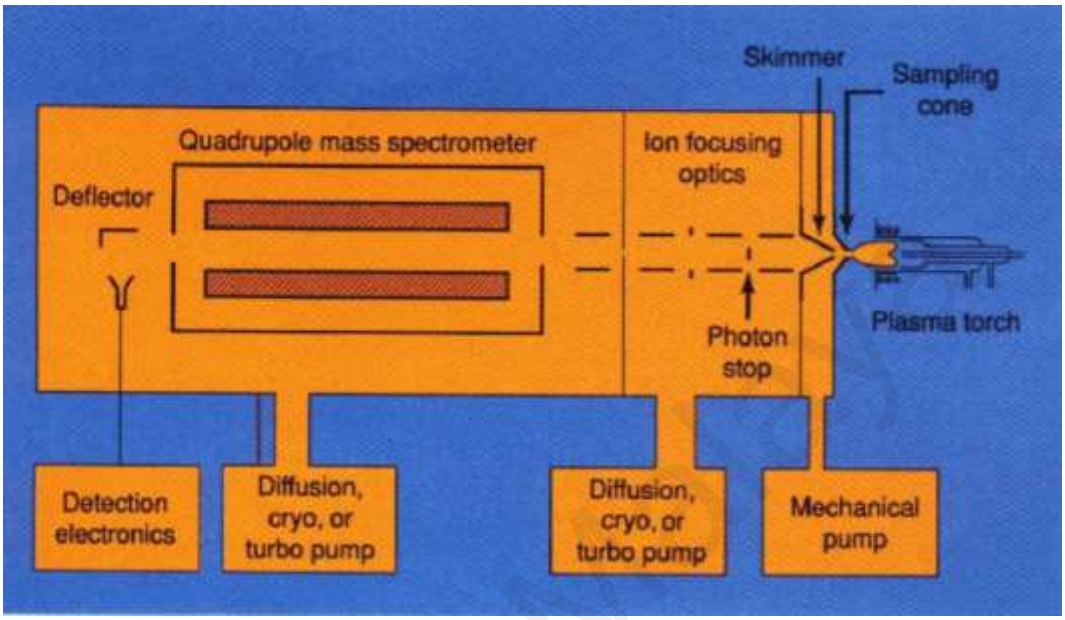

Figure 3.5: An ICP/MS instrument (Olesik, 1991).

3.3.3 Thermogravimetric Analysis (TGA)

TGA is a technique used to determine the stability and volatile components of materials. TGA measures the amount and rate of change in the mass of a material as a function of temperature or time because the sample is subjected to a controlled temperature program in a controlled atmosphere. This technique can be used to analyze materials that exhibit mass loss or gain due to decomposition, oxidation, or loss of volatiles (such as moisture). A TGA consists of a sample pan supported by a precision balance, which resides in a furnace and is heated or cooled during the experiment. Typical arrangements of the components for TGA are shown in Figure 3.6 (Saadatkhah et al., 2020). The sample is loaded from the bottom (hang down), top, or side.

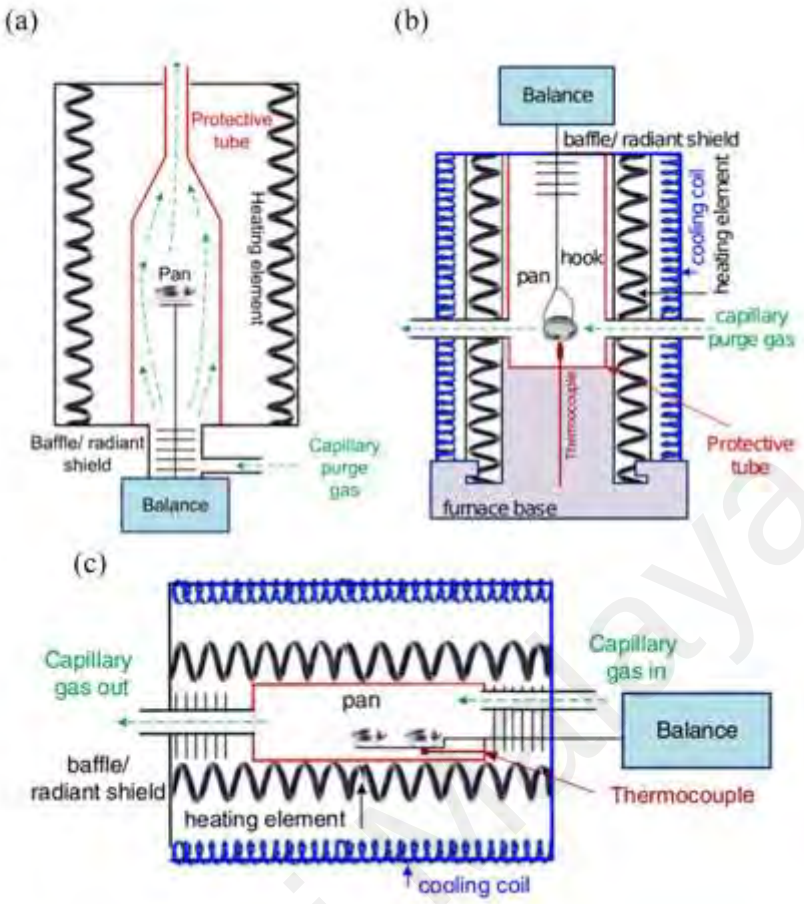

Figure 3.6: (a) Top loading configuration, (b) Bottom loading or hang down configuration and (c) Side loading configuration for TGA (Saadatkhah et al., 2020).

A TG curve or thermogram is a graphical representation of the sample's mass change versus temperature or time. Thermograms are unique for each compound and provide information about the thermal stability, oxidative stability, multi-component composition, product lifetime, decomposition kinetics, moisture content, and volatile content of a material. Figure 3.7 shows a typical thermogram with several sections:

1. Below 150°C, physisorbed water, low molecular weight volatile compounds, solvents, and trapped gases are released.

2. Between 150°C and 250°C, mass loss is attributed to chemisorbed water and low molecular weight compounds such as additives and volatile decomposition products.

3. Above 250°C, compounds begin to decompose within the temperature range from the onset to the endset. For multi-component systems and reactions with intermediate steps, there can be multiple onset and endset temperatures.

4. The remaining material above the endset temperature consists of non-volatile inorganic ashes and metals.

5. In an oxidizing environment, metallic compounds undergo oxidation and gain mass by increasing their oxidation state.

In this work, TGA was carried out to study the fraction of water and the thermal stability.

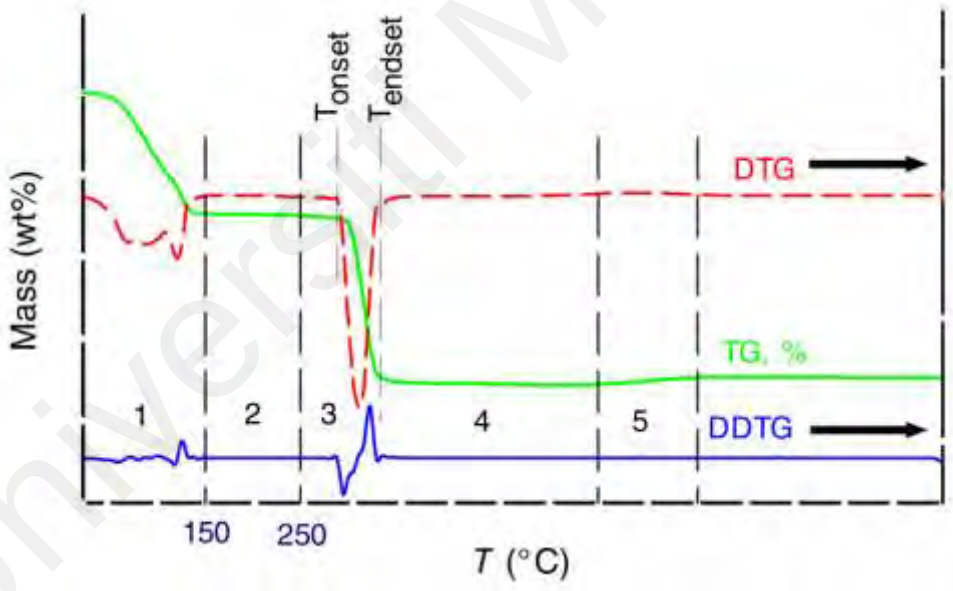

Figure 3.7: Five possible sections of a thermogram (TG curve (green), DTG curve, first derivative (red), DDTG curve, second derivative (blue) of $Mn(CH_3CO_2)_2 .4H_2O$ heated up to 900 ℃ in air). (Saadatkhah et al., 2020)

3.3.4 Brunauer-Emmett-Teller (BET)

The specific surface area is the most effective method for describing the external surface area of a solid object. Gas adsorption provides a distinct advantage because many classical methods for particle measurement and characterization fail to consider porosity.

Physisorption is generally a weak and reversible process. To estimate the monolayer coverage and calculate the surface area, the solid should be cooled, and a method should be used to measure the amount of gas/vapor required to form the monolayer, taking into account the dimensions and number of molecules.

The schematic diagram of the volumetric method is shown in Figure 3.8. Nitrogen is typically used as the adsorbate gas for the volumetric method. It is introduced into the evacuated space above the powdered sample to establish a defined equilibrium pressure (P) of the gas. The use of a diluent gas, such as helium (He), is unnecessary for this purpose, although helium may be employed for other purposes, such as measuring the dead volume.

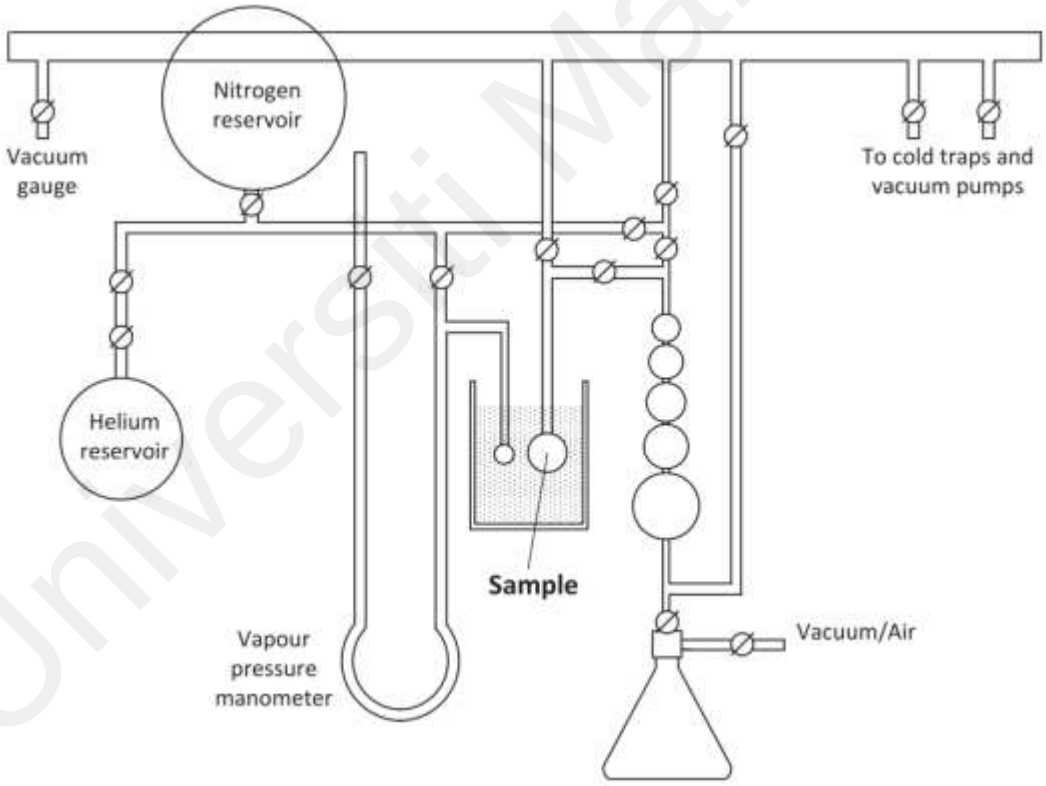

Figure 3.8: Schematic diagram of the volumetric method apparatus (Naderi, 2015).

In this study, Micrometrics ASAP 2020 was used to carried out the specific surface area of the samples from N_2 adsorption-desorption isotherm. The specific surface area was calculated using the conventional Brunauer-Emmett-Teller (BET) formula while micropore volume can be achieved with the t-plot method. The pore size distribution,

total pore volume and average pore width are carried out by Barrett-Joyner-Halenda (BJH) method.

3.3.5 Fourier Transform Infrared (FTIR)

FTIR spectroscopy is a useful technique used to determine qualitative and quantitative features of IR-active molecules in organic or inorganic solid, liquid, or gas samples by observing the vibrational transitions associated with specific functional groups (Isayev, 2010). IR (infrared) radiation is a type of electromagnetic radiation that lies between visible light and radio waves on the electromagnetic spectrum. When a material is irradiated with IR radiation, the absorbed IR radiation usually excites molecules into a higher vibrational state. The wavelength of light absorbed by a particular molecule is determined by the energy difference between the resting and excited vibrational states. The wavelengths absorbed by the sample reflect the characteristics of its molecular structure. The infrared region of the electromagnetic spectrum extends from 14,000 to 10 cm^{-1}, and the region of most interest for chemical analysis is approximately 4,000 to 400 cm^{-1}, which corresponds to change in vibrational energies within molecules (Urtubia, Pérez-correa, Pizarro, & Agosin, 2008).

The components of an IR instrument basically consist of an interferometer, a source, a sample compartment, a beam splitter, a detector, an analog-to-digital converter, and a digital machine for quantifying the data (Skoog, Holler, & Crouch, 2007). Figure 3.9 shows the schematic diagram of an FTIR spectrometer. Infrared light emitted from a source is directed into an interferometer, which modulates the light. After passing through the interferometer, the light travels through the sample compartment and the sample and is then focused onto the detector. The signal measured by the detector is called the interferogram. The measured signal is digitized and sent to the computer, where the Fourier transformation takes place. FTIR spectra are usually presented as plots of

intensity versus wavenumber, which is the reciprocal of the wavelength. The intensity can be plotted as the percentage of light transmittance or absorbance at each wavenumber. In this study, FTIR is used to confirm the presence of the OH group.

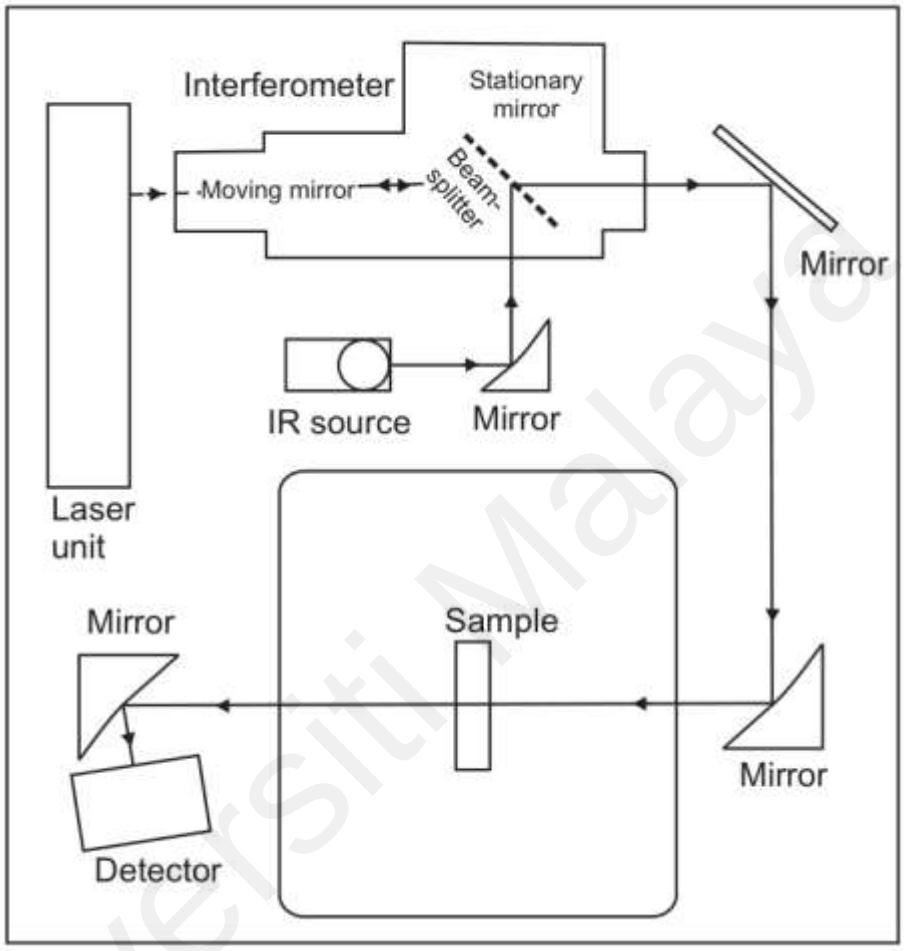

Figure 3.9: IR spectrometer with the source, interferometer, sample, and detector (King, Ramsey, McMillan, & Swayze, 2004).

3.3.6 X-Ray Diffraction (XRD)

XRD is a command technique to study of crystal structures and atomic spacing. The schematic diagram of a diffractometer system is shown is Figure 3.10. X-ray diffractometers consist of three basic elements: an X-ray cathode ray tube, a sample holder, and an X-ray detector (Bunaciu, Udriştioiu, & Aboul-Enein, 2015). The X-ray is generated by a cathode ray tube and then filtered to produce monochromatic radiation. It

is then collimated to concentrate the X-ray beam and finally directed towards the sample. When the conditions satisfy Bragg's law

$$\boldsymbol{\alpha = \frac{\lambda}{2\theta\sqrt{h^2+k^2+l^2}}} \quad \textbf{(3.1)}$$

Where α is lattice parameter, θ is diffraction angle, λ is incident wavelength, (h, k, l) is Miller index.

The interaction of the incident rays with the sample produces constructive interference, resulting in the formation of a diffracted ray. Bragg's law relates the wavelength of electromagnetic radiation to the diffraction angle and the lattice spacing in a crystalline sample. To obtain information about the lattice structure of the sample, it is necessary to scan the sample through a range of 2θ angles. This allows for the attainment of all possible diffraction directions of the lattice due to the random orientation of the powdered material. Once detected, processed, and counted, a diffraction spectrogram is obtained, which displays characteristic peaks. These peaks can then be converted to d-spacings and compared with standard reference patterns to identify the material, as each material has a unique set of d-spacings.

XRD is a fundamental, high-tech, nondestructive technique used for analyzing a wide range of materials, including liquids and solids. In this study, XRD will be applied to confirm the structure of the as-prepared samples.

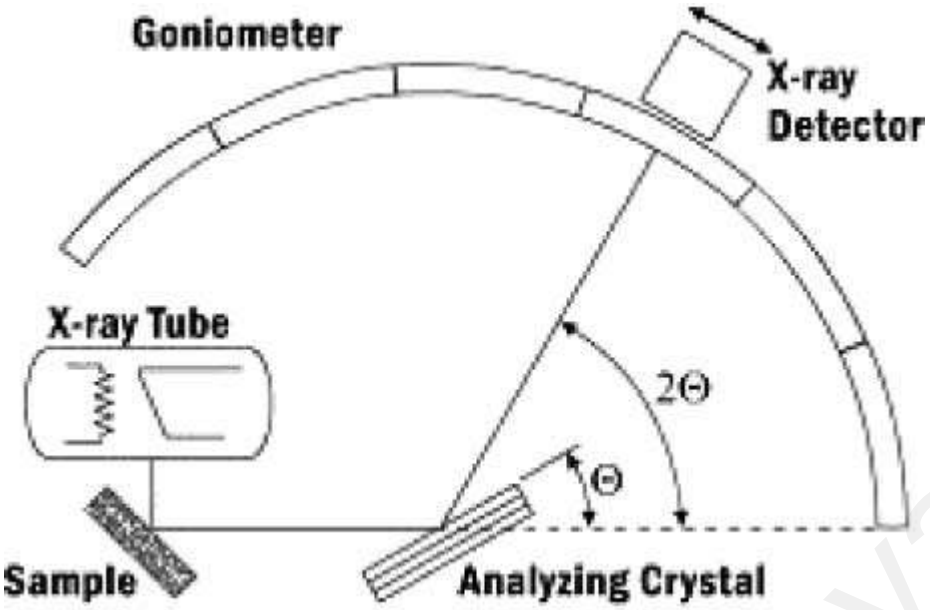

Figure 3.10: Schematic diagram of a diffractometer system (Bunaciu et al., 2015).

In-situ XRD, or in-situ X-ray diffraction, is a valuable technique used to study the structural changes that occur in electrode materials during dynamic processes. The mechanism and introduction of this technique have been explained in the previous chapter. In the current study, in-situ XRD was conducted specifically during charge-discharge cycles.

As shown in Figure 3.11Figure 3.11, the cion cell case includes a window, and the coil cell undergoes charge and discharge cycles as usual. Throughout this process, X-rays are directed towards the sample, and the resulting reflections are captured by the X-ray detector. Consequently, a series of XRD patterns can be collected, allowing for the observation of the continuous structural evolution of the materials. In the present study, XRD was employed to investigate the structural parameters of the as-prepared samples.

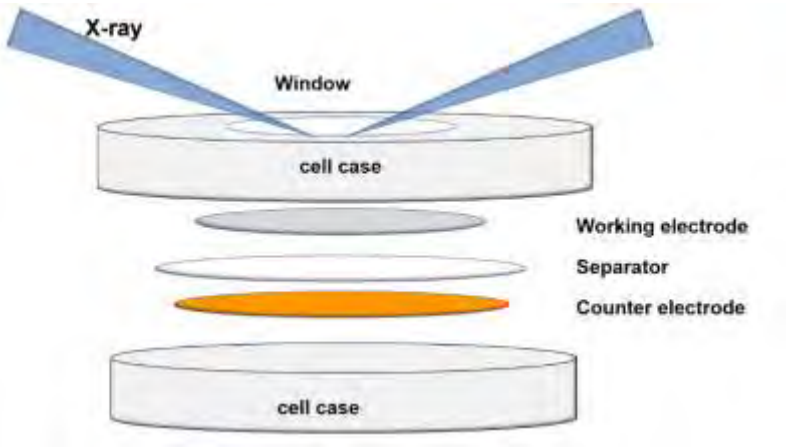

Figure 3.11: The schematic diagram of in-situ XRD cell.

3.3.7 High Resolution Transmission Electron Microscope (HRTEM) and Field Emission Scanning Electron Microscope (FESEM)

HRTEM and FESEM are common methods used to investigate the morphology of materials with nanometer-level resolution. Both techniques were employed in this study to examine the morphology properties of the samples. HRTEM images were acquired using the JEOL JEM-2100F microscope. These images were analyzed to estimate the particle size of the as-prepared samples. Additionally, elemental analysis and Energy Dispersive X-ray Spectroscopy (EDX) were performed using the same microscope to determine the composition of the samples and identify any vacancies or elemental constituents.

3.3.8 X-Ray Photoelectron Spectroscopy (XPS)

The principle of XPS (X-ray Photoelectron Spectroscopy) involves irradiating the sample with X-rays, which leads to the excitation of inner or valence electrons of atoms or molecules. These excited electrons, known as photoelectrons, are then detected, and their energies are recorded. The recorded kinetic energy/binding energy of the photoelectrons is plotted on the horizontal axis, while the relative intensity is plotted on the vertical axis.

The photoelectric effect, which forms the basis of XPS, has been developed into a powerful tool for studying the composition and electronic structure of matter since the 1950s. In recognition of the development of high-resolution XPS, Kai Siegbahn was awarded the Nobel Prize in 1981. In recent years, there have been significant advancements in the XPS technique, including new measurement modes and more precise theoretical interpretation methodologies. Figure 3.12 provides a schematic representation of some key aspects of the XPS experiment, highlighting new directions of development (Fadley, 2010).

In this work, XPS was used to determine the different states of elements.

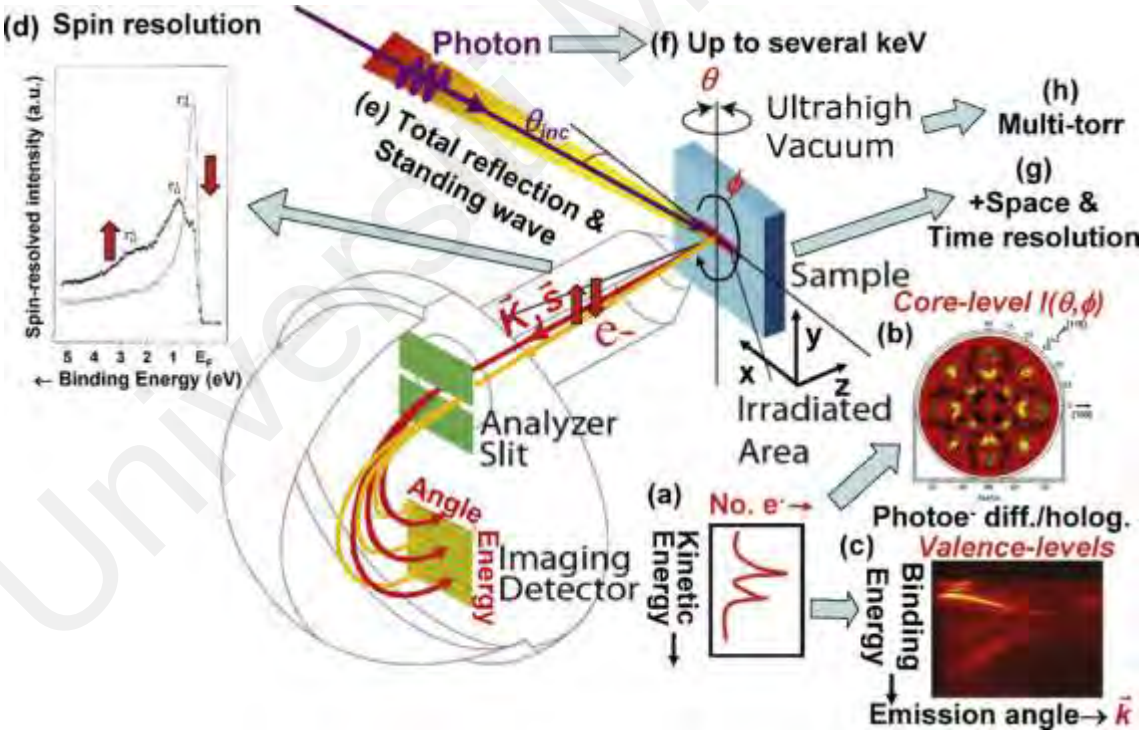

Figure 3.12: Illustration of a typical experimental configuration for X-ray photoelectron spectroscopy experiments, together with the various types of measurements possible, including (a) simple spectra or energy distribution curves, (b) core-level photoelectron diffraction, (c) valence-band mapping or binding energy vs $\vec{k}$ plots, (d) spin-resolved spectra, (e) exciting with incident X-rays such that there is total reflection and/or a standing wave in the sample, (f) using much higher photon energies than have been typical in the past, (g) taking advantage of space and/or

time resolution, and (h) surrounding the sample with high ambient sample pressures of several torr (Fadley, 2010).

3.3.9 Neutron Profile Depth (NPD)

NDP is a non-destructive analytical technique that relies on the interaction between a beam of neutrons and specific elements, such as lithium, within a sample. The neutrons used in NDP are delivered through a neutron guide to the NDP facility.

With the rapid development of neutron sources, neutron diffraction-based characterization techniques have become widely utilized in material research. The mechanism of neutron diffraction is similar to that of X-ray and electron diffraction, as it is based on the Bragg equation. This gives neutrons greater penetrability, allowing for detection of samples with centimeter-level thickness. Upon interaction with the nuclei, isotropic scattering occurs, and the scattering amplitude is only related to the size and orientation of the atomic magnetic moment, not the atomic number of the nucleus. As a result, NDP can accurately identify the elemental composition of the measured sample.

Figure 3.13 provides a schematic of the NDP facility. The sample is attached to an aluminum disk, which is vertically held at the center of a vacuum chamber using grooves on the sample mount. The sample is positioned to face the surface-barrier type charged particle detector. When neutrons are absorbed by elemental atoms in the sample, monoenergetic charged alpha and triton particles are emitted and travel in opposite directions from the reaction site. These charged particles do not lose any energy after leaving the sample's surface as they travel towards the detectors (Nagpure, Downing, Bhushan, Babu, & Cao, 2011).

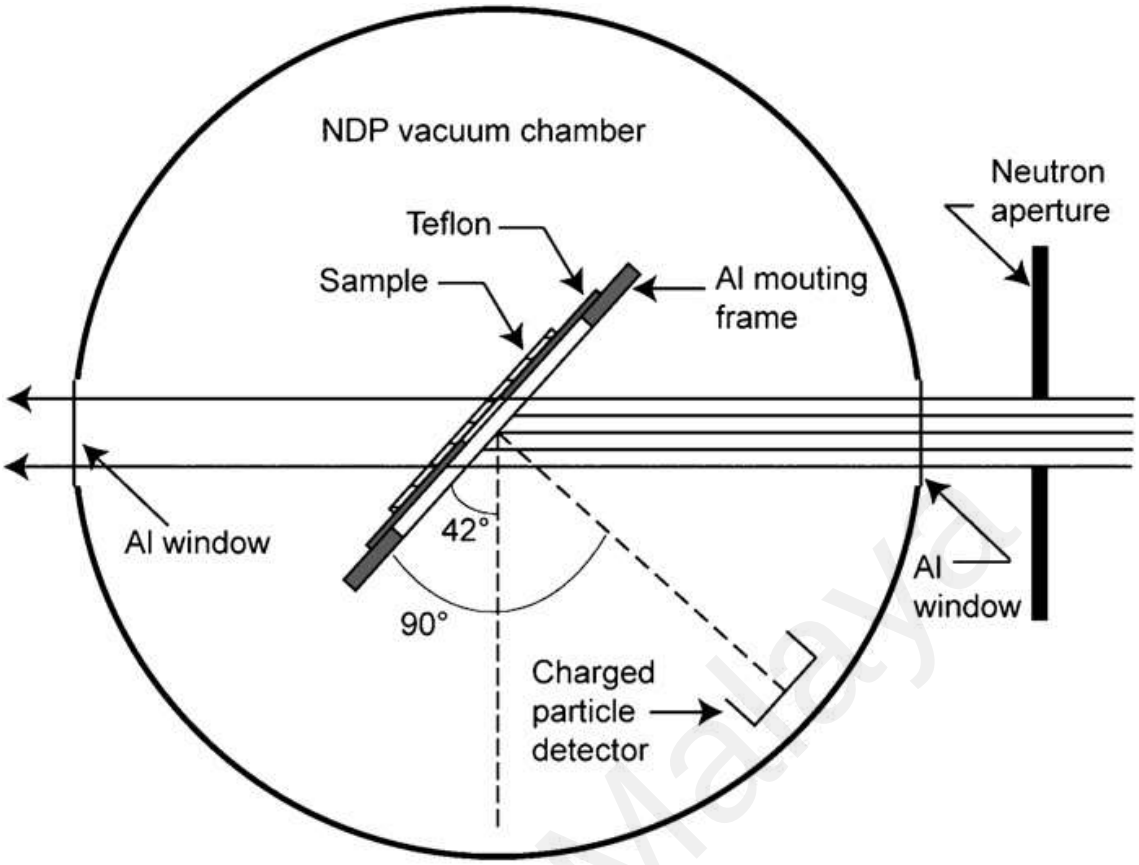

Figure 3.13: Schematic of the NDP facility. (Nagpure et al., 2011)

3.4 Electrochemical Characterization of SIBs

3.4.1 The Preparation of Cell

In this study, the focus was on the cathode material. To assemble the half-cell, a sodium metal anode was used. Table 3.2 provides the composition ratios for preparing the working electrode. The slurry was prepared by mixing polyvinylidene fluoride (PVDF), active material, and Super P in a ratio of 8:1:1. N-methyl-2-pyrrolidone (NMP) was used as the mixing solvent, and the slurry was stirred for 24 hours. After stirring, a dark slurry was obtained. The slurry was then coated onto aluminum foil using a doctor blade, with a slurry loading of approximately 10 mg/cm^2. The foil with the slurry was subsequently transferred to a vacuum oven for drying. After drying, the mass loading of the active material on the foil was approximately 2 mg/cm^2. For the electrolyte, a solution of 1.0 M sodium hexafluorophosphate (NaPF6) in a mixture of ethylene carbonate (EC) and propylene carbonate (PC), with 5% fluoroethylene carbonate (FEC), was used. The

electrolyte was applied at a volume of 80 µl per cell. The assembly of the half-cell was carried out in a glovebox filled with argon gas, ensuring that the levels of oxygen and moisture were lower than 1 ppm. A glass fiber acted as the separator, and a sodium foil served as the counter electrode. The cell fabrication order is depicted in Figure 3.14.

Table 3.2: The ratio of slurry.

	Active material	Active carbon	PVDF	NMP
Mass	0.8 g	0.1 g	0.1 g	4 g

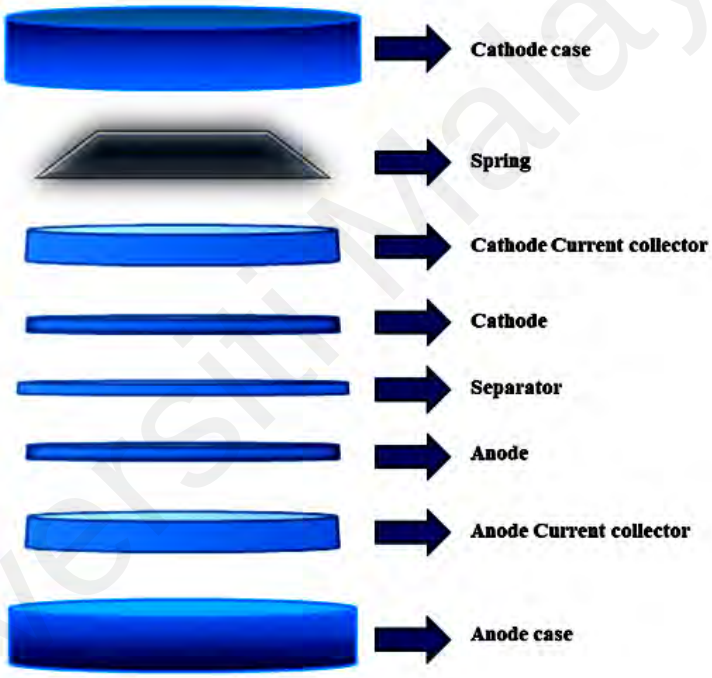

Figure 3.14: Fabrication of SIB cell.

3.4.2 Cyclic Voltammetry (CV)

CV is a widely used electrochemical method that involves controlling the potential of an electrode while measuring the resulting current at various scan rates. This is achieved by applying a triangular waveform to the electrode over a specified period. By obtaining a potential-current curve within a certain voltage range, valuable information about the reversibility of electrode-electrolyte reactions and the characteristics of coupling

reactions can be obtained. CV is commonly employed to determine parameters related to electrode chemical reactions, identify the rate-controlling steps, and gain insights into reaction mechanisms.

CV is considered one of the most versatile techniques in electroanalysis and finds applications in various fields such as electrochemistry, inorganic chemistry, organic chemistry, and biochemistry. It is often the initial experiment conducted to study the electrochemical behavior of a compound, a biological material, or an electrode surface. The strength of CV lies in its ability to rapidly observe redox behavior.

In the context of battery systems, CV is frequently employed to identify redox peaks and assess the level of polarization. It is also used to investigate diffusion coefficients, providing valuable insights into the transport properties of species within the battery.

3.4.3 Electrochemical Impedance Spectroscopy (EIS)

EIS is a technique used to study the interface reaction between an electrode and electrolyte in electrochemical systems. EIS involves applying a small sinusoidal excitation signal to the system and measuring the resulting current response across a range of frequencies. In a linear or pseudo-linear system, the current response to the sinusoidal potential excitation will also be a sinusoid at the same frequency but with a phase shift. By analyzing the amplitude and phase of the current response as a function of frequency, valuable information about the electrochemical processes occurring at the electrode-electrolyte interface can be obtained. EIS provides insights into various electrochemical phenomena, including charge transfer resistance, double-layer capacitance, diffusion processes, and other interface properties. It is a powerful tool for characterizing and understanding the behavior of electrochemical systems, such as batteries, fuel cells, corrosion processes, and electroplating processes (Figure 3.15).

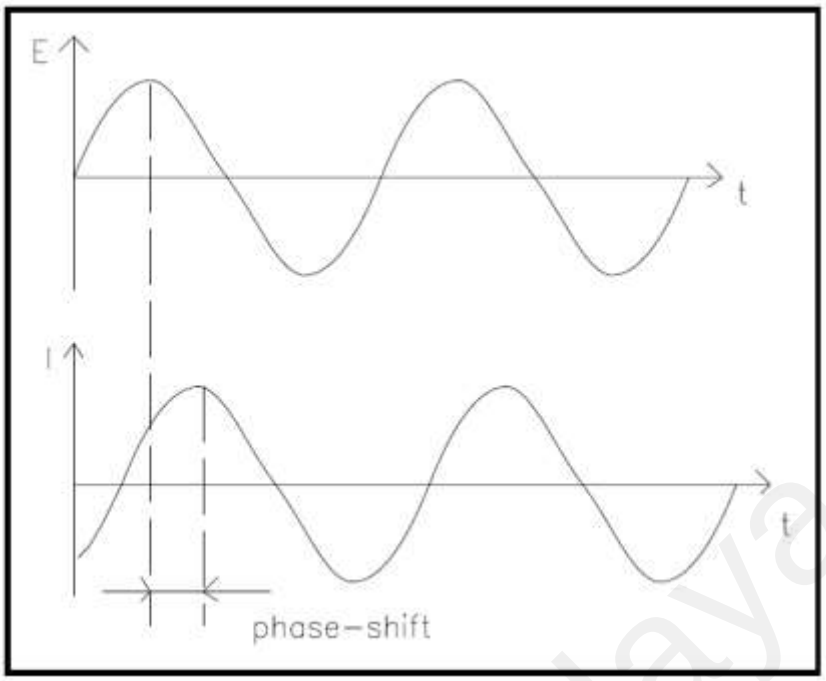

Figure 3.15: Sinusoidal current response in a linear system.

The impedance is represented as a complex number:

$$\boldsymbol{Z(\omega) = \frac{E}{I} = Z_0 exp(j\emptyset) = Z_0(\cos\emptyset + j\sin\theta) = Z_r + jZ_i} \qquad \textbf{(3.2)}$$

Where $\boldsymbol{Z_r}$ is the real part of the impedance and Z_i is the imaginary part.

The expression for $\boldsymbol{Z(\omega)}$ is composed of a real and an imaginary part. If the real part is plotted on the Y-axis and the imaginary part is plotted on the Y-axis of a chart, we get a "Nyquist Plot" (Figure 3.16). Notice that in this plot the Y-axis is negative and that each point on the Nyquist Plot is the impedance at one frequency. Figure 3.16 has been annotated to show that low frequency data are on the right side of the plot and higher frequencies are on the left.

On the Nyquist Plot the impedance can be represented as a vector (arrow) of length $\boldsymbol{|Z|}$. The angle between this vector and the X-axis, commonly called the "phase angle", is $\emptyset$ (=arg Z).

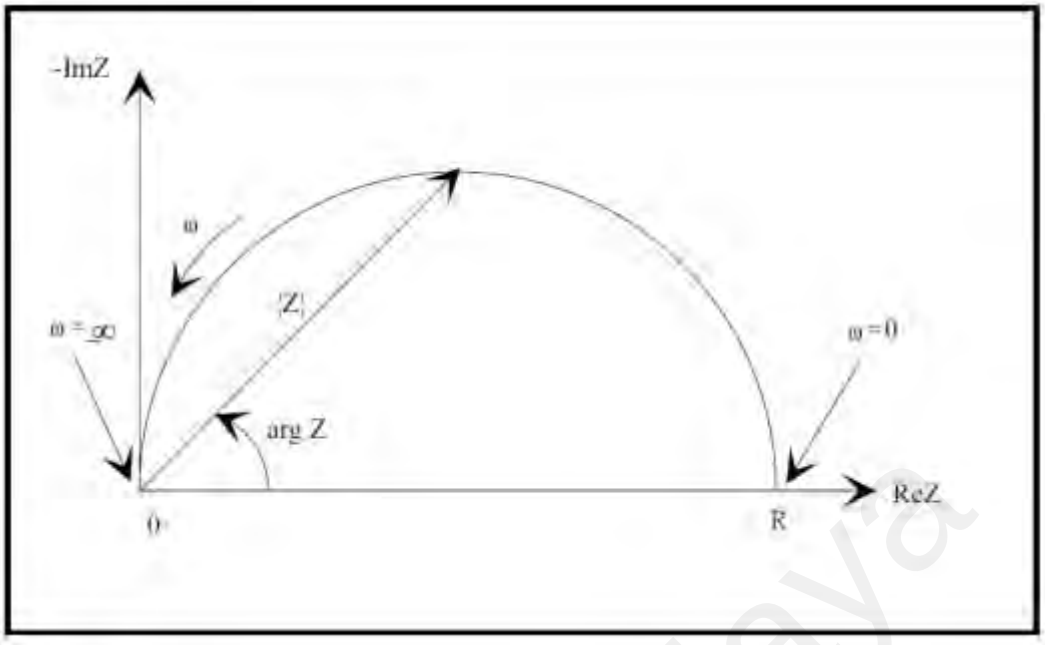

Figure 3.16: Nyquist Plot with Impedance Vector.

In a classical battery system, Nyquist plot shows two semicircles and a radial line. As shown in Figure 3.17, R_s is the ohmic resistance of the system. The first semicircle presents the ions transportation process through the solid electrolyte interphase (SEI). Second semicircle presents the transportation of charges while the radial line presents the diffusion of ions inside the active materials.

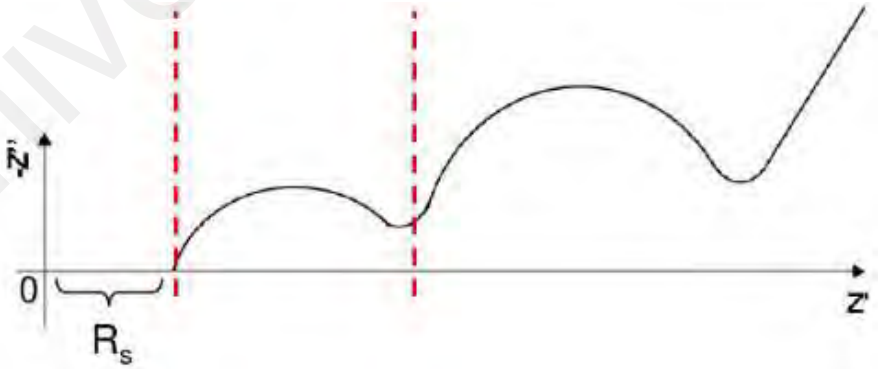

Figure 3.17: Classical Nyquist plot of batteries system.

In an open circuit situation, a different frequency sinusoidal signals are added to the half-cell and the resistance corresponding to the frequency can be detected. The results can help to analyze the kinetics of the batteries system during the GCD. The EIS

measurement is recorded in the frequency between 0.1 - 100 kHz. The Diffusion coefficient D can be calculated by

$$\boldsymbol{D = R^2T^2/2A^2n^4F^4C^2\sigma^2} \tag{3.3}$$

$$\boldsymbol{Z_{re} = R_s + R_{ct} + \sigma\omega^{\frac{1}{2}}} \tag{3.4}$$

Where, n is the amount of transfer electron during the redox process, F is faraday constant, R is gas constant, A is the superficial area of the electrode, D is diffusion coefficient of Na^+, C is sodium ionic concentration, T is absolute temperature, σ is Warburg coefficient. Z_{re} is real impedance, Rs is the SPE resistance, ω is angular frequency, R_{ct} is charge transfer resistance(S. Li et al., 2014). From the equation above, σ^2 is inversely proportional to diffusion coefficient D at the same other conditions.

3.4.4 Galvanostatic Charge/Discharge (GCD)

GCD is a widely used technique for evaluating the rechargeable performance of batteries. It involves applying a constant current to the battery within a specific potential range. During the charge process, a constant current is supplied to the battery until the desired voltage or potential limit is reached. This allows the battery to store electrical energy by driving the electrochemical reactions in the battery towards the direction of charging. In the discharge process, a counter current is applied to the battery to extract electrical energy. The battery discharges until the voltage or potential reaches a predetermined set value.

By performing GCD cycles, various performance parameters of the battery can be evaluated. The rate performance refers to how well the battery performs under different charge/discharge rates or currents. It indicates the ability of the battery to deliver or accept a charge at different rates. The cycling performance measures the stability and capacity

retention of the battery over multiple charge/discharge cycles. It assesses the durability and longevity of the battery under repeated cycling.

3.4.5 Galvanostatic Intermittent Titration Technique (GITT)

GITT is a transient measurement method with a process of pulse-galvanostatic-relaxation. Among them, the pulse refers to the process of passing a short current, and the relaxation refers to the process of no current passing. Within a time τ, a constant current I is applied to charge or discharge and then remove I. The voltage changes during the constant current process and the relaxation process are recorded.

The formula for calculating the diffusion coefficient is as follows,

$$D = \frac{4}{\pi\tau}\left(\frac{n_m V_m}{S}\right)^2 \left(\frac{\Delta E_s}{\Delta E_t}\right)^2$$

Where, D is the diffusion coefficient, τ is relaxation time, n_m is the mole number, V_m is the mole volume of electrode material, S is the surface between the electrode and the electrolyte, ΔE_s is the change of voltage during the pulse, ΔE_t is the change of voltage after one pulse.

3.5 Summary

- The synthesis of PBA with surface modification using the hydrothermal method.
- The synthesis of P2-type layer oxide with elemental substitution using the solid-state method.
- The structural and morphological characterization of the synthesized materials using techniques such as elemental analysis, ICP-MS, TGA, BET, FTIR, XRD, in-situ XRD, HR-TEM, SEM, XPS and NPD.
- The electrochemical characterization of SIBs using techniques such as CV, EIS, GCD and GITT.

CHAPTER 4: NA-RICH PRUSSIAN BLUE ANALOGUE AS CATHODE MATERIALS FOR SODIUM ION BATTERIES[1]

4.1 Introduction

In this chapter, we propose a simple method with solution coprecipitation to synthesize nano-size PBA particles. NaCl was used to control the Na^+ content and the morphologies of different products. With the increasing of Na^+ concentration, both the structure stability and the electrochemical performance were significantly improved.

4.2 Structural and morphological Characterizations of Na-rich PBA

To investigate the thermal stability of PBA materials, TGA was firstly studied. Figure 4.1 shows the TGA curve of each sample at the temperature range between 50 °C and 550 °C. Two plateaus and two rapid drops can be clearly observed.

The decomposition of PBA ($Na_xFe^{III}[Fe^{II}(CN)_6]_y \cdot nH_2O$) can be divided to 3 sections (Buser, Schwarzenbach, Petter, & Ludi, 1977; Y. Lu et al., 2012; Wilde, Ghosh, & Marshall, 1970; Zhou, Li, Xin, & Goodenough, 2017) as follow,

[1] **Chapter 4 of this thesis is published as:** Chen, Y., Woo, H. J., Rizwan, M., Yahya, R. b., Cui, D., Luo, D., . . . Wang, F. (2019). Nanoscale Morphology Control of Na-Rich Prussian Blue Cathode Materials for Sodium Ion Batteries with Good Thermal Stability. *ACS Applied Energy Materials, 2*(12), 8570-8579. doi:https://doi.org/10.1021/acsaem.9b01491

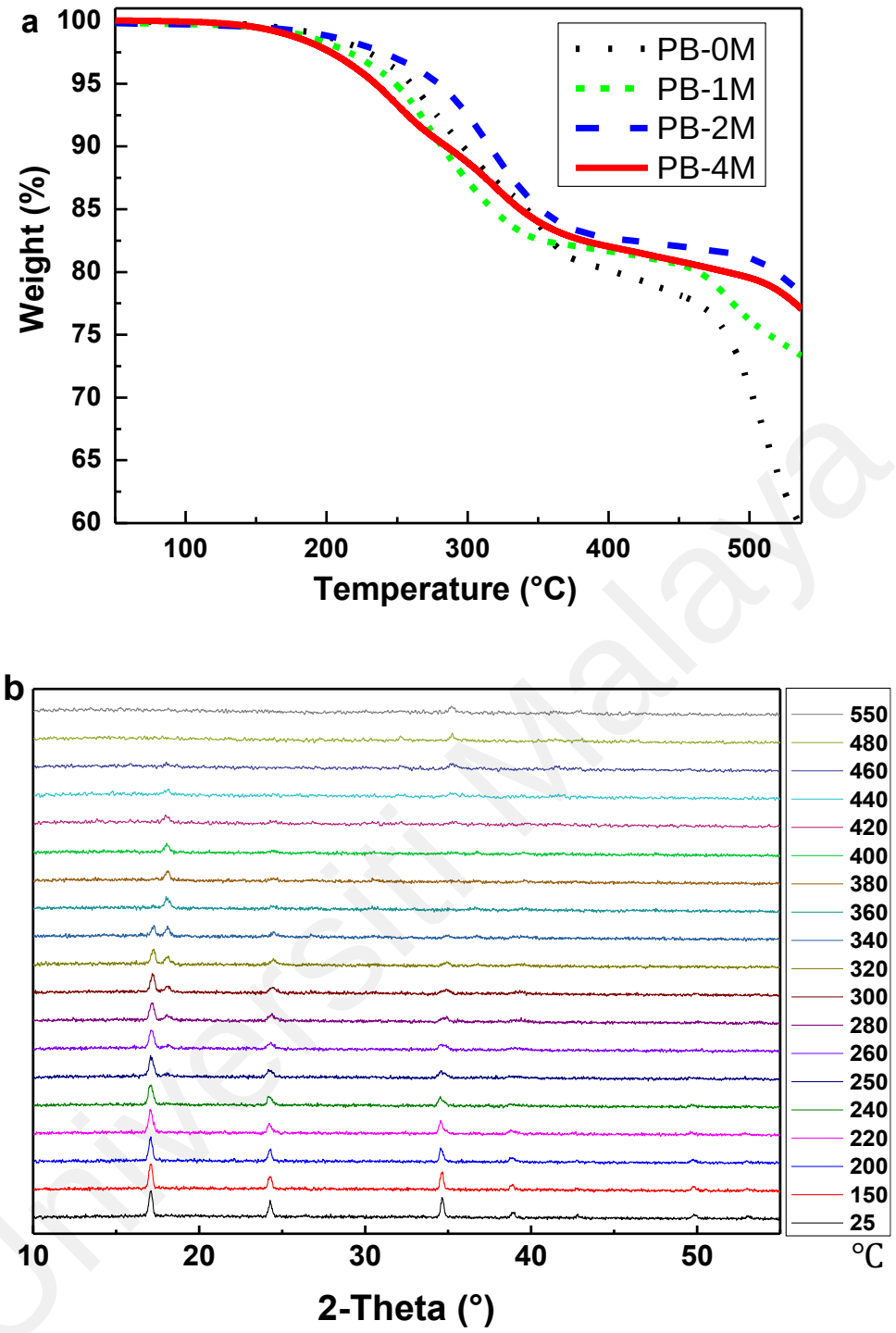

Figure 4.1: (a) The TGA curves comparison of all the samples and (b) in-situ XRD patterns of PB-4M at the temperature range between 25 °C and 550 °C.

.

Section 1:

$$Na_xFe^{III}[Fe^{II}(CN)_6]_y \cdot nH_2O \rightarrow Na_xFe^{III}[Fe^{II}(CN)_6]_y + nH_2O \quad (4.1)$$

Section 2:

$$Na_xFe^{III}[Fe^{II}(CN)_6]_y \rightarrow Na_xFe^{II}[Fe^{II}(CN)_6]_y + Fe^{II}[Fe^{II}(CN)_6]_y + (CN)_2 \quad (4.2)$$

Section 3:

$$Na_xFe^{II}[Fe^{II}(CN)_6]_y \rightarrow NaCN + Fe^{II}[Fe^{II}(CN)_6] \quad (4.3)$$

$$Fe^{II}[Fe^{II}(CN)_6] \rightarrow Fe_3C + C + N_2 + (CN)_2 \quad (4.4)$$

$$Fe^{II}[Fe^{II}(CN)_6] \rightarrow Fe_3C + C + N_2 \quad (4.5)$$

The reactions in the three sections are not separate, they may occur simultaneously. The first section involves the loss of absorbed water, which is performed at temperature ranging from 25 °C to 150 °C. During this stage, all the samples show no obvious loss of weight, suggesting that they contain little amounts of absorbed water. The second section is performed within the temperature range of 150 °C to 380 °C. During this stage, the structure of PBA starts to decompose and Fe^{III} reduces to Fe^{II}. Three samples, PB-0M, PB-1M and PB-2M, have shown a similar trend at this temperature range. As the Na content increases, the collapse of PB-4M tends to slow down. It should be noted that for PB-4M within the temperature range of 150 °C to 380 °C, two falling edges are observed. The slow collapse indicates that PB-4M is synthesized with the most stable structure among all the samples. The higher retention and ending temperature (~83% and 380 °C) might be resulted from the increased content of the Na^+ ions, which occupy in sites of the interstitial water and defects. At temperatures above 450 °C, the PBA structure starts to collapse, which continue until the temperature increases towards the end. In the temperature range between 450 °C and 550 °C, a rapid drop in weight can be clearly observed, due to the breakage of the C≡N bonds, particularly around 450 °C. Comparing

the weight loss among the samples, PB-2M and PB-4M exhibit similar retention based on TGA measurements, while PB-0M and PB-1M show obvious weight loss at 550 °C.

To better understand the detailed change of the PBA structure, PB-4M has been investigated via in-situ XRD at the temperature range between 50 °C and 550 °C. At the temperature below 150 ºC, the XRD pattern of the sample has almost no change. From 200 ºC above, subtle changes could be found on the XRD pattern caused by loss of the interstitial water. When the temperature increases to 250 ºC, a minor peak emerges, which implies the collapse of structure. This peak might belong to the product from the decomposition of PBA. The peak at 17° disappears when the temperature increases up to 360 ° C, and the new peak also disappears above 480 ° C. Associating to the in-situ XRD result of PB-4M, the first phase change is at around 240 - 250 ℃, where the peaks at 24 ° and 34° are weak and there is a new peak appear at around 23°, well corresponding to the first truing point from TGA curve. After this point, the TGA curve is become gently, indicating the totally consumption of water including absorbed water and interstitial water. So, the total amount of water of PB-4M is about 10%. To the contrary, for instance, PB-0M, there is no any obvious turning point up to the temperature of 360 ℃, implying that the water may still exist upon the heating process until the temperature up to 360 ℃. And the total mass lost during the section is about 20%. In addition, interstitial water is more difficult to remove from the lattice because it might be held by chemical bonds, hydrogen bonding, or Van der Waals forces inside the lattice. The earlier loss of mass may be due to the loss of absorbed water, which is easier to remove from the PBA. The second phase change is at the temperature around 360 ℃, which is well corresponding to the TGA curve as well. At the temperature above 500, there is steep decrease of both PB-0M and PB-1M, indicating the instability of these two samples.

FTIR was carried out to further understand the water content in the PBA materials with different Na content. Figure 4.2 (a) shows the transmittance for wavenumber from 4000 cm^{-1} to 1000 cm^{-1}. The four samples demonstrate similar transmittance curves in most range, while some intensity peaks of different transmittance have also been observed at the wavenumber near 1415 cm^{-1}, 1610 cm^{-1}, 2055 cm^{-1}. Figure 4.2 (b) and (c) show the details of the three peaks. The transmittance has an obvious decrease of intensity at the peak of 2055 cm^{-1}, which is corresponding to the $\nu(Fe^{II}\text{-}C\equiv N\text{-}Fe^{III})$. The weak peak near 2130 cm^{-1} can be related to the $\nu(Fe^{III}\text{-}C\equiv N\text{-}Fe^{II})$ (Ng, Ding, & Gan, 2001; Yan et al., 2017). On the other hand, the peaks at around 1610 cm^{-1} and 1414 cm^{-1} correspond to the σ(OH) of absorbed water and interstitial water, respectively. Unlike other samples, the peak of 1414 cm^{-1} of PB-4M is almost disappear indicating the decrease of OH^-, which may attribute to the replacement of Na^+ to the water. The addition of NaCl can help to reduce the interstitial water and defects in the crystalline structure. With the increasing content of Na, the peak of 1414 cm^{-1} in PB-4M is weak with low intensity, which implies the low interstitial water of PB-4M.

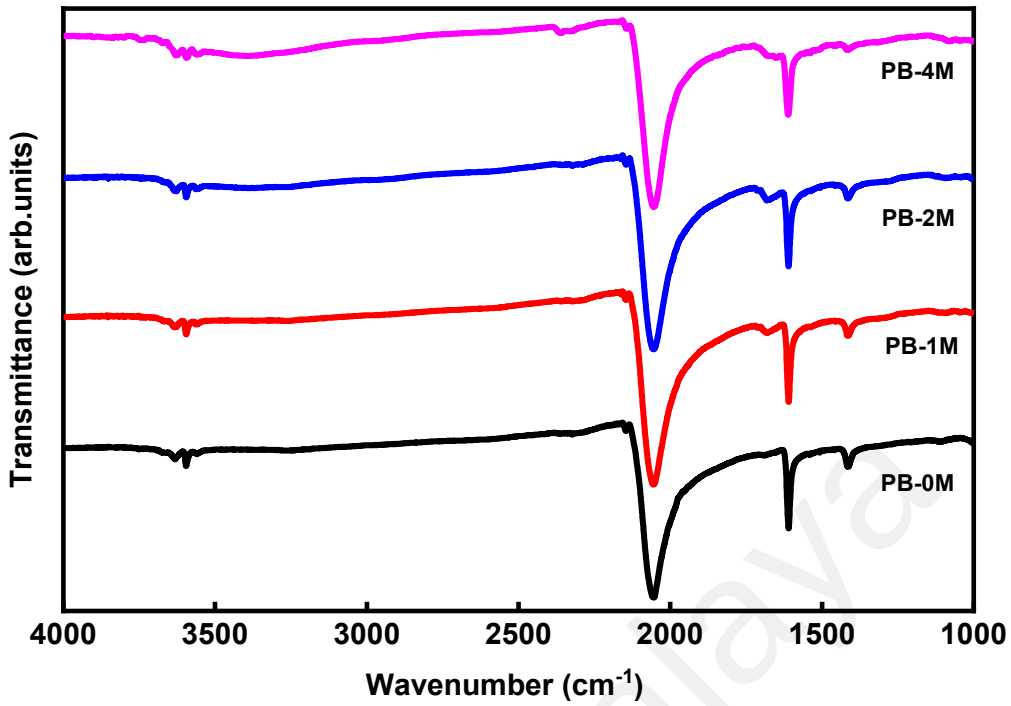

(a)

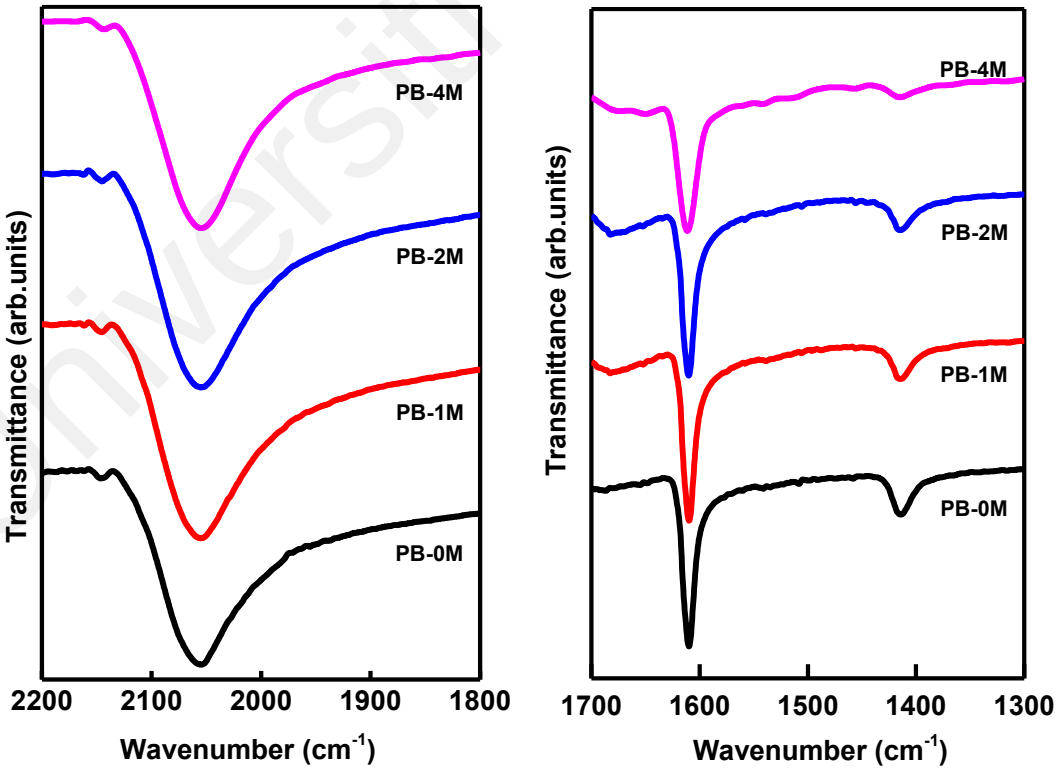

(b) (c)

Figure 4.2: Comparison of FITR at the wavenumber region of (a) 4000 cm^{-1} - 1000 cm^{-1}, (b) 2200 cm^{-1} -1800 cm^{-1} and (c) 1700 cm^{-1} -1300 cm^{-1} of PB-0M, PB-1M, PB-2M, PB-4M

The SEM images of the samples are shown in Figure 4.3. Based on the growth rule of crystal, the concentration of solution may affect the growth and nucleation of crystal and in our case, the morphology of each PBA is change. PB-0 shows a cubid structure with few visible defects (Figure 4.3 (a)). Figure 4.3 (b) shows the morphology of PB-1M and some cracked cubids have been found. For the sample of PB-2M (Figure 4.3 (c)), the morphology has been transformed from cubic structure to multi-rod-like structure. When the concentration of NaCl increases to 4M, the synthesized product turns to nano particles with porous structure. The occupation of Na^+ may decelerate the growth of crystal in the synthesizing process. Therefore, the surface morphology is changed, and the particle size has shrunk from micro-scale to nano-scale when the Na^+ content is increased.

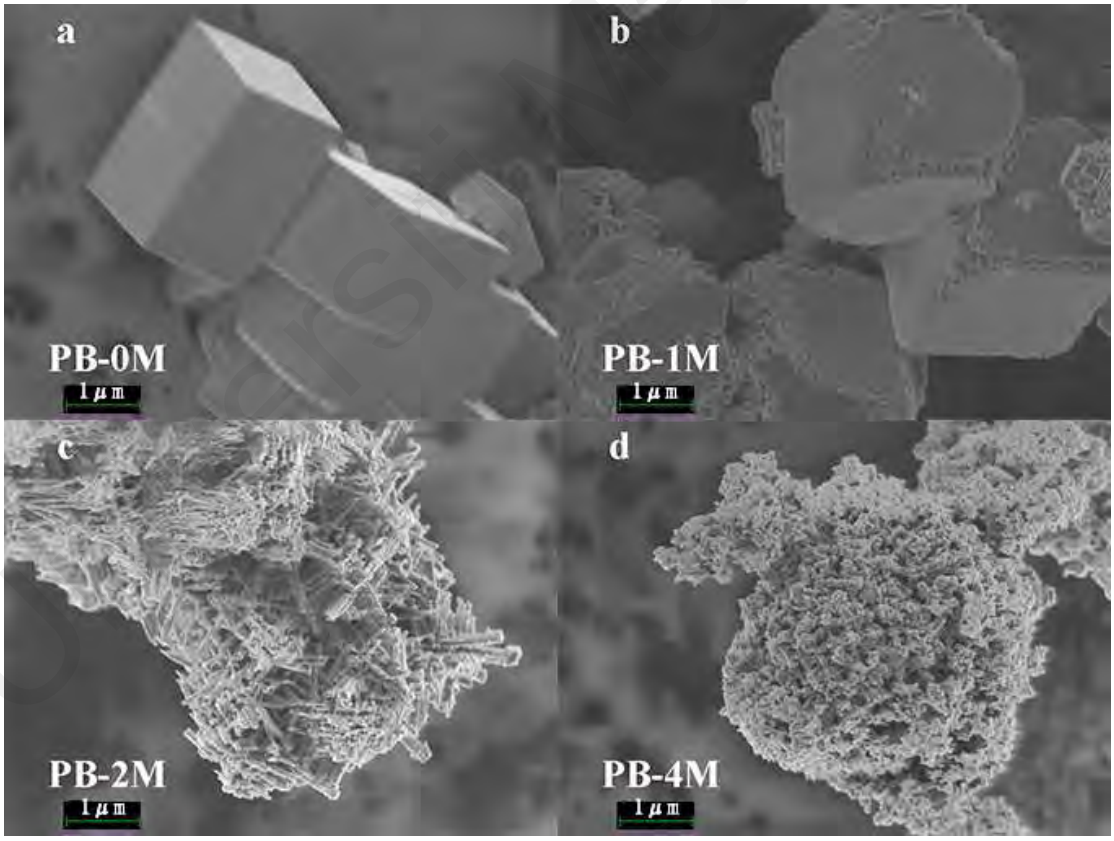

Figure 4.3: The SEM images of (a) PB-0M, (b) PB-1M, (c) PB-2M and d) PB-4M.

To further investigate the surface area of each sample, N_2 adsorption/desorption analyses using BET was carried out. The detailed analysis of the samples is shown in Figure 4.4. All sample displayed type-IV reversible N_2 uptake with obvious hysteresis

loop of PB-0M, PB-1M, PB-2M and PB-4M, indicating that the mesoporous structures in these samples. The surface areas are measured as 2.07 m^2/g, 2.64 m^2/g, 5.83 m^2/g and 28.38 m^2/g for PB-0M, PB-1M, PB-2M and PB-4M, respectively. It is well known that a large surface area of the material could improve the performance in the respect of electrochemical reaction. The large surface area of PB-4M might lead to large contact area between electrode and electrolyte which could improve the electrochemical performance. This porous structure and large specific surface area can also improve the infiltration of electrolyte and fasten the transportation of Na^+. To better understand the structural change of PBA samples, HRTEM was also carried out and the results are shown in Figure 4.5. PB-0M, PB-1M, PB-2M and PB-4M show the morphology of cubic structure, cracked cubic structure without corner, multi-acicular-like structure and the aggregation of nano-particles, respectively. The HRTEM results indicate that the growth of PBA is suppressed in some orientation due to the increased concentration of Na^+, which agrees well with classical nucleation theory and previous works (You et al., 2015; Zakaria & Chikyow, 2017).

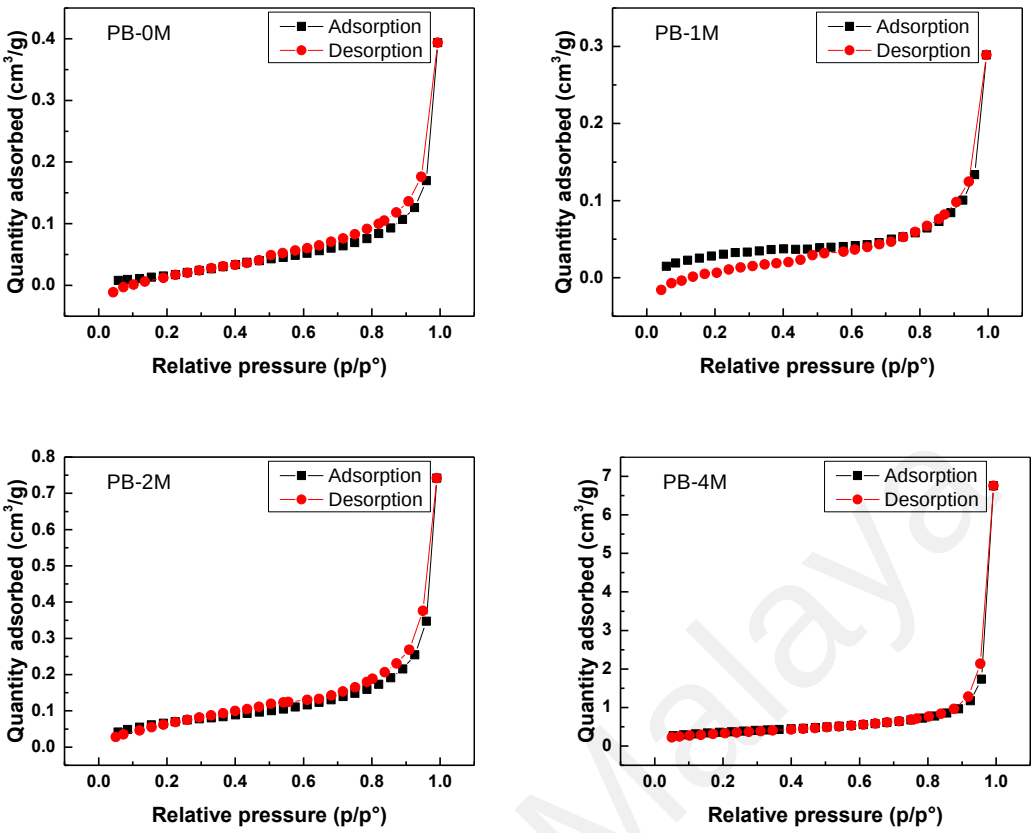

Figure 4.4: N_2 adsorption/desorption isotherms of a) PB-0M, b) PB-1M, c) PB-2M and d) PB-4M.

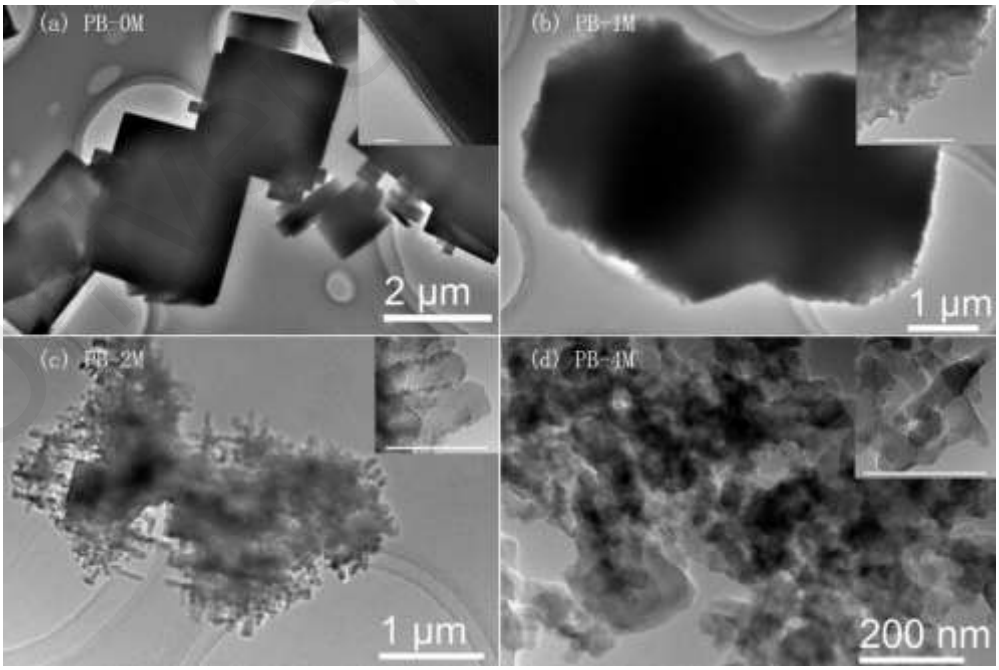

Figure 4.5: The TEM images of (a) PB-0M, (b) PB-1M, (c) PB-2M and (d) PB-4M with high resolution images in the top-right corner (The scale bar in all HRTEM images is 200 nm.).

EDX and powder XRD patterns of the 4 PBA samples were carried out to investigate the difference of morphology and element distribution. Figure 4.6 and Figure 4.7 showed the mapping images and the XRD pattern of the samples. From the EDX results, Na, Fe and N elements are distributed uniformly in the samples. As shown in Figure 4.7, vertical lines represent the peaks of $Fe_4[Fe(CN)_6]_3$ on the standard PDF card (JCPDS No.52-1907). In some status, the peak at around 24° may have the split peaks, but it is clearly seen that all the peaks of the patterns are close to the $Fe_4[Fe(CN)_6]_3$ with face-centered cubic structure (FCC, space group $Fm\bar{3}m$) (Piernas-Muñoz, Castillo-Martínez, Gómez-Cámer, & Rojo, 2016; Wu et al., 2016; C. Zhao et al., 2018). From PB-0M to PB-4M, the peaks move towards left as the structure changes to rhombohedral (space group $R\bar{3}m$) due to the increase of Na content. The lattice parameters of each sample can be calculated by,

$$\alpha = \frac{\lambda}{2\theta\sqrt{h^2 + k^2 + l^2}} \quad \textbf{(4.6)}$$

where α is lattice parameter, θ is diffraction angle, λ is incident wavelength, (h, k, l) is the Miller index. The lattice parameters of PB-0M, PB-1M， PB-2M, PB-4M are calculated as 10.22478 Å, 10.22522 Å, 10.23152 Å, 10.24252 Å, respectively. With the increasing of Na^+ content, the lattice parameter is also increased and the phase of the material structure gradually changes from cubic to rhombohedral (Wu et al., 2016). This phase transition is probably due to the insertion of Na^+ ions which occupies the center channel and causes the lattice to shrink.

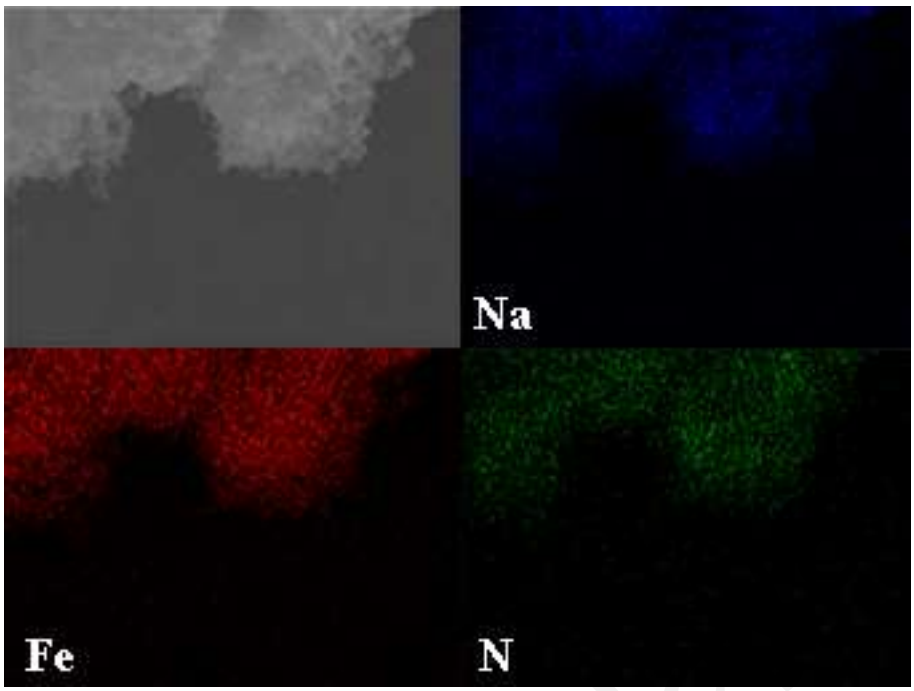

Figure 4.6: EDX mapping of PB-4M (Na, Fe and N)

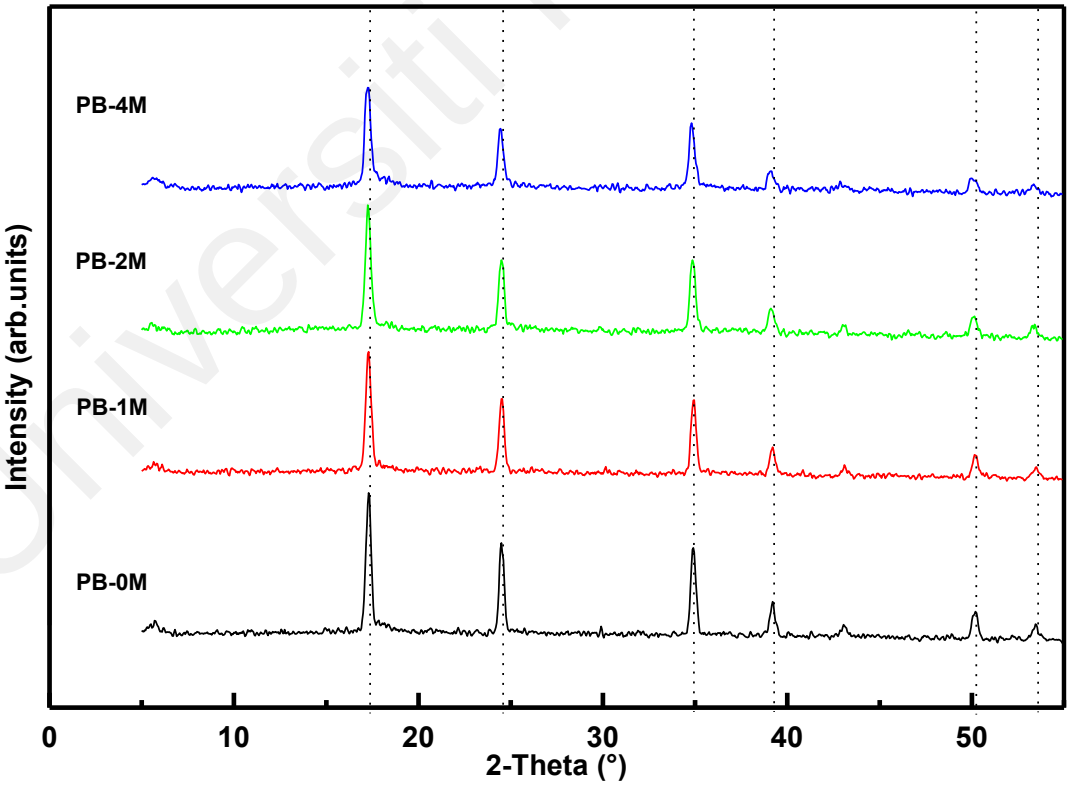

Figure 4.7: Comparison of XRD patterns of PB-0M, PB-1M, PB-2M and PB-4M.

Based on previous studies, PBA is a three-dimension network with the formula as $A_xMM'(CN)_6$ (A = Na, K; M and M′ = Fe, Co, Mn, Ni) (Buser et al., 1977; X. Shen et al., 2009). The most important feature that makes PBA a possible cathode material is the open-framework structure. Here in our PBA structure, M and M′ are both Fe, A is Na, thus the formula can be written as $Na_xFeFe(CN)_6$. Fe(II) and Fe(III) are bridged by the linear (C≡N) group. The C≡N bond opens the faces of the elementary cubes, which facilitates the transportation of Na^+ in the body-center structure. Due to this unique property, the Na^+ ion could move fast and stably, which makes PBA a promising cathode material for SIB (Y. Lu et al., 2012; Qian et al., 2018). Calculating by the ICP-MS and CHN elements analysis result, the composition of each sample was listed in Table 4.1. ICP-MS is used to determine the Na and Fe contents while elemental analysis is used to determine C, H, N element. The concentration ratio is divided by atomic weight of each element to obtain the mole ratio. The prepared PB is written according to $Na_xFeFe(CN)_6 \cdot nH_2O$. Then, the mole ratio of PB is simplified by normalising Fe mole ratio to 1. It is noticed that the ratio is increased with an increase of Na^+ content during the process.

Table 4.1: The element (atom) ratio of PB-0M, PB-1M, PB-2M, PB-4M,

	PB-0M	PB-1M	PB-2M	PB-4M
Formula	$Na_{1.20}FeFe(CN)_6 \cdot 2.42H_2O$	$Na_{1.54}FeFe(CN)_6 \cdot 2.11H_2O$	$Na_{1.58}FeFe(CN)_6 \cdot 1.89H_2O$	$Na_{1.63}FeFe(CN)_6 \cdot 1.75H_2O$

With an increase of Na^+ content, the morphology of PBA can be changed as shown in Figure 4.8: The insertion of Na+ inside Prussian blue. PBA without Na^+ is composed of cubic phase; while the initial cubic phase will gradually change to the rhombohedral phase

with the increase of Na^+ content (You et al., 2015). From the SEM and TEM images, the morphology of PBA has successively transformed to nanoparticle structure and the size of particle has also decreased, which is probably due to the increasing content of Na^+ ions in the solution. As we know, varying experimental conditions may cause the change of morphology. For instance, Shen and the co-worker had studied the different synthesizing environments such as the adding of surfactant and reductant (X. Shen et al., 2009). In this study, however, the only varying factor is the concentration of Na^+ during the synthesizing procedure; therefore, we believe that the morphological change is caused by the increased content of Na^+ (L. Li, Nie, Chen, & Wang, 2019). A hypothetical formation process is shown in Figure 4.9. With the addition of Na^+ ions in the solution, the Na^+ ions would either occupy the vacancies or the tunnel of PB. These Na^+ ions could retard the growth of PBA by cutting the connection or force between $Fe(CN)_6^{4-}$. This might be the reason for the irregular morphology of PB-1M. With an increased NaCl concentration of 2M, the growth of PBA is suspended in certain orientations; therefore, PBA became multi-rod-like structure. In a nearly saturated NaCl solution for PB-4M, this suspension becomes more severe in all directions and only nano-sized particles can be synthesized.

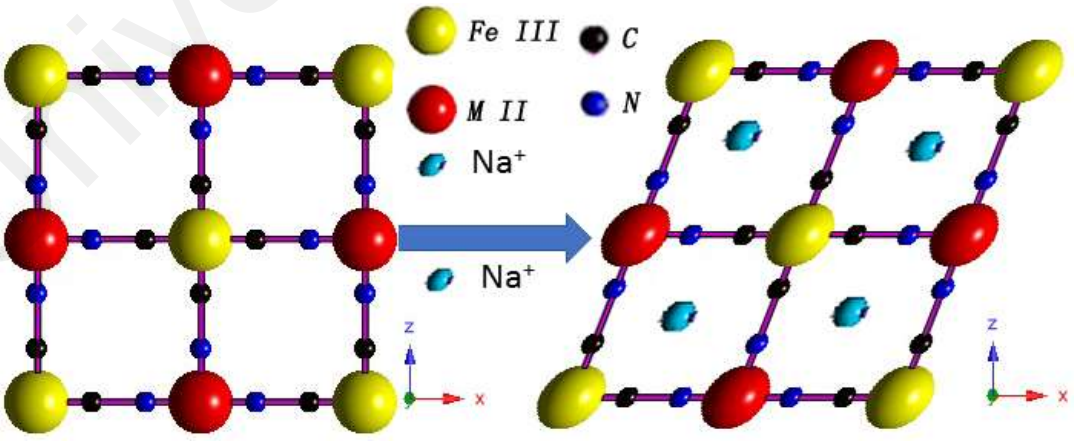

Figure 4.8: The insertion of Na^+ inside Prussian blue

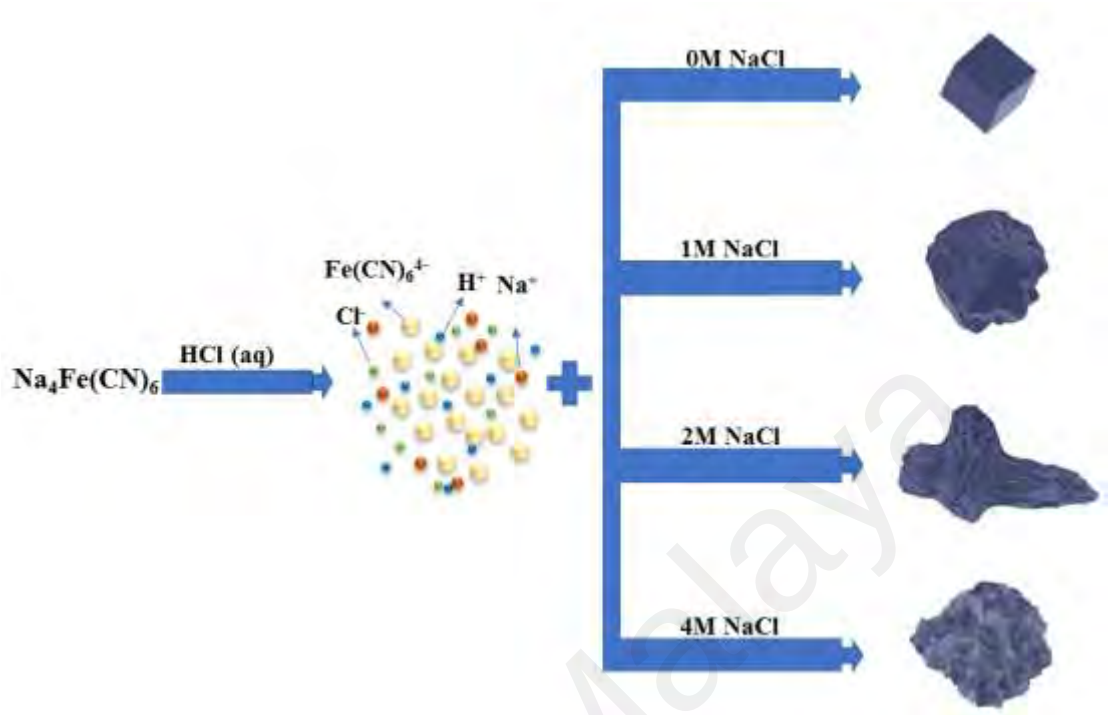

Figure 4.9: The formation of PBA with different Na^+ ions ratio.

4.3 Electrochemical Characterizations of Na-rich PBA

To investigate the effects of Na^+ ions content of PBA in a high temperature, some electrochemical properties were carried out at different temperatures with different current densities, and the voltage ranges from 2.0 V to 4.0 V. Figure 4.10 shows the galvanostatic charge/discharge voltage profiles at a 0.2 C at RT for PB-0M, PB-1M, PB-2M and PB-4M. During the first cycle of charging, PB-4M exhibits an initial specific capacity of 105 mAh/g while the capacities of PB-0M, PB-1M, PB-2M are 57 mAh/g, 80 mAh/g, 84 mAh/g, respectively. The discharged capacity during the first cycle are 109 mAh/g (PB-0M), 115 mAh/g (PB-1M), 120 mAh/g (PB-2M) and 130 mAh/g (PB-4M), which are similar to the value reported previously (You et al., 2014).Obviously, higher Na^+ content also leads to a high initial coulombic efficiency (52.3 %, 69.5 %, 70.0 %, 83.8 % for PB-0M, PB-1M, PB-2M and PB-4M, respectively.) which means that there are more active sites. The higher initial capacity of PB-4M can be ascribed to the high

Na^+ content and the nanocrystallization of the material. The nanoscale size of PB-4M leads to better infiltration of electrolyte and shortens the path of Na^+ movement, which might also affect the thermal feature of PB.

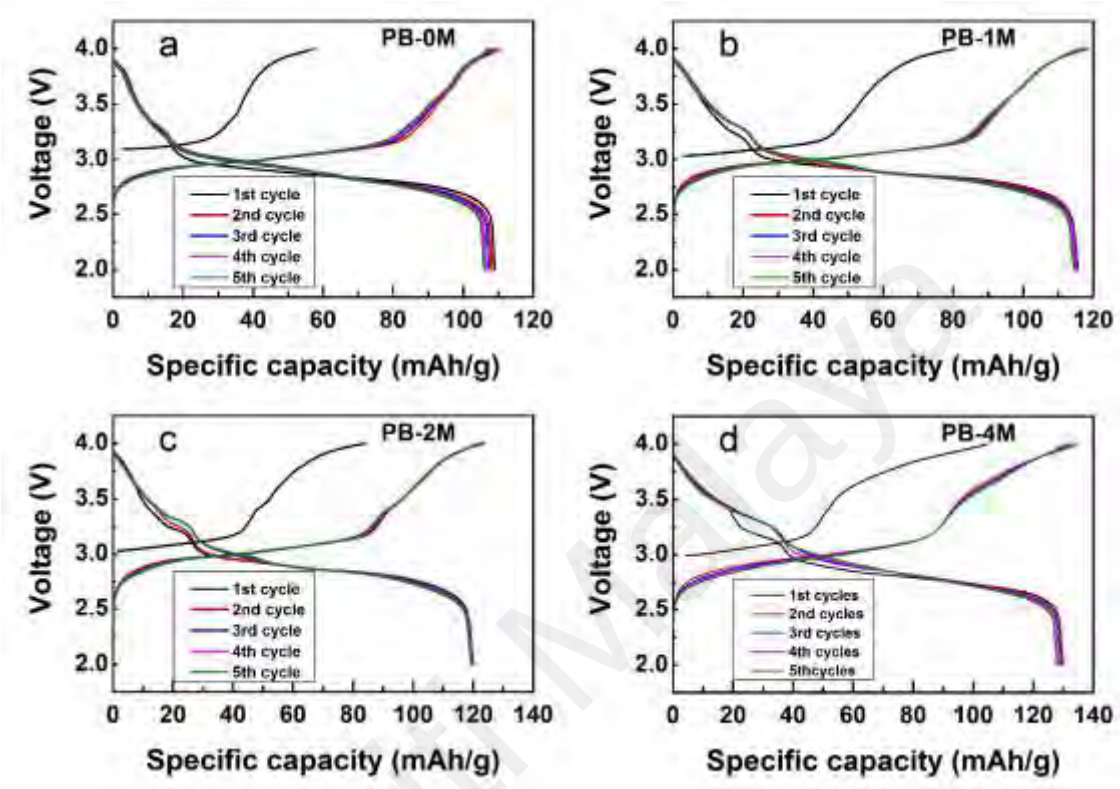

Figure 4.10: charge-discharge profile of (a) PB-0M, (b) PB-1M, (c) PB-2M and (d) PB-4M between 2.0 V and 4.0V at 0.2 C at RT

Figure 4.11 (a-d) show the rate performance profiles of the four samples in different current densities at RT. When the current density is increased, PB-0M shows the lowest discharge capacity which are 100 mAh/g, 91 mAh/g, 80 mAh/g, 62 mAh/g at 0.5 C, 1 C, 2 C, 5C, respectively. PB-1M and PB-2M show the better discharge capacity performances. The discharge capacities of PB-1M are 109, 103, 95, 85 at 0.5 C, 1 C, 2 C, 5C, respectively; while those of PB-2M are 115, 107, 100, 90 at 0.5 C, 1 C, 2 C, 5C, respectively. Among all the samples, PB-4M has shown the best performance with highest discharge capacities of 123 mAh/g, 120 mAh/g, 114 mAh g g^{-1}, 110 mAh/g at 0.5

C, 1 C, 2 C, 5C, respectively. However, PB-0M suffers a significant drop of specific capacity due to the increasing rate of 5 C.

To investigate the influence of operating temperature, the cells were tested at the increased temperatures of 40 ℃, 60 ℃ and 80 ℃ successively. As shown in Figure 4.11 (e), there are significant drops of discharge capacity at the high rate and the high temperatures (40 ℃, 60 ℃) for PB-0M. When the test temperature increases to 80 ℃, all the samples except PB-4M become unstable. After a few charge/discharge cycles at 80 ℃, the specific capacity of PB-0M deteriorates to almost 0. PB-2M and PB-1M also exhibit declined specific capacity at 5 C. It should be noted that PB-4M shows a little turbulence of capacity in the first 10 cycles at 80 ℃, but the reversible capacity stabilizes to more than 100 mAh at 1 C (120 mAh/g), 2 C (112 mAh/g), 5 C (103 mAh/g) shortly afterwards. This abnormal phenomenon could not be described well based on our knowledge, we guess that it might due to the reaction between electrolyte and water at the temperature of 80 ℃. We assume that since PB-4M has the highest Na^+ ions content inside the crystal structure, the interstitial water decreases significantly from the previous analysis, which makes the framework of structure stable at high temperature (Song et al., 2015). Consequently, PB-4M exhibits the highest and most stable performance in the high current density and at high operating temperature.

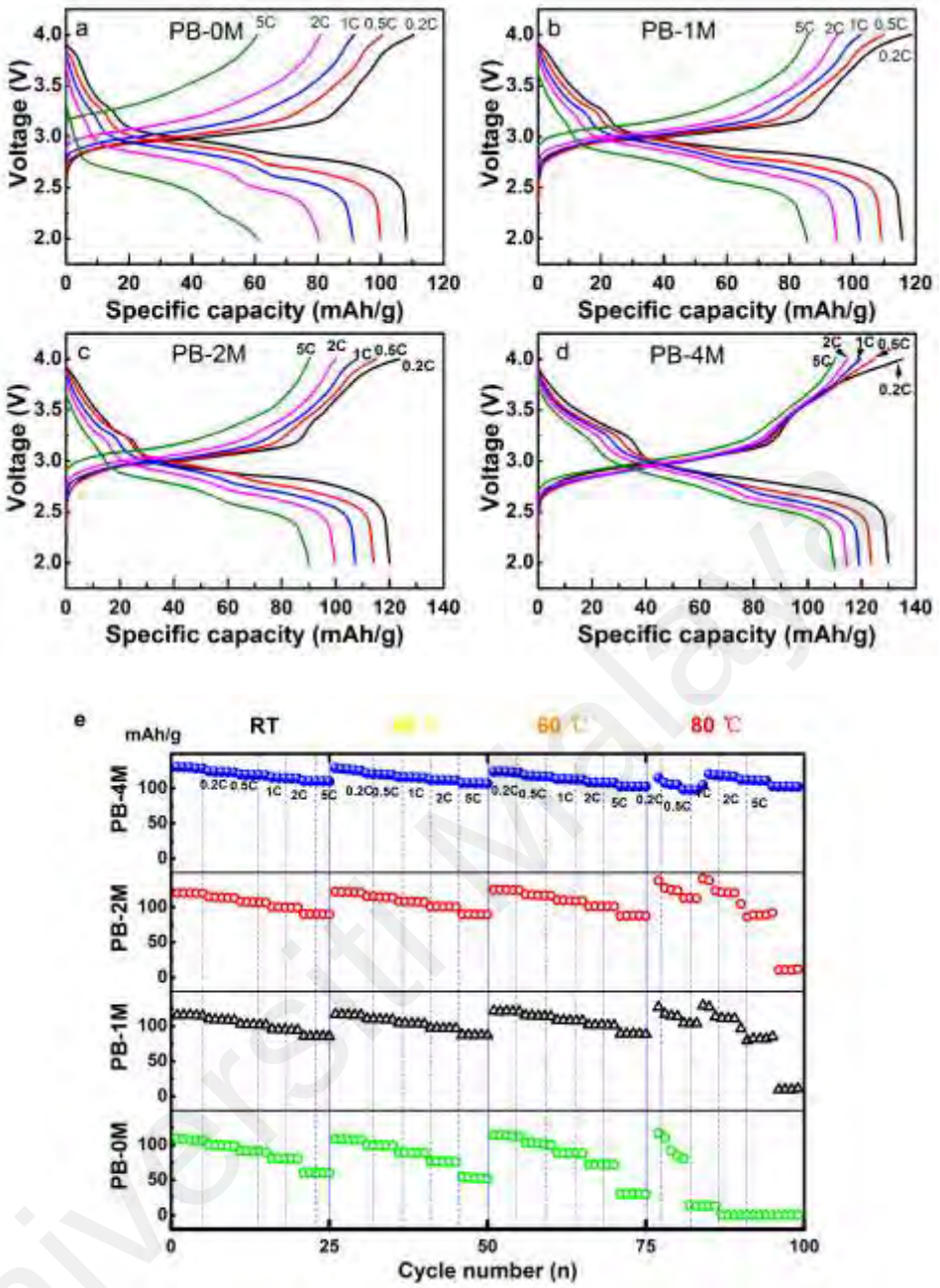

Figure 4.11: The rate performance profiles of a) PB-0M, b) PB-1M, c) PB-2M, d) PB-4M and e) the rate performance of PB-0M, PB-1M, PB-2M, PB-4M at different current densities.

The long cycling performance of the materials should also be tested for application. The previous results for PB-0M and PB-1M show that they cannot be applied for practical usage due to the quick decay of capacity at high operating temperature or at high rate. For comparison, PB-4M and PB-2M have been tested for the long cycling performance at 80 ℃ for 500 cycles (Figure 4.12). PB-4M shows a high specific discharge capacity of 108

mAh/g and remains a reversible specific discharge capacity of 58 mAh/g after 500 cycles with an excellent efficiency of almost 100%. Comparing with PB-4M, PB-2M shows worse performance regarding to the discharge capacity. The initial specific capacity is 98 mAh/g while the final specific discharge capacity is only 30 mAh/g with a disorder of efficiency. The remarkable performance of PB-4M can be attributed to the high content of Na^+. The high-water content is the main barrier for the commercialization of PBA as the cathode material. The water may cause side reaction with electrolyte which might lead to the collapse of PBA structure during the charge-discharge process. The high concentration of Na^+ in the solution during synthesis can help to form a low content of interstitial water, which would enhance the thermal reliability of the PBA cathode.

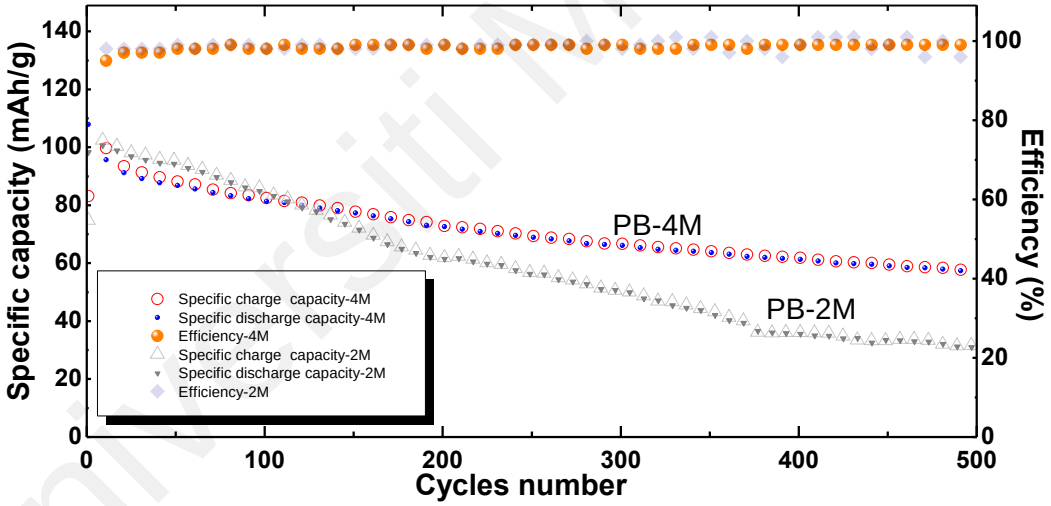

Figure 4.12: Cycling performance of PB-2M and PB-4M at 80 ℃.

4.4 Summary

- Na-rich PBA has been prepared with high thermal stability.
- The high concentration of Na^+ in the PBA framework could decrease the amount of vacancies and the content of the interstitial water.

- The Na^+ facilitate the nanocrystallization of the PBA structure, which shortens the path of Na^+ transportation. Therefore, excellent charge/discharge performance at high temperature and high current has been achieved for PB-4M.
- PB-4M exhibits an excellent performance, which delivers a specific discharge capacity of 130 mAh/g and remains a reversible specific capacity of 58 mAh/g after 500 cycles at 80 °C with an efficiency of near 100%. The good thermal stability should be attributed to the lower water content and fewer vacancies.

CHAPTER 5: CAGE-LIKE POROUS PRUSSIAN BLUE ANALOGUE AS CATHODE MATERIALS FOR SODIUM-ION BATTERIES[2]

5.1 Introduction

In previous chapter, we managed to produce Na-rich PBA with good thermal stability that exhibited specific capacity of 57 mAh g^{-1} after 500 cycles at an elevated temperature of 80 °C (Y. Chen et al., 2019). Compared to other previous outstanding works (Q. Liu et al., 2020; Qian et al., 2018; B. Wang et al., 2018; W. Wang et al., 2020; D. Yang et al., 2015; A. Zhou et al., 2020), this chapter uses a facile re-heating and acid-etching method to obtain the nano porous cage-like PBA that shows high electrochemical performance.

5.2 Structural And Morphological Characterizations of Cage-Like PBA

Figure 5.1 shows the morphology images of PBAs before and after etching process. As presented in Figure 5.1(a), PB-A precursor displays a broad size distribution of cubic structure with the size ranging between 200 – 500 nm and aggregated together. Figure 5.1 (b) shows PB-C precursor with uniform size of cubic particles (with diameter of ~400 nm) as a result of the re-heating process during synthesis (L. Han, Yu, & Lou, 2016) . Every PBA cube (both PB-A precursor and PB-C precursor) are assembled by many PBA nanocrystals in an oriented arrangement (M. Hu et al., 2012). The re-heating process simply enables the re-assembly of PBA nanocrystals to form more uniform PBA cubes. On the other hand, PVP coats on the surface of PBA cubes also play an important role to prevent the continuous growth of PBA mesocrystal.

[2] **Chapter 5 of this thesis is published as:** Chen, Y., Woo, H. J., Syed Mohd Fadzil, S. A. F., Tan, W., Wang, F., & Mohd Arof, A. K. (2022). Cage-Like Porous Prussian Blue as High-Capacity Cathode for Sodium-Ion Batteries. *ACS Applied Nano Materials, 5*(4), 4833-4840. doi:https://doi.org/10.1021/acsanm.1c04416

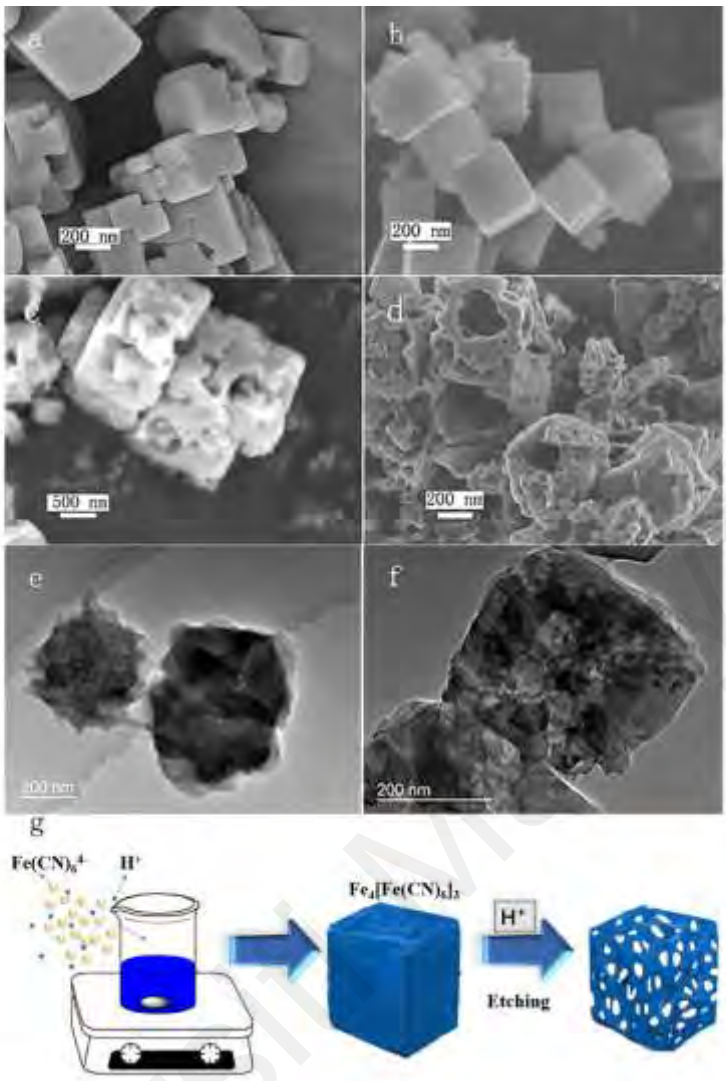

Figure 5.1: FESEM images of (a) PB-A precursor, (b) PB-C precursor, (c) PB-A and (d) PB-C. TEM images of (e) PB-A and (f) PB-C and (g) schematic illustration of PB-C synthesis process.

Upon etching reaction, PB-A precursor turned into irregular porous crystals while PB-C precursor became a cage-like porous cubes with internal hollow cavity, as shown in Figure 5.1 (c) & (d), respectively. The PBA cubes sizes were not significantly changed and the original smooth surface became rough. Figure 5.1 (e) and (f) represents TEM images of PB-C and PB-A respectively. The etching agents (HCl molecules) diffused into the internal part of PBA cubes through the vacancies/defects. At the same time, the PVP coat on the PBA cube surface protected the shell by reducing the etching rate. Therefore,

the etching rate in the center of PBA cube has relatively higher etching rate, forming an internal hollow cavity (Cölfen & Mann, 2003; M. Hu et al., 2012; M. Hu, Jiang, Lin, & Zeng, 2010). Besides, some structure of the PBA cubes may also be etched randomly during the etching process, creating the cage-like porous structure.

Figure 5.1 (g) shows a schematic of the two steps PB-C synthesis processes. In the first step of synthesis, $Na_4Fe(CN)_6$ was used in a weak acid environment to produce PB-C precursor. In the second step, the precursor was put in a strong acid condition to optimize the etching process to form PB-C. The use of PVP is very important in which it acted as the surfactant to protect the structural integrity and to avoid the collapse of PBA structure (X. Shen et al., 2009).

The XRD patterns of PB-C, PB-A and the standard PBA (JCPDS No. 52-1907) are shown in Figure 5.2 (a)**.** The peaks approximately at 2θ = 17.5° , 24.7° , 35.2° , 39.5 ° , 43.5° , 50.5° and 53.8° have been assigned to the crystal planes (200), (220), (400), (420), (422), (440), and (600), respectively. Compared to the standard pattern, no obvious change is indicated in both PB-A and PB-C XRD spectrum showing the purity and structure stability of PB-C and PB-A. In addition, sharp and strong peaks have demonstrated the high crystallinity of PB-C and PB-A.

TGA curve of both PB-C and PB-A are depicted in Figure 5.2 (b) at the temperature between 50 °C and 600 °C. For PB-A, the weight loss of ~20% in the range of 50 °C to 300 °C could be attributed to the loss of water. The first turning point of the curve can be seen at ~300 °C attributing to the structural decomposition of PB-A. The loss of water of PB-C is only ~10 % in which can be observed from 50°C to 330 °C. The different percentage of water content can be explained by their different structure. The dense structure of PB-A precursor would hinder the diffusion of H^+ (etching agent) thus make it hard for interstitial water to be removed. On the other hand, the loose structure PB-C

precursor have provided the random path needed for the H^+ to diffuse into the PBA cube causing the interstitial water to be etched easily and produced PB-C with less water content (M. Hu et al., 2012).

To further study the change of morphology, the N_2 adsorption/desorption isotherms of PB-C and PB-A were carried out, as presented in Figure 5.2 (c) and (d), respectively. The inset showed the pore size distribution of each sample via BJH model. The BET specific surface area of PB-A and PB-C are determined as 6.6 m^2g^{-1} and 79.3 m^2g^{-1}, respectively. PB-C has exhibited a significantly larger surface area than PB-A due to its cage-like porous structure. This would mean a larger contact area between the active material and the electrolyte, thus increases the potential active sites for the redox reaction to occur during the charge-discharge process. Furthermore, PB-A shows almost no pore distribution while PB-C depicts some pores size of about 5 – 10 nm, which were observed in FESEM images.

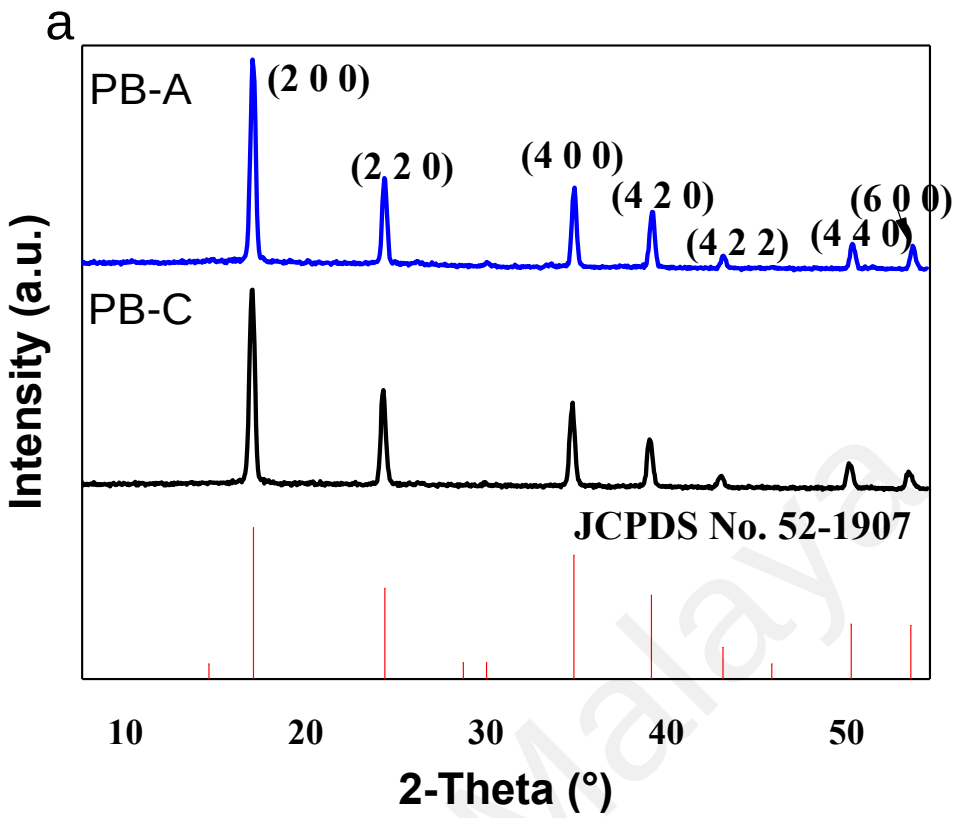

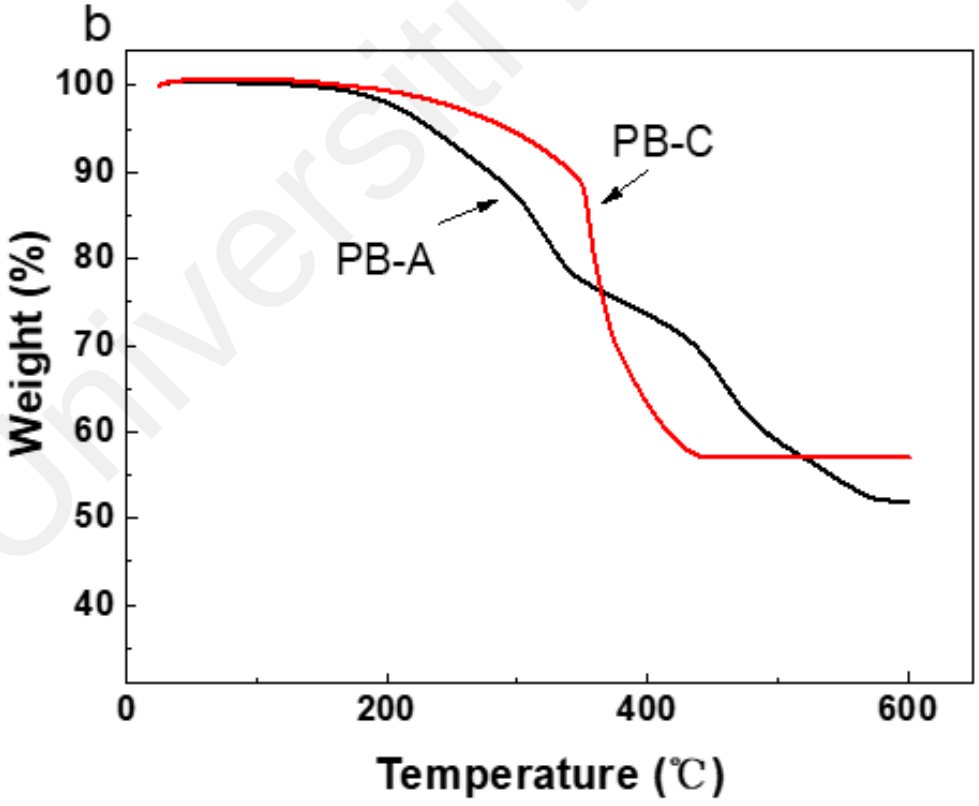

Figure 5.1, continue.

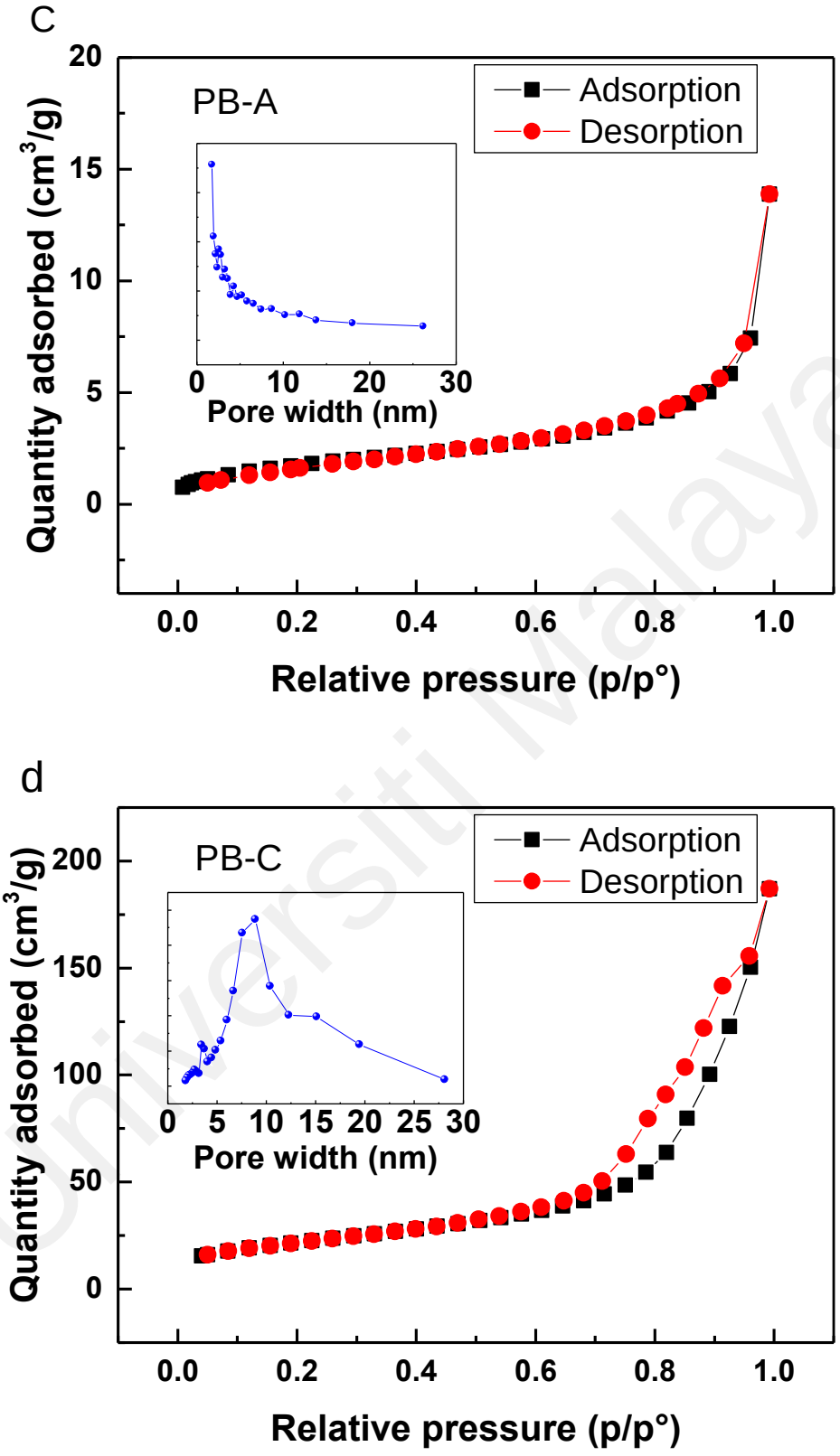

Figure 5.2: (a) XRD patterns of PB-A and PB-C, (b) TGA curves of PB-A and PB-C, N_2 adsorption/desorption isotherms of (c) PB-A and (d) PB-C.

5.3 Electrochemical Characterizations of Cage-like PBA

To study the advantages of cage-like porous structure, batteries performances were carried out. Figure 5.3 (a) and Figure 5.3 (b) represent the charge-discharge performance of PB-C and PB-A at voltage between 2.0 – 4.0 V with different C-rate (0.2 C – 10 C). Both PB-C and PB-A have a similar charge-discharge pattern at the voltage between 2.5 V – 3.0 V. At low C-rate (0.2 C), PB-A delivers a discharge capacity of 95 mAh/g. However, the discharge capacity decreases rapidly to 92 mAh/g, 89 mAh/g, 84 mAh/g, 74 mAh/g and 55 mAh/g with increasing current density to 0.5 C, 1 C, 2 C, 5 C and 10 C, respectively. In contrast, PB-C gives a high discharge capacity of 112 mAh/g at 0.2 C and able to maintain quite well (with no significant drop) at 109 mAh/g, 105 mAh/g, 102 mAh/g, 99 mAh/g and 97 mAh/g with increasing current density to 0.5 C, 1 C, 2 C, 5 C and 10 C, respectively. Figure 5.3 (c) and Figure 5.3 (d) compare the rate performance of PB-C and PB-A. PB-A could only deliver less than 60% retention (0.2 C to 10 C) while PB-C shows a satisfactory rate performance with 83 % retention. The ability of PB-C to perform at high current density is very much due the high number of exposed active sites and short migration distance of Na^+, leading to enhance ions diffusion rate and electron transfer dynamics (Jiang et al., 2021). Figure 5.3 (e) shows the long cycling performance. PB-A exposes its problem as it suffers with low-capacity retention of 70 % after 1000 cycles at 1 C. On the contrary, PB-C shows a capacity retention of more than 85 % after 1000 cycles. It must be noted that almost no capacity fading is observed from 50^{th} to 1000^{th} cycle, indicating the high stability of PB-C for long cycling.

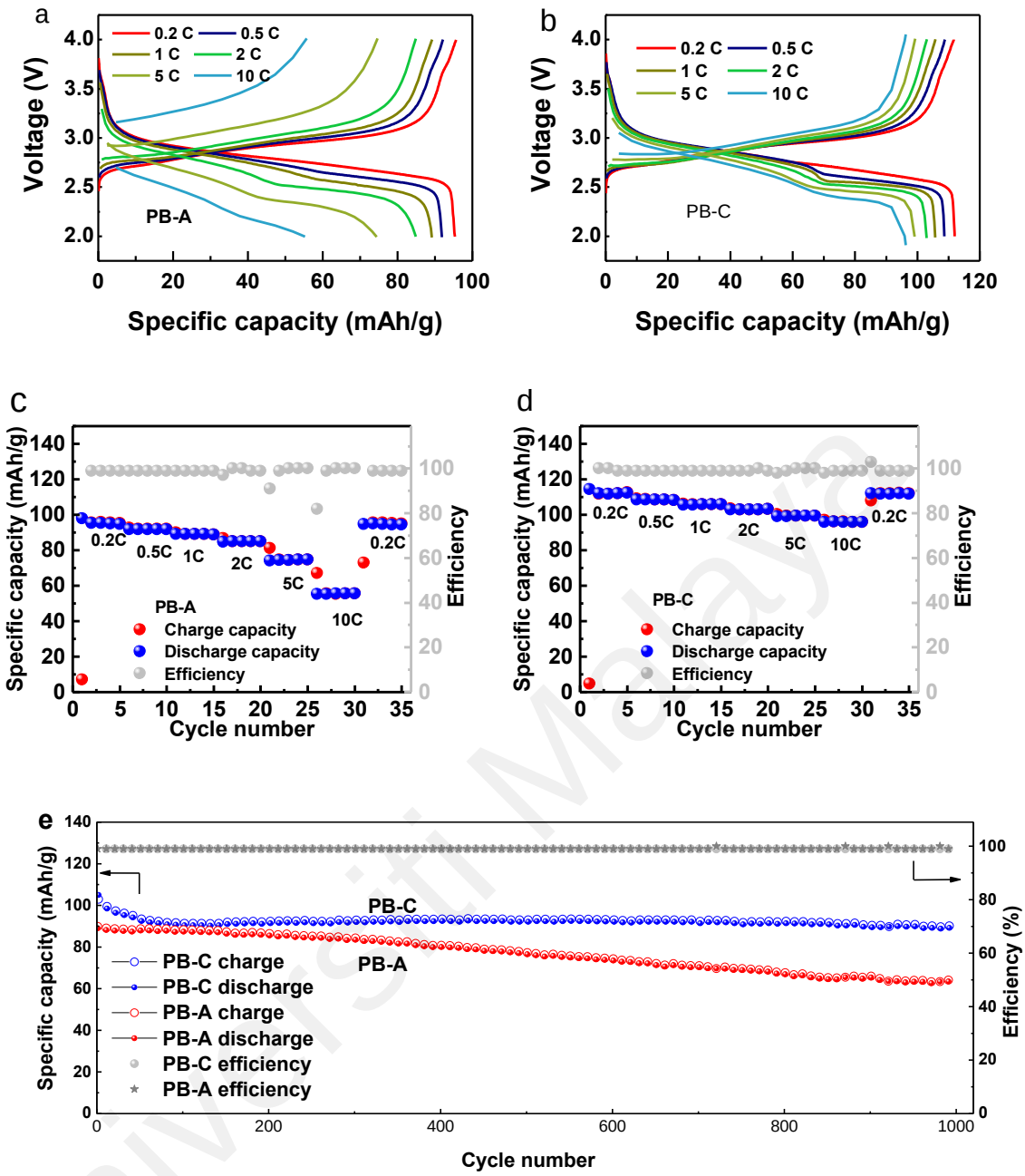

Figure 5.3: The electrochemical performance of PB-A and PB-C: (a) and (b) charge/discharge profile at different current, (c) and (d) rate capability, (e) 1000 charge/discharge cycling at 1 C.

XPS spectroscopy has been conducted for PB-A and PB-C. As shown in Figure 5.4 (a) and (b), the presence of element O, Fe, N and C in PB-C were confirmed by XPS spectra. From Figure 5.5, it is noted that the amount of O element that represents H_2O in PB-A is two times higher than that of PB-C, in which consistent with the TGA results. Moreover, the percentage of O element decreases while the percentage of N element (represent C≡N bond) increases from PB-A to PB-C, indicating that the crystal structure of PB-C is

more occupied by $Fe(CN)_6$ instead of H_2O. Figure 5.4 (b) shows the XPS spectra for Fe element of PB-C. PB-C has a major Fe divalent and there are four fitted peaks, corresponding to 708.6 eV of Fe(II) 2P 3/2, 713.0 eV of Fe(III) 2P 3/2, 721.5 eV of Fe(II) 2P 1/2 and 725.9 eV of Fe(III) 2P 1/2. The electrochemical active Fe^{2+} provides more active sites for the redox reaction to take place, increasing the electrochemical performance of PB-C.

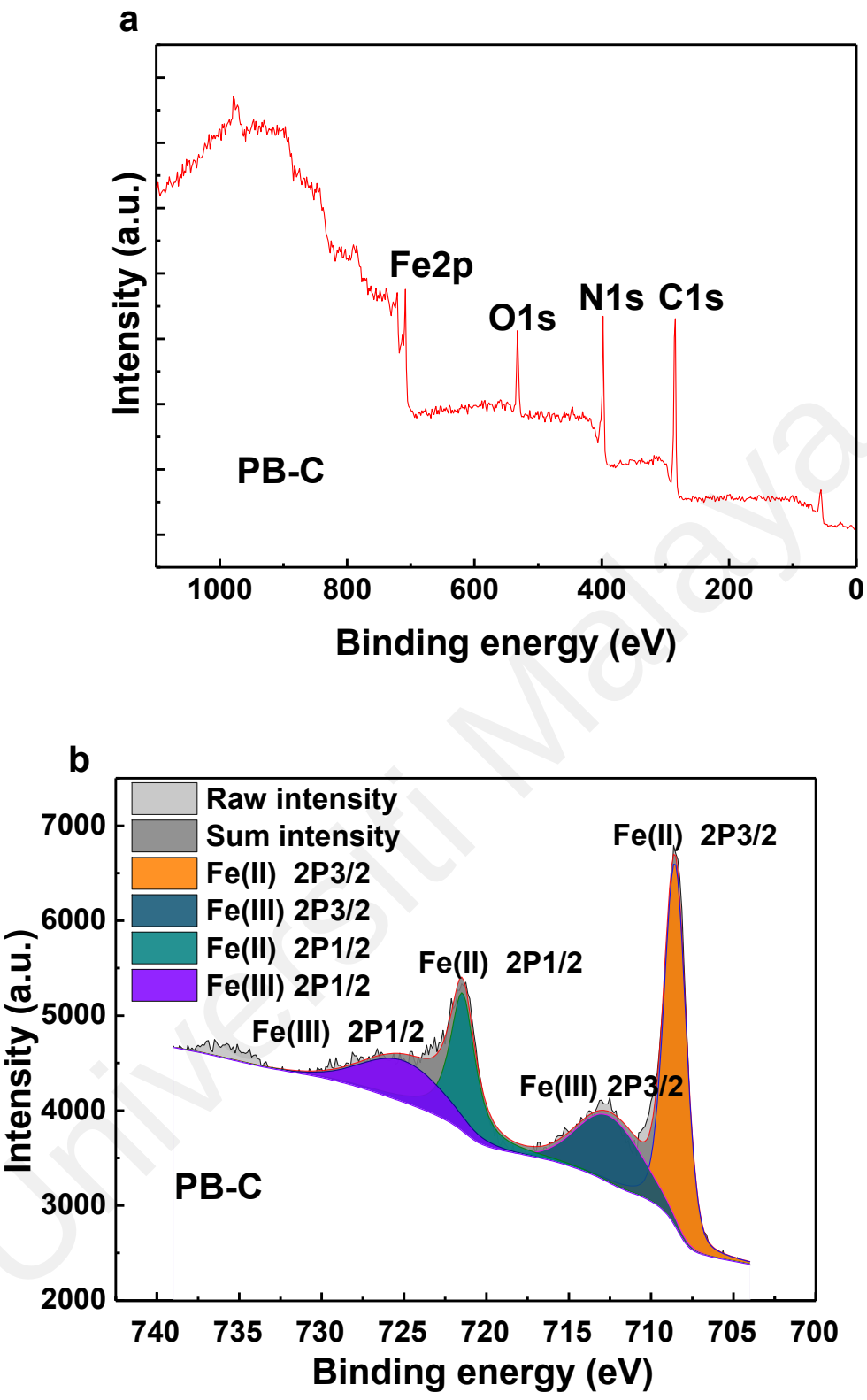

Figure 5.4: (a)XPS spectra of PB-C and (b) High-resolution XPS spectra of PB-C.

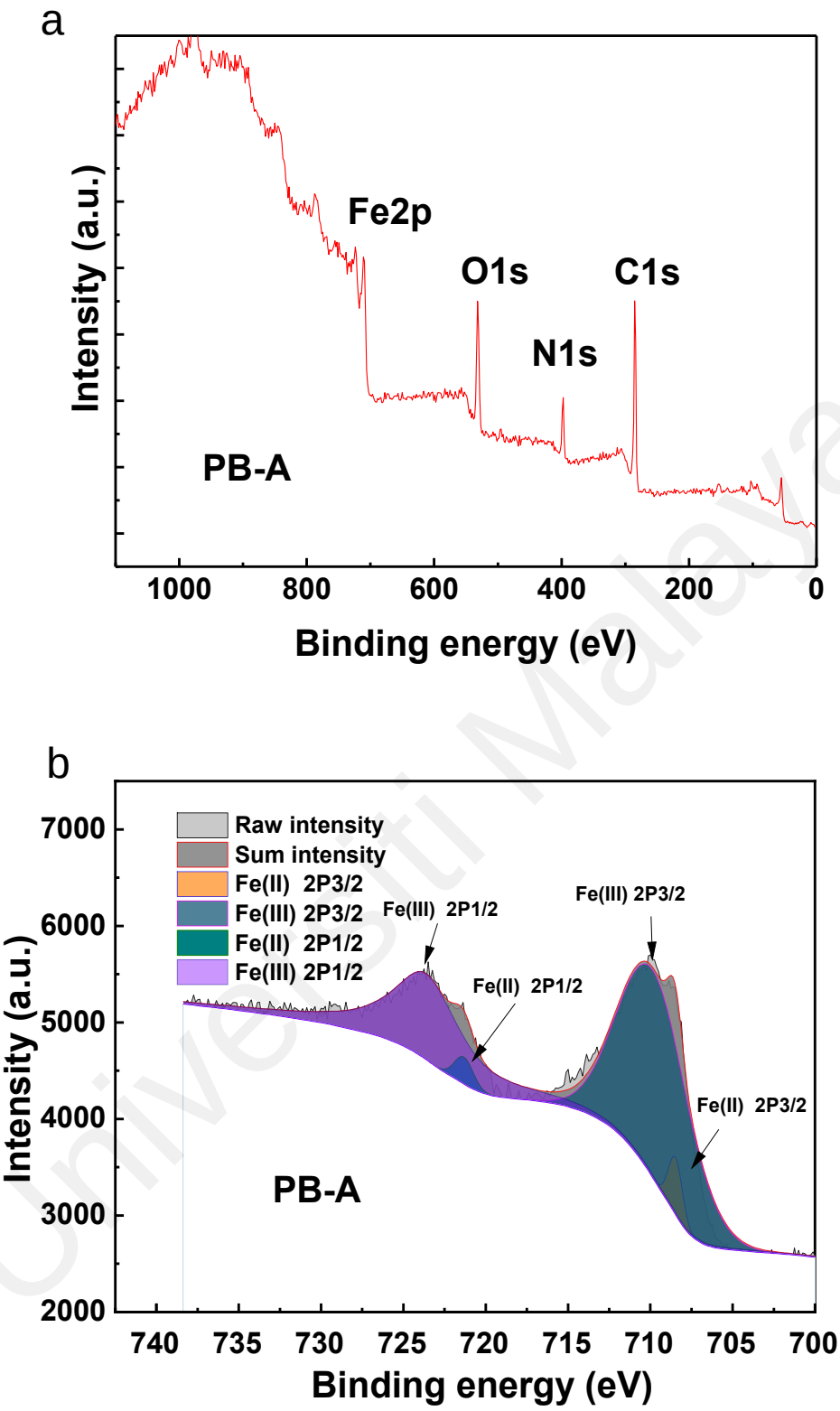

Figure 5.5: (a)XPS spectra of PB-A and (b) High-resolution XPS spectra of PB-A.

The kinetics of Na^+ transfer during the charge/discharge process was determined by the electrochemical impedance spectra (EIS) before and after 100 cycles, in the frequency range of 0.1 Hz - 100 kHz. The fitted Nyquist plots are depicted in **Figure 5.6** (a). From the plot, there are two semicircles and an incline line for both samples before cycling, corresponding to the resistance of solid electrolyte interface film (R_{sei}), charge transfer resistance (R_{ct}) and the ions diffusion in the bulk, respectively. After 100 cycles, two semicircles of both samples are observed to merge into one semicircle indicating the activation of the battery. In addition, the semicircle that represents R_{ct} of PB-C is much smaller than PB-A, representing that the charge transfer of PB-C is faster than PB-A. To further understand the ionic transfer inside the bulk, the ions diffusion coefficient is calculated at the low-frequency region with the following equations:

$$\boldsymbol{D = \frac{R^2T^2}{2A^2n^4F^4C^2\sigma^2}} \quad \textbf{(5.1)}$$

$$\boldsymbol{Z_{re} = R_s + R_{ct} + \sigma\omega^{-1/2}} \quad \textbf{(5.2)}$$

Where D is diffusion coefficient of Na^+, T is absolute temperature, R is gas constant, n is the amount of electron transfer during the redox process, A is the surface area of the electrode, C is molar concentration of Na^+, F is Faraday constant and σ is Warburg coefficient. R_s is the electrolyte resistance, Z_{re} is real impedance, R_{ct} is charge transfer resistance, ω is angular frequency (S. Li et al., 2014). From equation (1), the diffusion coefficient of Na^+ has a positive value relating to σ. Based on equation (2), Z_{re} and $\omega^{-1/2}$ has a linear relationship depicted in Figure 5.6 (b), in which shows that the σ (the slope) of PB-C is much smaller than PB-A at low frequency. A smaller σ value of PB-C gives a higher diffusion coefficient value, in which correlates to the higher kinetic transfer of Na^+ in the PB-C bulk compared to PB-A. From the EIS results, it can be concluded that the electrochemical reaction impedance could be reduced by modifying

the typical cubic PBA structure to the cage-like porous structure. The mesocrystal and cage-like structure of PB-C gives a large contact area with electrolyte and provides smooth paths for ions to transfer between interfaces. Therefore, it can be inferred that the kinetic of Na^+ diffusion and the charge transfer has been improved by the morphological optimization of PB.

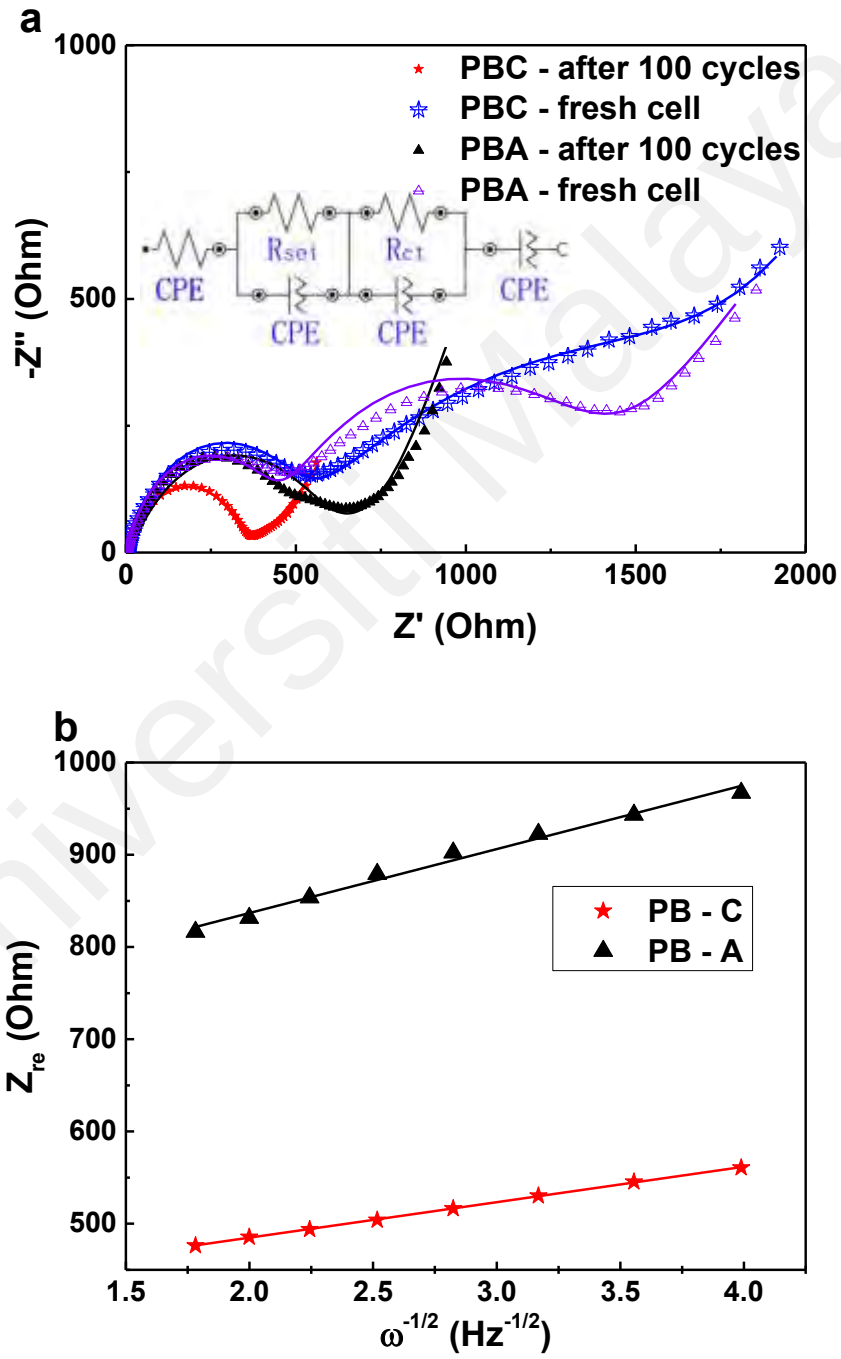

Figure 5.6: (a) Nyquist plot of PB-A and PB-C and (b) the linear relationship between Z_{re} and $\omega^{-1/2}$ at the low frequency region.

To further investigate the electrochemical performance of PB-C cage-like structure, the CV was carried out at the different scan rate of 0.25 mV/s, 0.5 mV/s, 0.75 mV/s, 1 mV/s, 1.25 mV/s, 1.5 mV/s, 1.75 mV/s, and 2 mV/s between the voltage range of 2.0 V and 4.0 V, as shown in Figure 5.7 (a). The curve for the scan rate 0.25 mV/s shows a pair of redox peaks at voltage around 2.97/2.67 V in which correlate well with the charge-discharge profile. As the scan rate increases, the oxidation peaks seem to shift to a higher voltage. To the contrary, the reduction peaks shift to a lower voltage due to the electrochemical polarization. The current in CV curves obeys the power law with formula $i = a\nu^b$ with the detailed explanation in supporting information. Based on Figure 5.3(b), the value of b for cathodic and anodic peaks can be determined, which are 0.92 and 0.83, respectively. From the calculated values of b, it can be considered that the redox reaction and capacitive process have occured during charge-discharge process. Figure 5.7 (c) shows the contribution of the capacitive process (diffusion controlled) for each scan rate, which are 71% (29%), 81% (19%), 83% (17%), 85%(15%), 86% (14%),87% (13%), 88% (12%) and 88% (12%) at the scan rate of 0.25 mV/s, 0.5 mV/s, 0.75 mV/s, 1 mV/s, 1.25 mV/s, 1.5 mV/s, 1.75 mV/s and 2 mV/s, respectively.This suggests that the capacitive process contributes a large part in charge-discharge process. Figure 5.7 (d) shows the calculated ratio of the capacitance of PB-C at the scan rate of 1 mV/s. From the CV test, it can be concluded that the major reason for the excellent performance of PB-C is the pseudocapacitance effect due to the nano-size and cage-like porous structure (F. Cheng, Liang, Tao, & Chen, 2011).

In summary, the nano-size and cage-like porous structure of PB-C are more favorable compared to the dense structure of PB-A as the ion migration paths are shorter and more active sites are exposed for the intercalation of Na^+ to occur. Furthermore, PB-C shows an excellent rate performance at C-rate due to the pseudocapacitance effect (main role of capacitive process during the charge-discharge cycles).

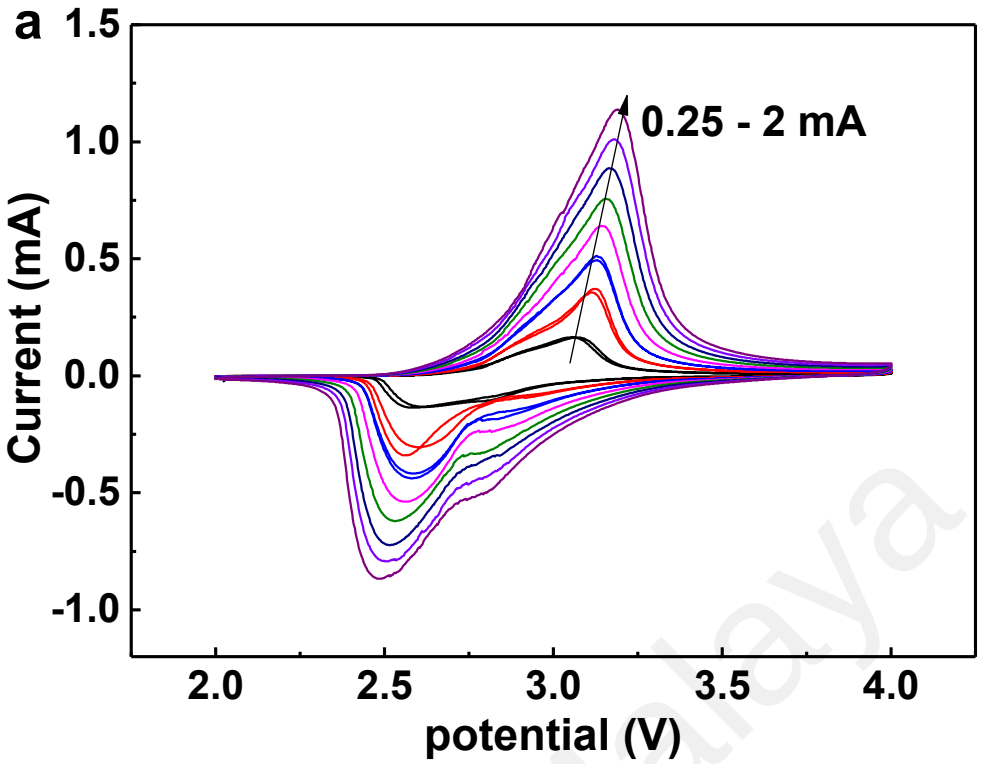

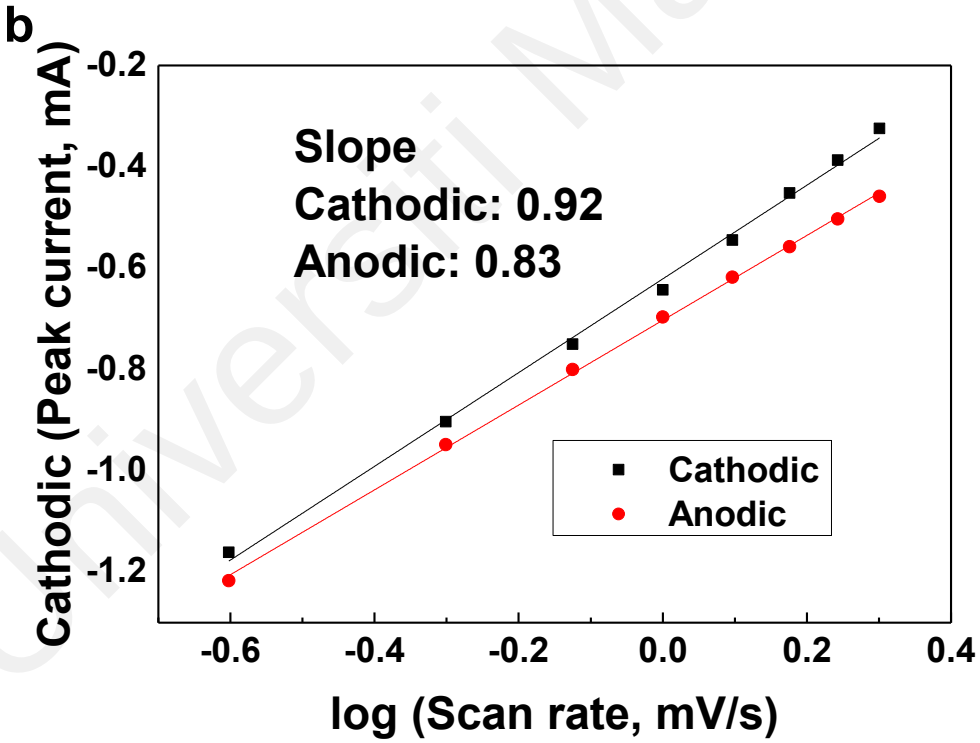

Figure 5.17 continue.

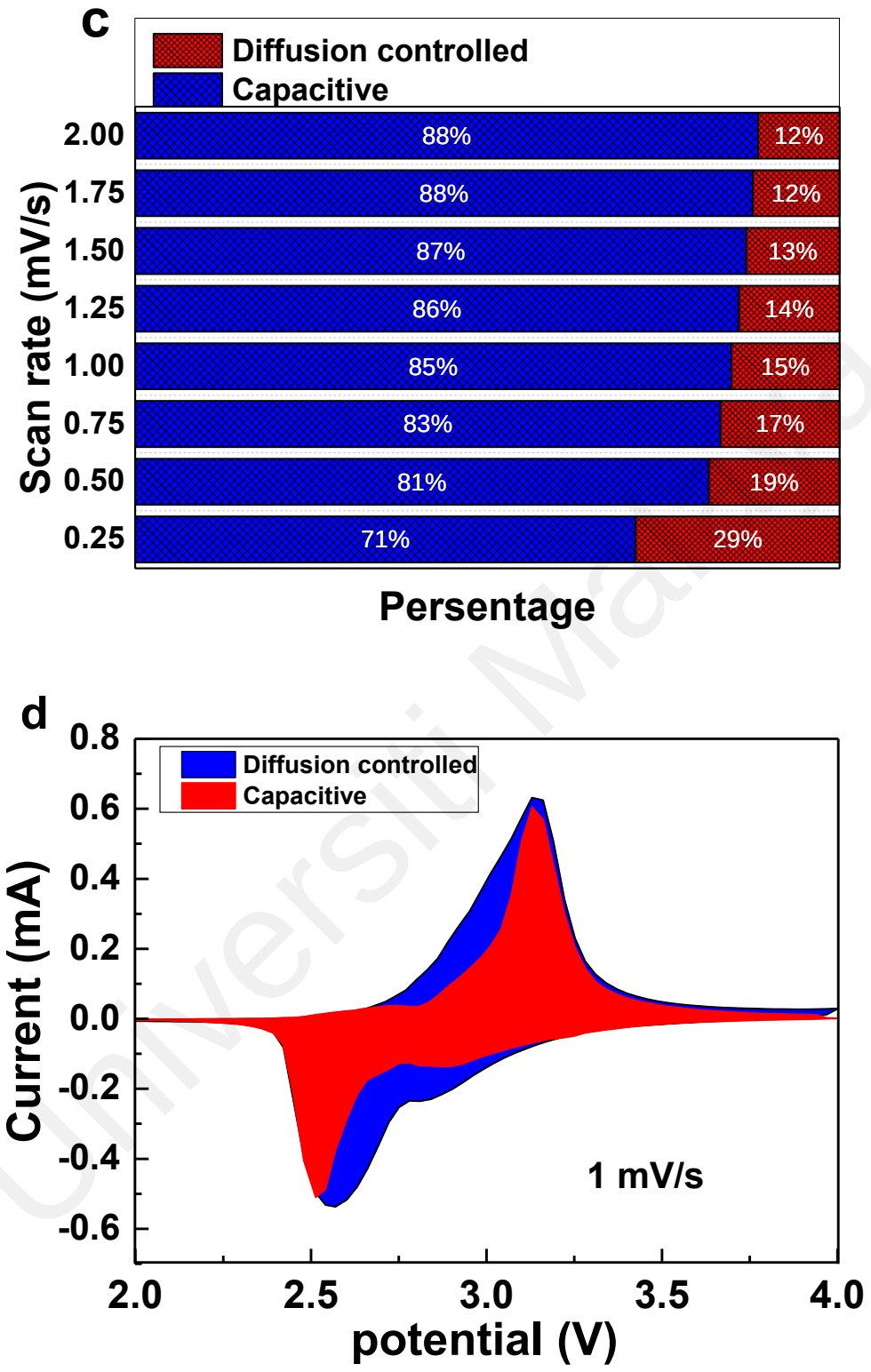

Figure 5.7: (a) CV curves at different scan rates, (b) log plot of cathodic and anodic currents in panel, (c) contribution ratios of the capacitive and diffusion-controlled processes at different scan rates and (d) capacitive and diffusive contributions of PB-C at 1 mV/s.

5.4 Summary

- The cage-like porous structure of sodium iron hexacyanoferrate (PB-C) was synthesized via reheating and an acid-etching method.
- The reheating process enables the reassembly of PBA nanocrystals to form more uniform PBA cubes, while PVP prevents the continuous growth of PBA cubes.
- By the etching process, cage-like porous PBA cubes with an internal hollow cavity is produced with a reduction of water content. The as synthesized PB-C with a cage-like morphology supplies a large specific surface area for excellent electrochemical performance.
- The additional pseudocapacitance and high number of exposed active sites Fe^{2+} increased the overall electrochemical performance of PB-C significantly. PB-C delivered a specific capacity of 112 mAh/g at 0.2 C. No obvious specific capacity fading was observed even at a high current density of 10 C. PB-C also demonstrated outstanding cycling performance (retained over 85% capacity after 1000 cycles) owing to its cage-like structure.
- The capacity contribution from diffusion-limited and non-diffusion limited processes were also investigated.

CHAPTER 6: P2-TYPE TRANSITION METAL OXIDE AS CATHODE MATERIALS FOR SODIUM-ION BATTERIES[3]

6.1 Introduction

In this chapter, Li and Mg are chosen as the substitution elements, and a Li/Mg co–substituted P2–type layered oxide ($Na_{0.67}(Li_{0.5}Mg_{0.5})_{0.1}(Ni_{0.33}Mn_{0.67})_{0.9}O_2$) is prepared by a facile solid–state reaction method. The synergetic effects of alkali and alkaline ions substitutions in the crystal structure, morphology and electrochemical properties are explored in detail.

6.2 Structural and Morphological Characterizations of P2-Type Transition Metal Oxide

The compositions of the Li/Mg co-substituted $Na_{0.67}(Li_{0.5}Mg_{0.5})_{0.1}(Ni_{0.33}Mn_{0.67})_{0.9}O_2$ (LMNM), Li-substituted $Na_{0.67}Li_{0.1}(Ni_{0.33}Mn_{0.67})_{0.9}O_2$ (LNM), Mg-substituted $Na_{0.67}Mg_{0.1}(Ni_{0.33}Mn_{0.67})_{0.9}O_2$ (MNM) and $Na_{0.67}Ni_{0.33}Mn_{0.67}O_2$ (NM) materials are determined to be $Na_{0.63}Li_{0.03}Mg_{0.04}Ni_{0.29}Mn_{0.60}O_2$, $Na_{0.65}Li_{0.08}Ni_{0.31}Mn_{0.62}O_2$, $Na_{0.63}Mg_{0.12}Ni_{0.28}Mn_{0.59}O_2$ and $Na_{0.64}Ni_{0.29}Mn_{0.63}O_2$ by ICP–OES, respectively. The crystal structures of the as–synthesized materials were investigated by XRD, see Figure 6.1. The characteristic reflections of the LMNM, LNM, MNM and NM correspond to P2-type structure with a space group of P63/mmc (PDF–54–0894). A small amount of NiO impurity was detected in the XRD patterns of all the samples, which is attributed to the solubility limit of nickel element in the P2–type structure.(Yongchang Liu et al., 2019) There is one additional reflection at 18.8° shown in the XRD pattern of LNM, which is

[3] **Chapter 6 of this thesis is published as:** Chen, Y., Yang, M., Yang, L., Chen, Z., Li, H., Woo, H. J., . . . Deng, Y. (2023). Alkali and alkaline ions co–substitution of P2 sodium layered oxides for sodium ion batteries. *Chinese Journal of Structural Chemistry*, 100028. doi:https://doi.org/10.1016/j.cjsc.2023.100028

possibly due to the formation of Li–contained O3 phase in the LNM.(Z.-Y. Li et al., 2022) The lattice parameters obtained from the refinements for the XRD patterns of the LMNM, LNM, MNM and NM are listed in

Table 6.1. As can be seen, the lattice parameter *c* values of the LMNM, LNM, MNM and NM are 11.1496 Å, 11.0712 Å, 11.1989 Å and 11.1631 Å, respectively. The Li doping (LNM) results in the decrease of the *c* value, while the Mg doping (MNM) has an increase of the *c* value. For the Li and Mg co-doping (LMNM), the *c* value is between them. Neutron powder diffraction (NPD) combining with Rietveld refinement was conducted to further study the structures of the LMNM Figure 6.2) and NM (Figure 6.3) as a comparison. As can be seen from Figure 6.2 and Figure 6.3a, both the LMNM and NM show negligible NiO impurities, and the major reflections are assigned to P2 phase. As Ni and Mn can be clearly distinguishable by NPD, a lower symmetric space group than $P6_3/mmc$ is needed to describe new ordered state in the sample. As illustrated in Figure 6.2b, the honeycomb-like *TM*@Mn_6 (*TM* = Li, Mg, Ni) superstructures can be well refined by $P6_3$ structure model(Z. Lu, Donaberger, & Dahn, 2000). Figure 6.3 shows the similar NPD pattern owing to the Ni@Mn_6 superstructures (Figure 6.3b).

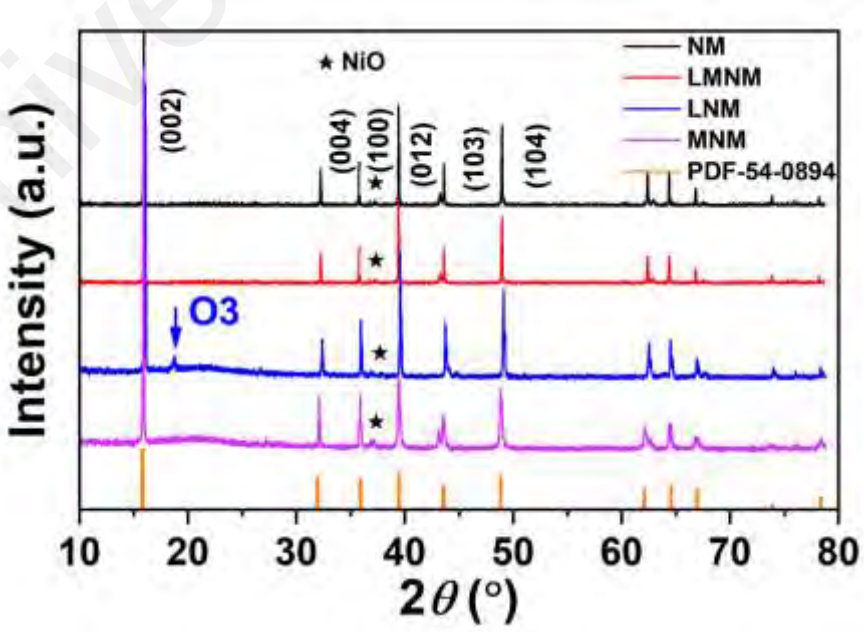

Figure 6.1: XRD patterns of LMNM, LNM, MNM and NM materials.

Table 6.1: Atomic parameters and unit constants calculated from the Rietveld refinement results from the XRD patterns of LMNM, LNM, MNM and NM.

	LMNM	LNM	MNM	NM
a (Å)	2.8907	2.8865	2.88471	2.8865
b (Å)	2.8907	2.8865	2.88471	2.8865
c (Å)	11.1496	11.0712	11.1989	11.1631
α (°)	90	90	90	90
β (°)	90	90	90	90
γ (°)	120	120	120	120
V (Å^3)	80.69	79.89	80.71	80.55

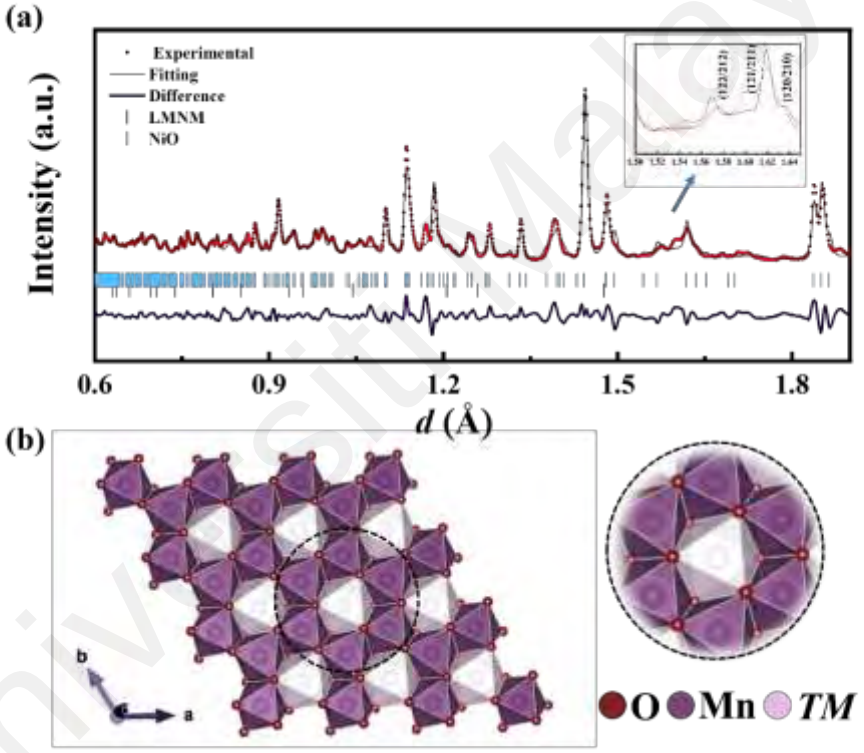

Figure 6.2: (a) NPD pattern and Rietveld refinement results of LMNM. (b) Crystal structure of LMNM viewed along the *c*-axis with honeycomb-like *TM*@Mn6 superstructures (*TM* = Li, Mg, Ni).

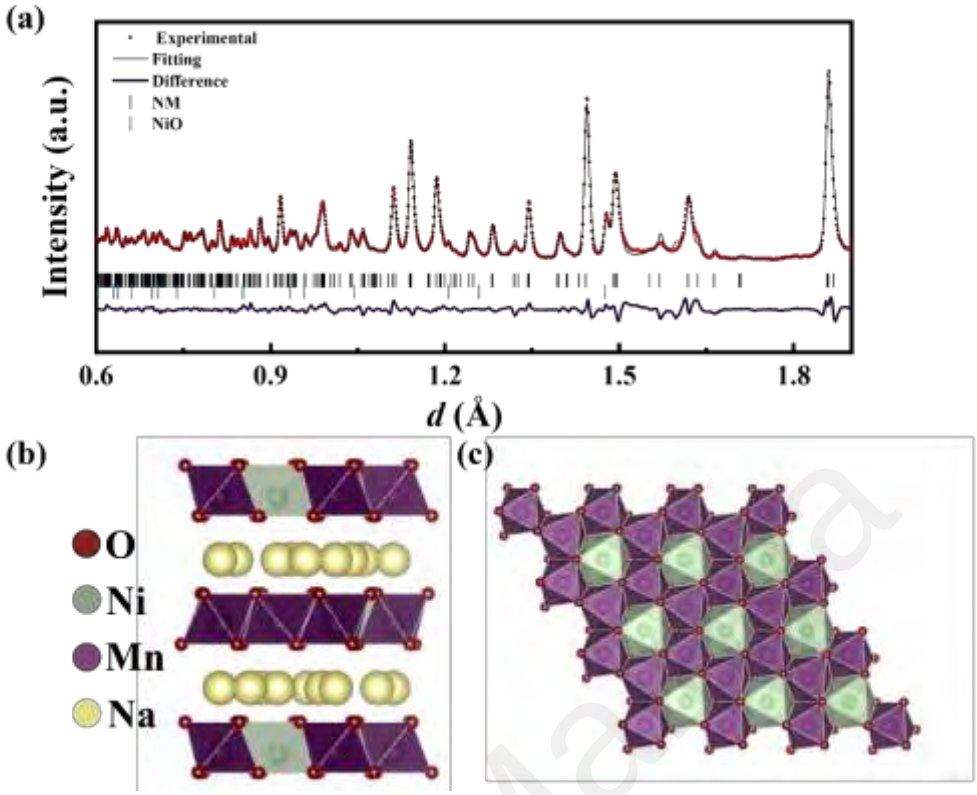

Figure 6.3: (a) NPD pattern and Rietveld refinement result of NM. Crystal structure of NM viewed along (b) *a*-axis and (c) *c*-axis.

The scanning electron microscopy (SEM) images of all the four samples are shown in Figure 6.4. The NM shows the particle size of several micrometers. After substitutions, all the doped samples (LMNM, LNM and MNM) exhibit similar morphology with the NM, but more small particles are observed on the particle surface, which is probably due to the impure NiO phase. Transmission electron microscopy (TEM) coupled with energy dispersive spectroscopy (EDS) mapping was further employed to clarify the structure and element distribution of the as–synthesized materials in Figure 6.5 - Figure 6.8. Typically, the LMNM shows a spacing of 0.56 nm from the (002) of P2 structure. The surface element distributions of all the samples are all as expected. It should be noted that Li is not able to be detected in the EDS mapping results of the LMNM and LNM (Hovington et al., 2016).

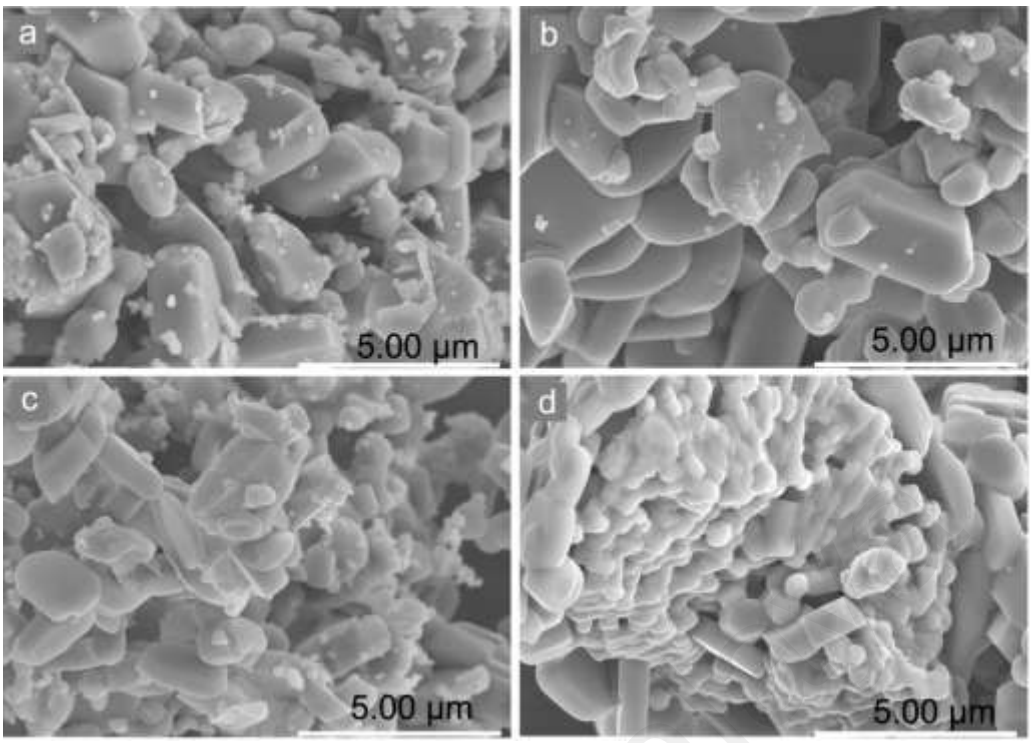

Figure 6.4: SEM images of (a) LMNM, (b) LNM, (c) MNM and (d) NM.

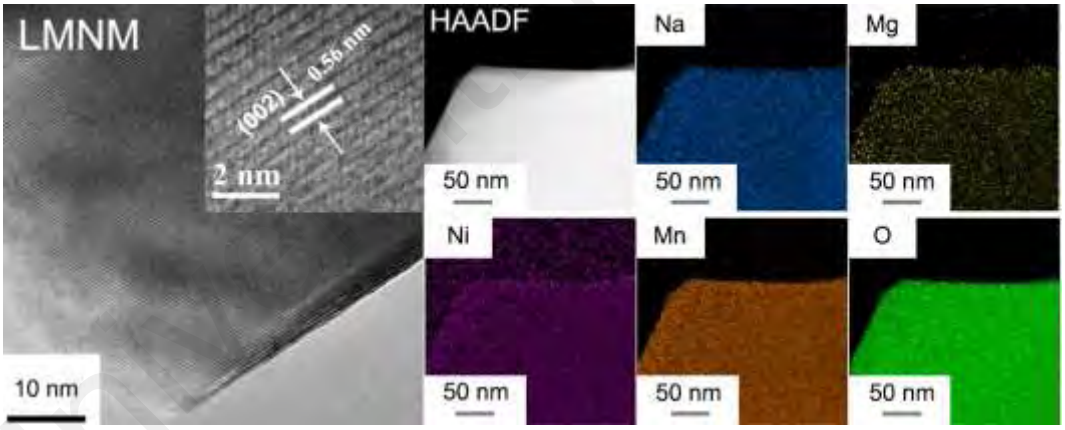

Figure 6.5: TEM image and corresponding EDS mapping images of LMNM.

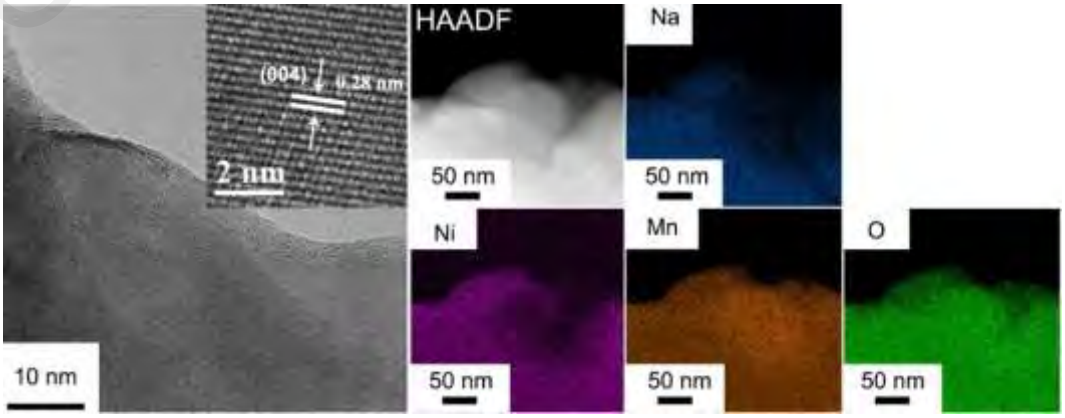

Figure 6.6: TEM image and corresponding EDS mapping images of LNM.

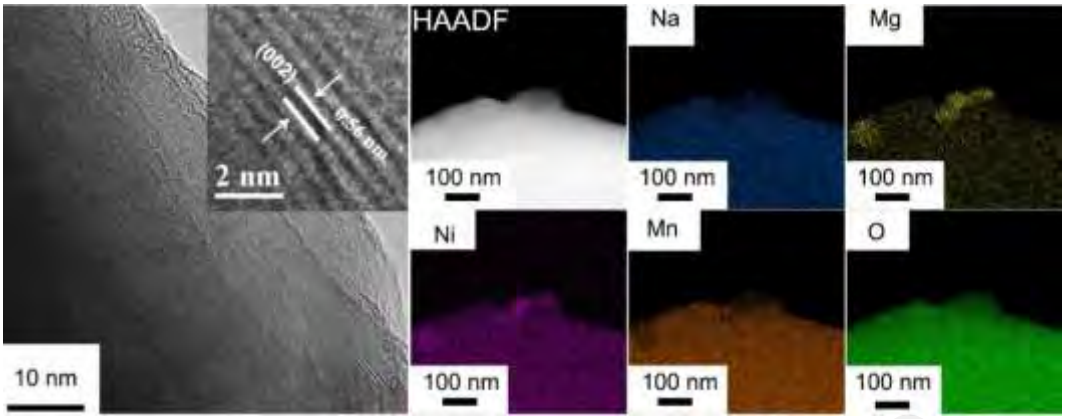

Figure 6.7: TEM image and corresponding EDS mapping images of MNM.

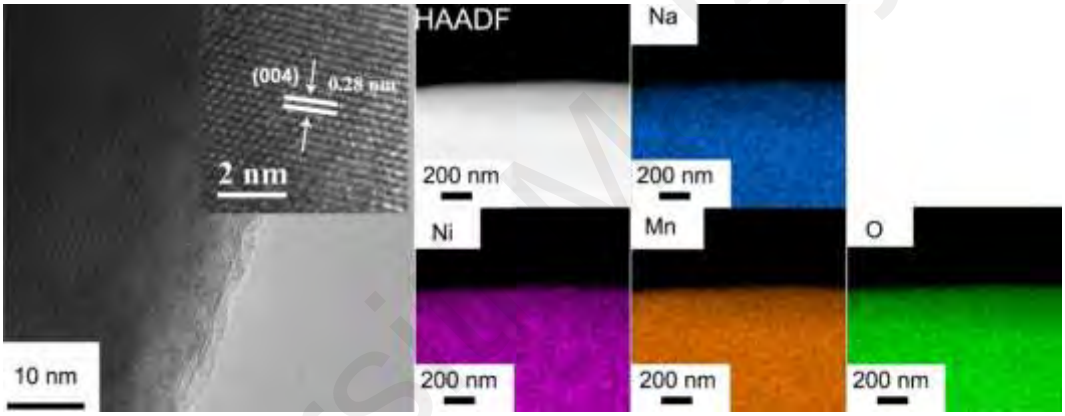

Figure 6.8: TEM image and corresponding EDS mapping images of NM.

The elemental compositions are carried out by XPS. As shown in Figure 6.9, survey spectra demonstrate the existence of Na, Ni, Mn, O elements, corresponding to the binder energy of ~1069 eV, ~855 eV, ~641 eV and ~528 eV, respectively. The high-resolution spectra are shown in Figure 6.10. All spectra show that peaks of Ni $2p_{3/2}$ and Ni $2p_{1/2}$ are located at 855.2 eV and 873.3 eV, respectively, indicating that the valance of Ni ion is +2.

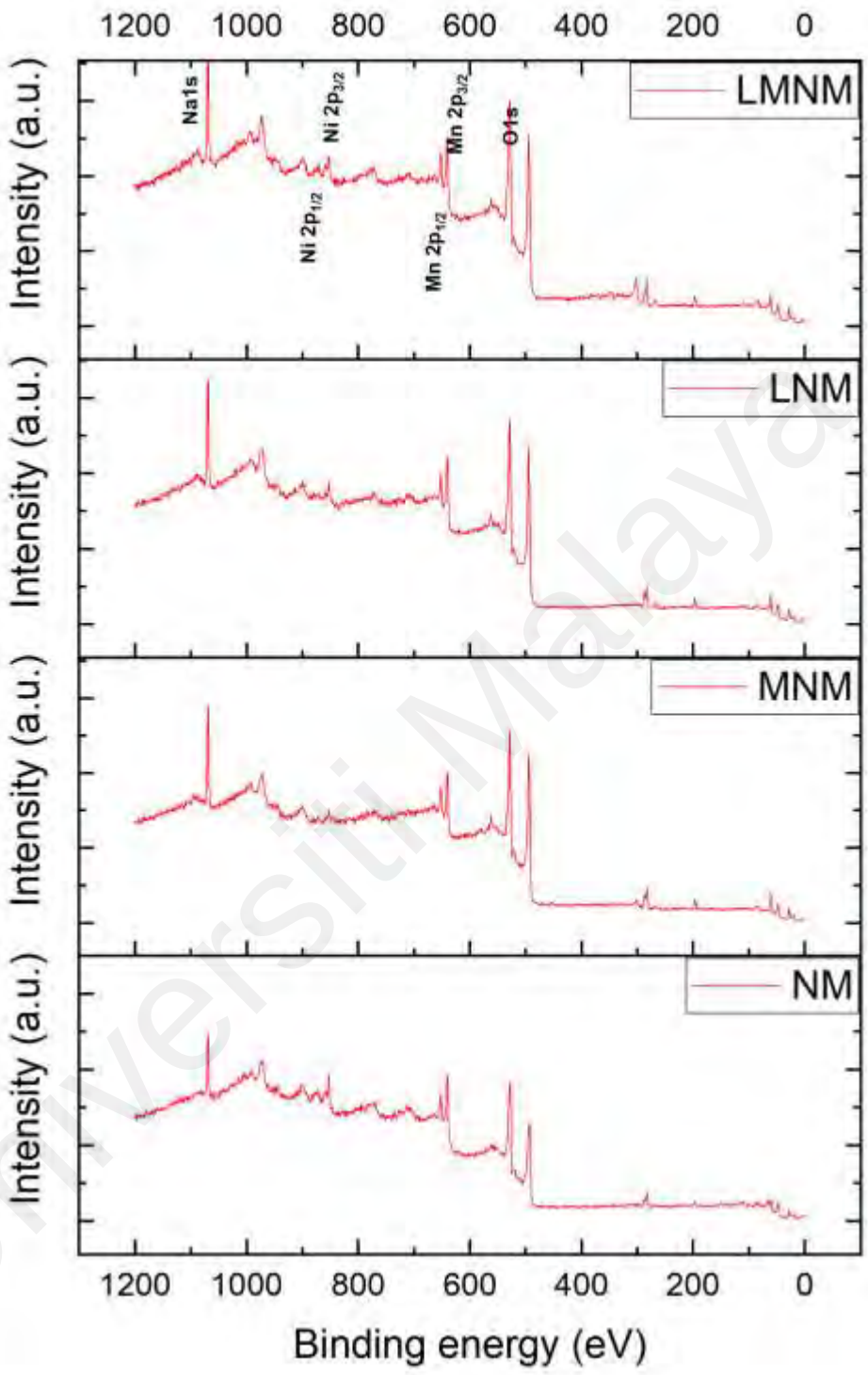

Figure 6.9: **XPS survey spectra of LMNM, LNM, MNM and NM.**

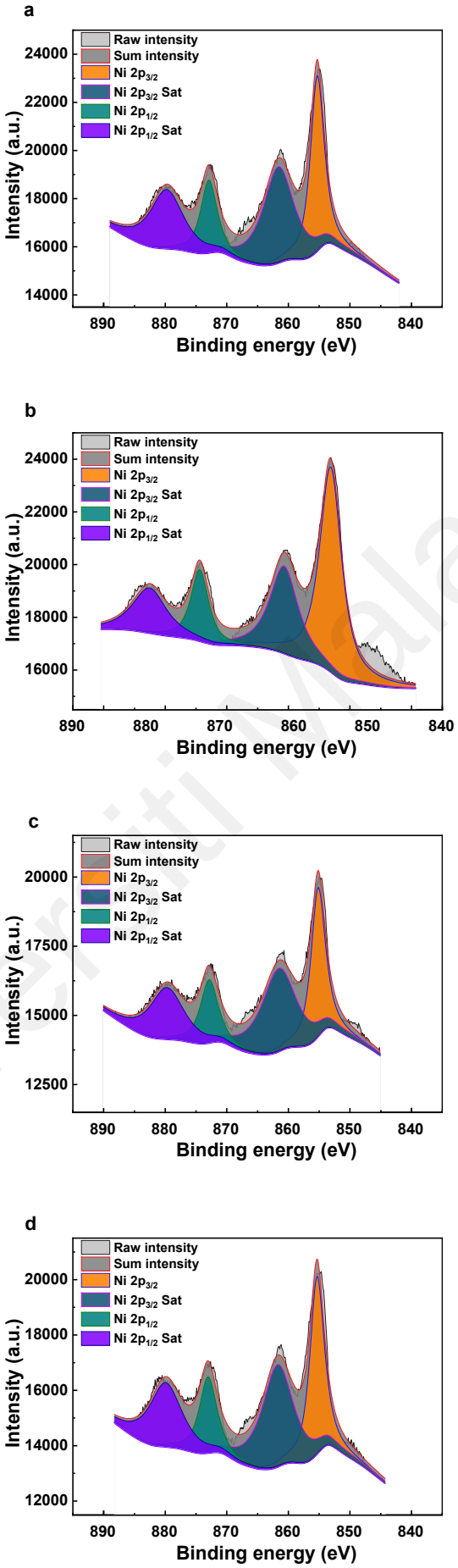

Figure 6.10: XPS spectra for Ni of (a) LMNM, (b) LNM, (c) MNM, (d) NM.

6.3 Electrochemical Characterizations of P2-Type Transition Metal Oxide

The electrochemical properties of the LMNM, LNM, MNM and NM were studied in half cells using sodium metal as anode. As shown in the initial charge/discharge curves of the LMNM, LNM, MNM and NM at 0.1 C (Figure 6.11), they show different charge/discharge curves. It is considered that the complex plateaus of layered sodium-ion cathode materials are attributed to multiple phase transitions and Na-vacancy ordering during the sodiation and desodiation processes (J. Li et al., 2019; Risthaus et al., 2018). The introduction of heteroatom would influence the phase transitions and Na-vacancy ordering upon charging/discharging, thus they display different charge/discharge curves. The LMNM displays less plateaus than the LNM, MNM and NM, indicating that the Li/Mg co-substitution could decrease Na/vacancy-related plateaus (Z. Cheng et al., 2022; J. Li et al., 2020). This phenomenon is also observed in the charge/discharge curves of the LMNM Figure 6.11b), NM, LNM and MNM (Figure 6.12) upon prolonged cycling.

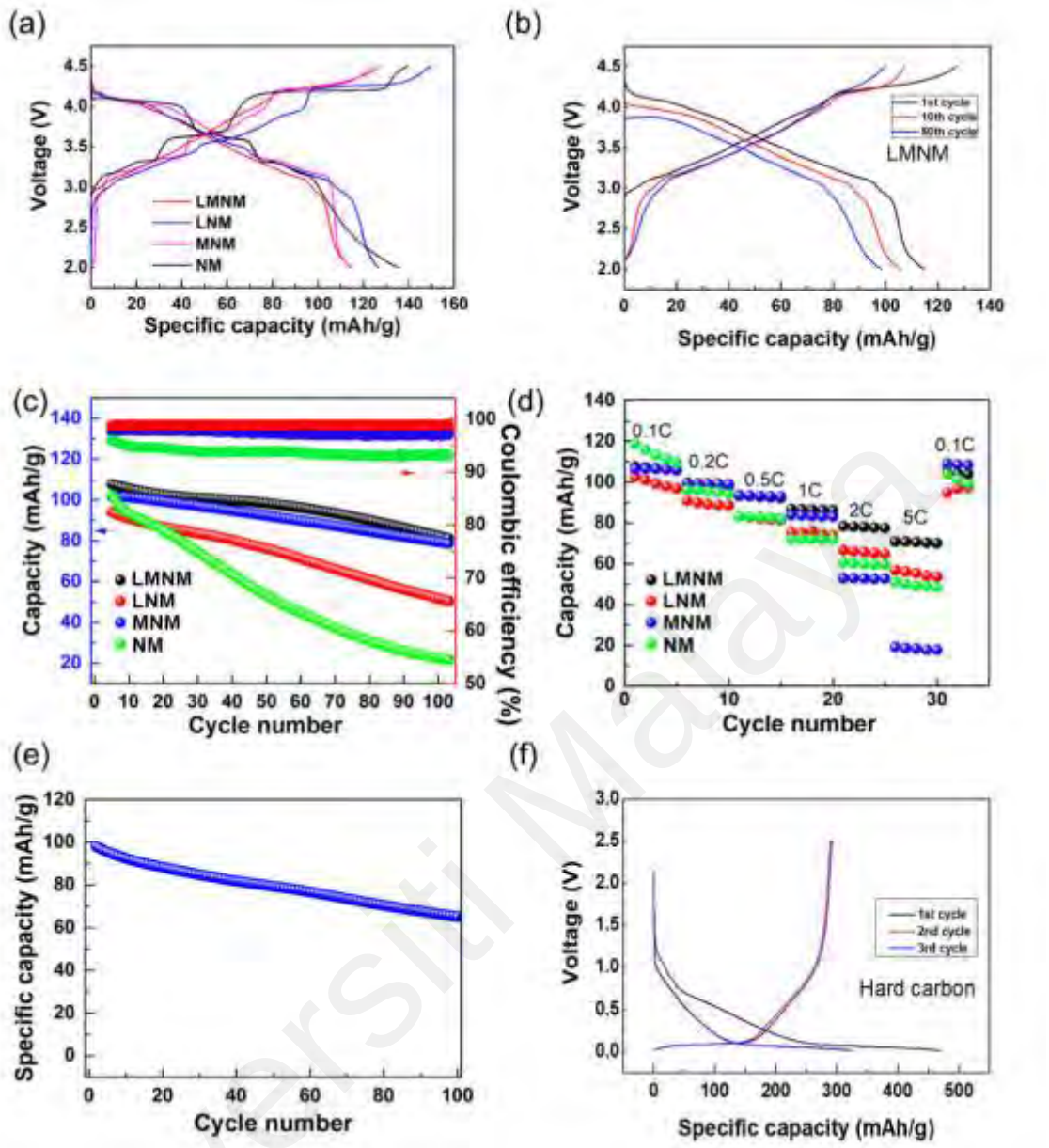

Figure 6.11: (a) Initial galvanostatic charge and discharge curves of LMNM, LNM, MNM and NM at 0.1 C in the voltage range of 2.0–4.5 V. (b) Charge and discharge curves of LMNM at 0.5 C. (c) Cycling performance of LMNM, LNM, MNM and NM at 0.5 C. (d) Rate capabilities of LMNM, LNM, MNM and NM at various rates in the voltage range of 2.0–4.5 V. (e) Cycling performance of LMNM//hard carbon full cell at 0.5 C in the voltage range of 1.9–4.4 V. (f) Charge and discharge curves of hard carbon for initial three cycles at 0.25 C in the voltage range of 0.01–2.5 V.

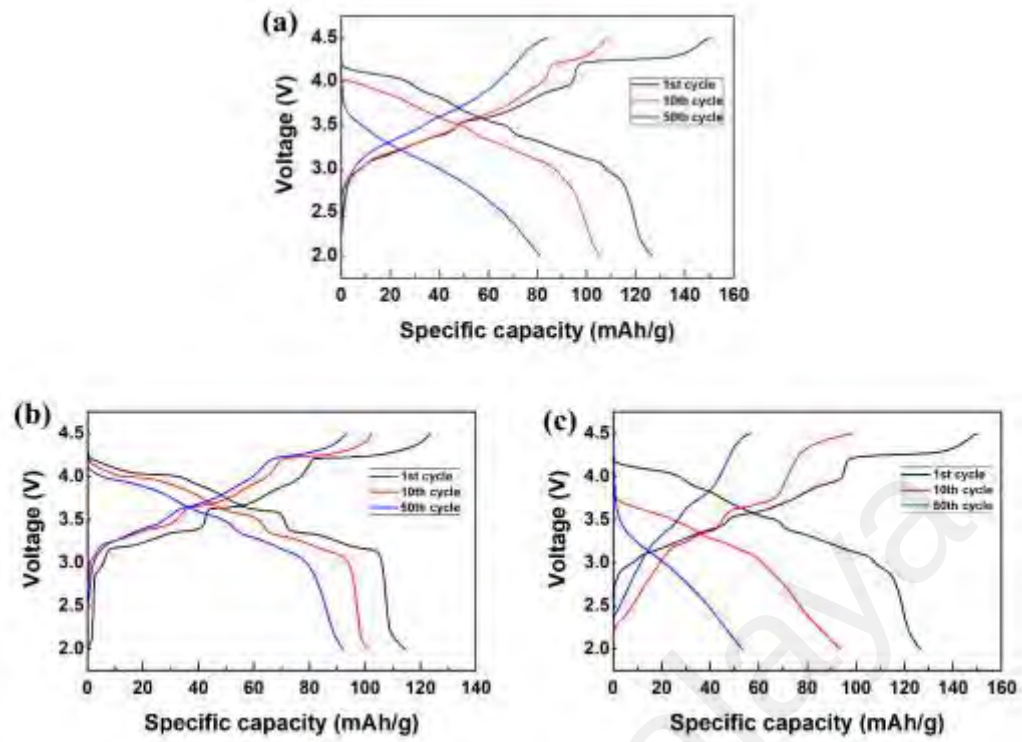

Figure 6.12: Galvanostatic charge and discharge curves of (a) LNM, (b) MNM and (c) NM at 0.5 C upon cycling.

The LMNM, LNM, MNM and NM show initial discharge capacities of 115 mAh/g, 127 mAh/g, 115 mAh/g and 135 mAh/g, respectively. The substituted samples show lower specific capacity probably caused by the decreased amount of transition metals with redox activity. Nevertheless, the substitution enables improved cycling performance. In detail, as shown in Figure 6.11 (at the rate of 0.5 C), the NM delivers a specific discharge capacity of 103 mAh/g in the 4th cycle and maintains a specific discharge capacity of only 22 mAh/g after 100 cycles, corresponding to the capacity retention of 21%. By contrast, the LMNM, LNM and MNM exhibit capacity retentions of 75%, 77%, and 54%, respectively. In addition, the average Coulombic efficiencies of the LMNM, LNM, MNM and NM are 98%, 97%, 99% and 94%, respectively, which correspond to the above difference in cycling performance. Figure 6.13 shows the CV curves of the LMNM, LNM, MNM and NM at 0.05 mV/s. The reversibility of the highest oxidation peak for the LMNM, LNM, MNM and NM shows the tendency of MNM > LMNM >

LNM > NM, which is consistent with the above cycling performance. With the substitutions, the simplified electrochemical reactions might be responsible for the improved cycling performance, which will be discussed further in the following parts.

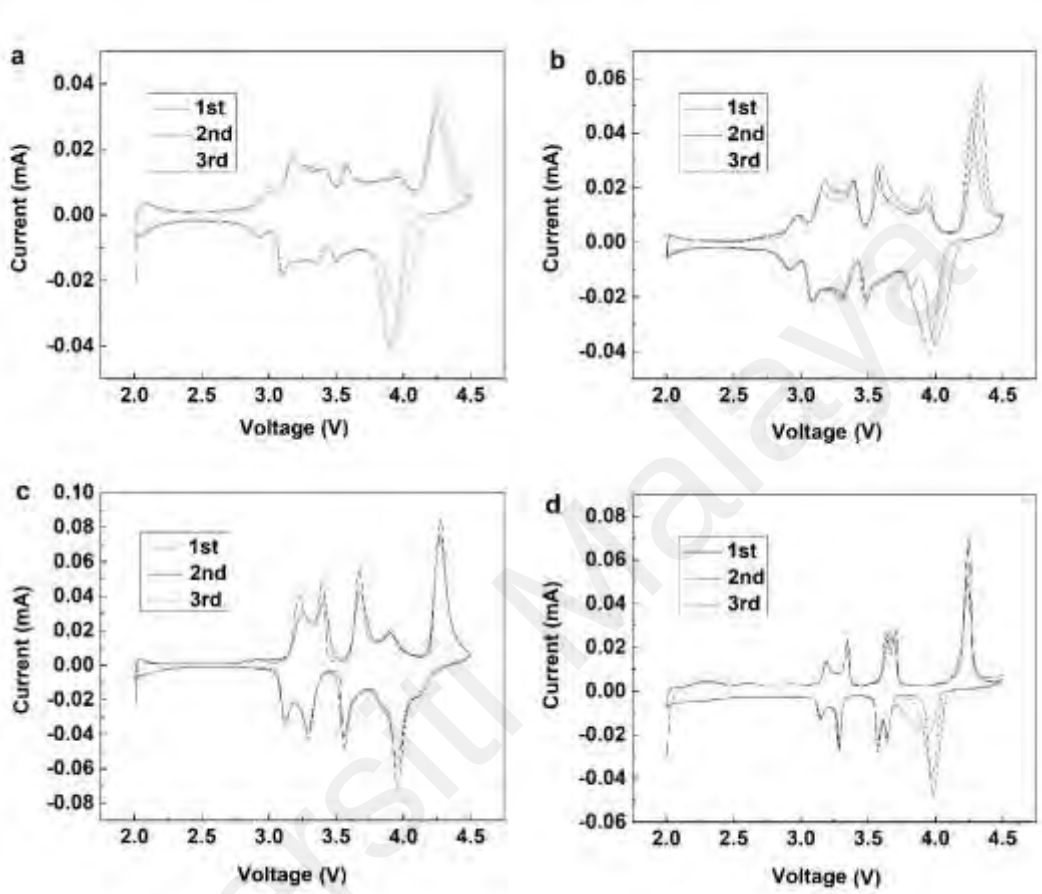

Figure 6.13: CV curves of (a) LMNM, (b) LNM, (c) MNM and (d) NM at 0.05 mV/s.

Besides, the co-substitutions contribute to enhance rate capability. The discharge capacities of the LMNM, LNM, MNM and NM at rates varying from 0.1 C to 5 C are displayed in Figure 6.11d. As can be seen, the LMNM, LNM, MNM and NM deliver discharge capacities of 61 mAh/g, 67 mAh/g, 53 mAh/g and 78 mAh/g at 2 C, respectively, which are 72%, 66%, 50% and 51% of the corresponding values at 0.1 C. It is obvious that the rate capability of the LMNM is the best among them. In comparison with other investigations of elemental doping for P2-type $Na_{0.67}Ni_{0.33}Mn_{0.67}O_2$, this work shows different effects. Several research groups have found that Li doping is beneficial

for the enhancement of anion redox reaction besides of stabilizing the structure, thus increasing capacities in layered sodium–ion cathode materials (C. Ma et al., 2017; Risthaus et al., 2018; Rong et al., 2019; Rong et al., 2018; L. Yang et al., 2020; Liangtao Yang et al., 2021). However, it is not the same in our work. Herein, the Li doping improves Na^+ ion diffusion coefficient, thus enhancing the rate capabilities of the LMNM and LNM, which will be studied in the following parts. For the Mg doping (MNM), it mainly helps to stabilize the crystal structure, which is similar with other Mg doping investigations for layered sodium-ion cathodes (Buchholz, Vaalma, Chagas, & Passerini, 2015; J. Li et al., 2019). It should be noted that the use of different raw materials, the capacity values of the NM are a bit lower than the reported ones (T. Chen et al., 2022; Feng et al., 2022; H. Hu, Tang, Cao, Yang, & Wang, 2021; Lei et al., 2022; Pei et al., 2022; Ren et al., 2022; Tapia-Ruiz et al., 2018; Liu Yang et al., 2021; F. Zhang, Liao, Xu, Wu, & Wu, 2021).

When the LMNM is cycled at 5 C, it keeps a capacity retention of 74% after 200 cycles (Figure 6.14). To further verify the practical application potential of the LMNM, full cells using the LMNM as cathodes and hard carbon were assembled. The cycling performance of the LMNM//hard carbon cell is shown in Figure 6.11. As can be seen, the LMNM//hard carbon cell exhibits an initial discharge capacity of 98 mAh/g at the beginning at 0.5 C within the voltage range of 1.9–4.4 V. It keeps a discharge capacity of 65 mAh/g after 100 cycles, corresponding to a capacity retention of 66%. It should be noted that the hard carbon was (de)sodiated for three cycles at 0.25 C in the voltage range of 0.01–2.5 V before being used in the full cells (Figure 6.11). These results suggest that the LMNM is a promising cathode material for SIBs.

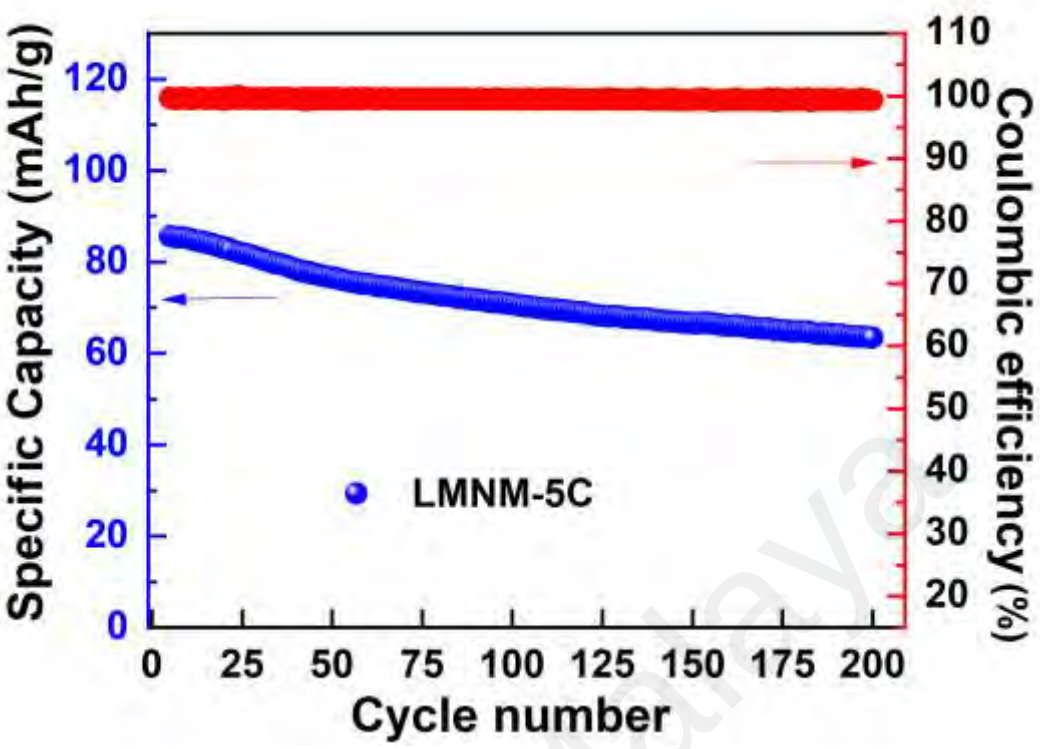

Figure 6.14: Cycling performance of LMNM at 5 C for 200 cycles.

To analyze the kinetics of Na^+ in the electrodes, GITT measurements were performed on the LMNM, NM, LNM and MNM in the voltage ranges of 2.0-4.5 V at 0.1 C, the results of which are shown in Figure 6.15. It shows tiny difference of Na^+ diffusion coefficients among the four electrodes when the voltage is below 4.15 V. However, the NM electrode displays a sharp drop in the Na^+ diffusion coefficient up to the high-voltage range, which is not the same case for the substituted samples, indicating that the substitutions could improve the kinetics for Na^+ diffusion in the high-voltage range during charge/discharge. To further understand the kinetic properties and charge storage behaviors of the LMNM, NM, LNM and MNM electrodes, CV measurement at different scan rates ranging from 0.05 to 2.0 mV s^{-1} were carried out. Figure 6.16 shows the obtained CV curves of the LMNM, NM, LNM and MNM and the corresponding linear fits of peak currents. The Na^+ diffusion coefficient is positively related to the slope of the redox peak currents and scan rate (J. Li et al., 2020). As can be seen, both the cathodic

and anodic slopes of the Li and Mg substituted electrode are remarkably higher than the pristine electrode. Besides, the slope value of the LMN is larger than that of the MNM. It indicates that Li plays a major role in improving the Na^+ diffusion coefficients. Overall, Li and Mg co-substitution in P2 material significantly enhances the Na^+ diffusion coefficient, as shown in Table 6.2. The above results explain the enhanced rate capability of the Li and Mg co–substituted electrode material.

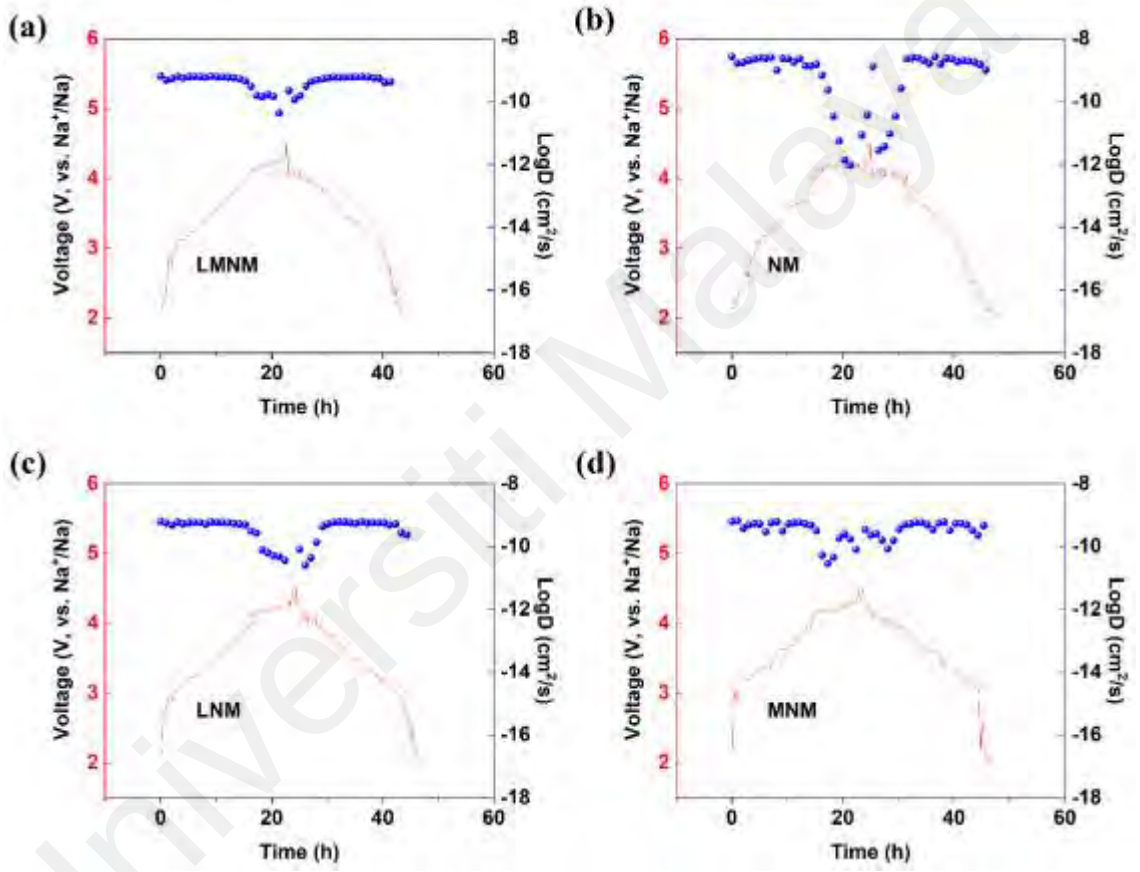

Figure 6.15: GITT curves of (a) LMNM, (b) NM, (c) LNM and (d) MNM, respectively. (c and d) CV curves of LMNM and linear fits of peak currents, respectively.

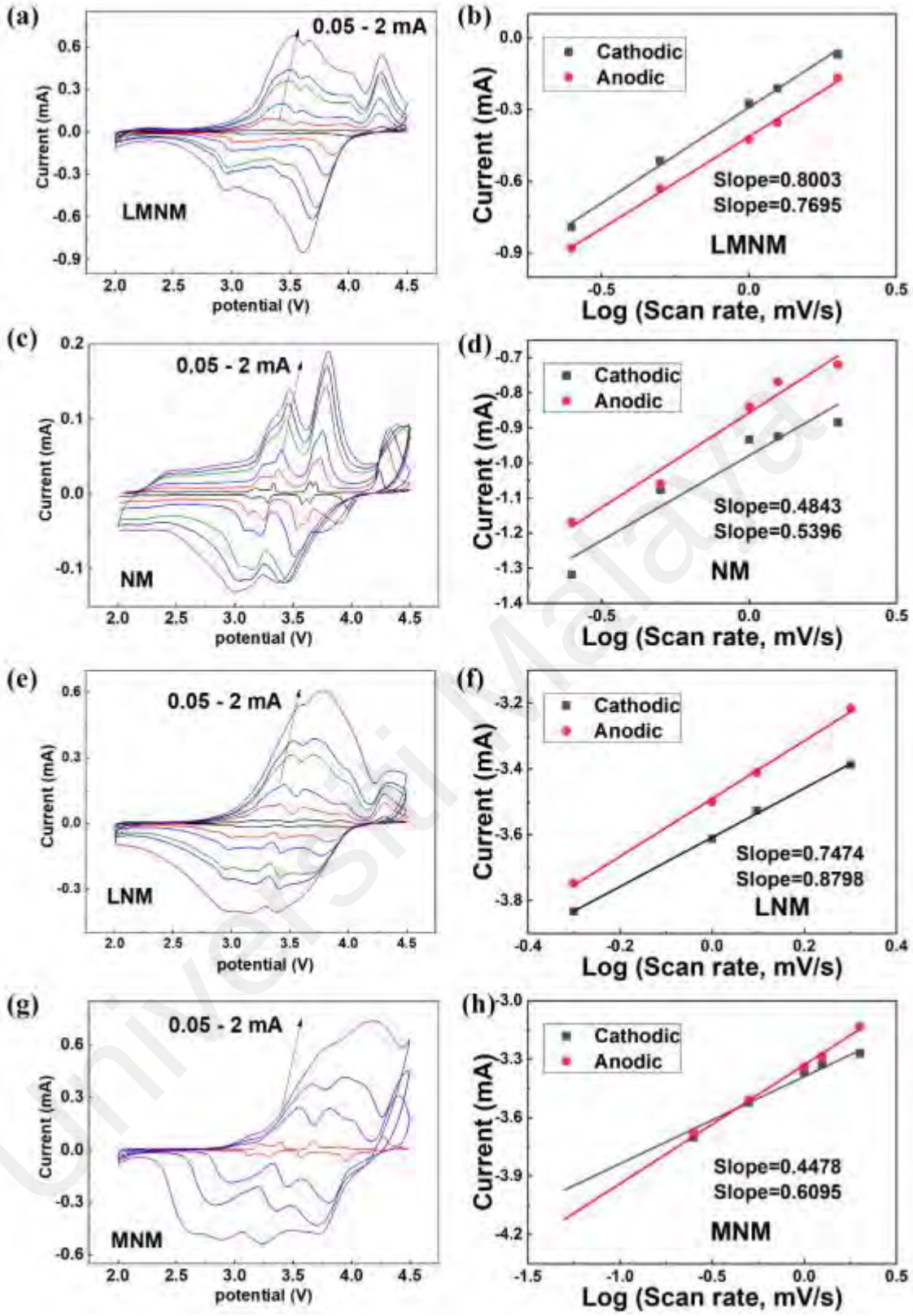

Figure 6.16: CV curves of the LMNM, NM, LNM and MNM and the corresponding linear fits of peak currents, respectively.

Table 6.2: Na^+ diffusion coefficients of LMNM, LNM, MNM and NM calculated from corresponding CV curves.

	LMNM (cm^2/s)	LNM (cm^2/s)	MNM (cm^2/s)	NM (cm^2/s)
Oxidation	2.33×10^{-11}	2.00×10^{-11}	7.31×10^{-12}	8.55×10^{-12}
Reduction	2.16×10^{-11}	2.82×10^{-11}	1.35×10^{-11}	1.06×10^{-11}

For a better understanding of the detailed structural evolution of the LMNM, operando XRD was carried out during the first desodiation and sodiation process, and the patterns are shown in Figure 6.17. At the beginning of desodiation up to 4.0 V, the P2 structure maintains without any phase transition, indicating a 'solid solution' reaction mechanism. The (002) and (004) reflections of P2 phase shift gradually to lower degree, while the (100) and (102) reflections of P2 phase move towards a higher degree, indicating the contraction of *a* axis and expansion of *c* axis during desodiation. When the charging voltage is above 4.0 V, the (002) and (004) reflections of P2 phase almost vanish, and a new reflection appears at $2\theta \approx 17°$, indicating the occurrence of P2–>OP4 phase transition (C. Wang et al., 2021; Xiao et al., 2022). Comparing with another high-voltage phase (O2 phase), the OP4 phase is thermally more stable (Somerville et al., 2019). Fortunately, these shifted and disappeared reflections return back to the initial states during discharge. The phase transition and its reversibility explain the enhanced sodium storage property of the Li and Mg co–substituted material. For comparison, there is a new peak of (002'), indicating the O2 phase of the NM sample in the charge state of 4.5 (Figure 6.18) (Z. Lu & Dahn, 2001).

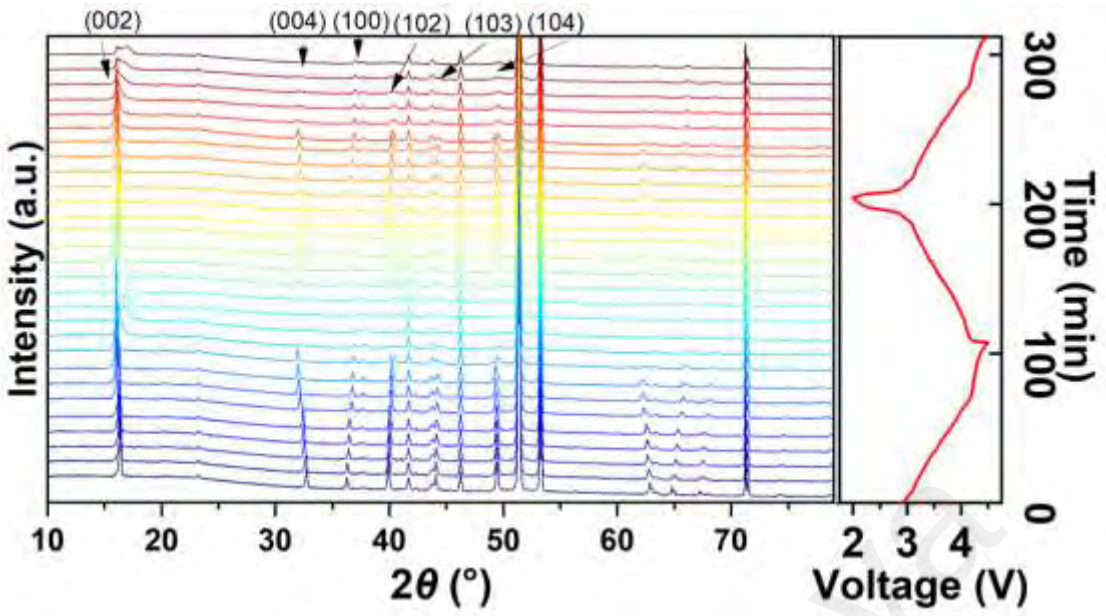

Figure 6.17: Operando XRD results of LMNM upon charging/discharging. Waterfall diagram and initial charge/discharge curves.

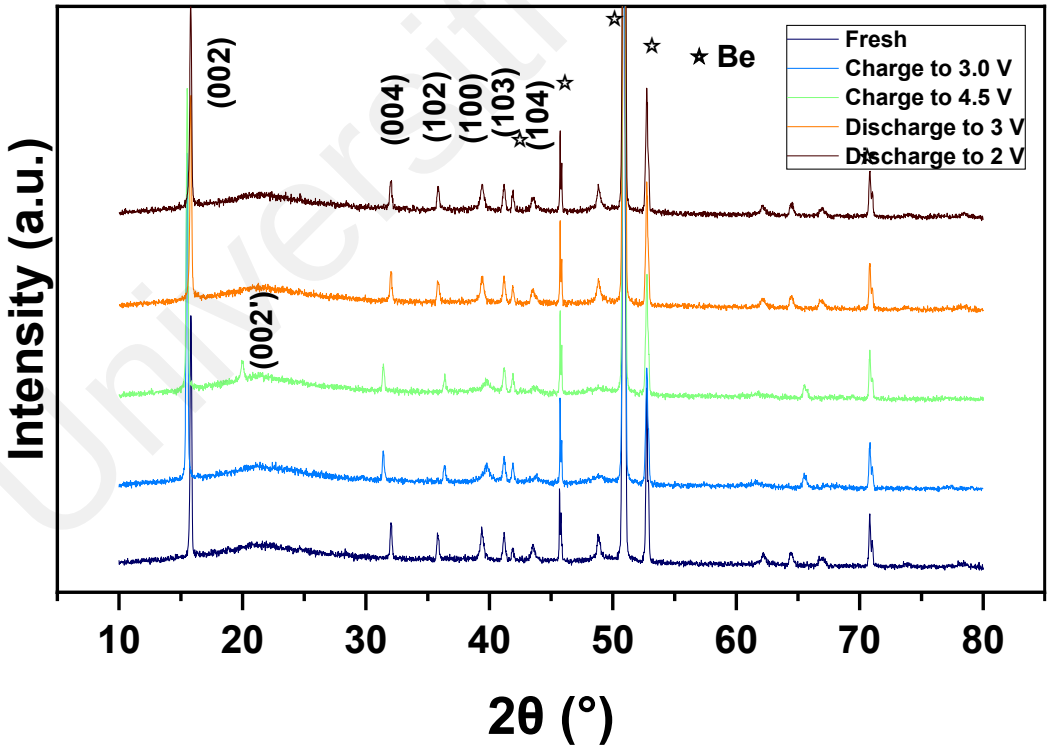

Figure 6.18: Ex-situ XRD in different voltage of NM sample.

6.4 Summary

- A P2-type $Na_{0.67}(Li_{0.5}Mg_{0.5})_{0.1}(Ni_{0.33}Mn_{0.67})_{0.9}O_2$ material designed with the aim of using the synergetic effects of Li and Mg ions has been successfully prepared.
- The Li substitution was found to be preferential for the enhancement of Na^+ ion diffusion coefficient, and the Mg substitution was particularly beneficial for improving cycling stability.
- The Li and Mg co-substitution synergistically ameliorated the capacity fading while boosted the Na^+ ion diffusion capability, especially in high-voltage ranges.
- Operando XRD results proved that the Li and Mg co-substituted material had distinct structural changes from P2 to OP4 rather than O2 for the un-doped material, demonstrating less structural changes, which contributed to the above improvements. As a result, the as-synthesized Li and Mg co-substituted LMNM layered oxide delivered a reversible specific capacity of 86 mAh/g at 5C with the cut-off voltage of 4.5 V and 74% capacity retention after 200 cycles.

CHAPTER 7: DISCUSSION, CONCLUSION AND FUTURE WORK

7.1 Introduction

In this chapter, the effect of materials synthesizing method and the materials characterization of PBA and P2-type TMO will be discussed.

PBA is synthesized using the precipitation method. This method involves the chemical precipitation of the desired components from a solution, leading to the formation of PBA nanoparticles or structures. Two sub-works of PBA will be discussed: component regulation and morphology modification. Component regulation involves adjusting the composition of the PBA material to enhance its electrochemical properties, while morphology modification focuses on changing the physical structure of the PBA material to improve its performance. For P2-type TMO, the solid-state method is used as the synthesizing method. This method involves the direct reaction of solid precursors at elevated temperatures, resulting in the formation of the desired P2-type TMO material. The effect of modifying the P2-type TMO structure through the substitution of different elements will be discussed. This substitution can lead to variations in the structure, morphology, and electrochemical performance of the P2-type TMO material.

Later the chapter will discuss the effects of these different synthesis and modification methods on the structural, morphological, and electrochemical properties of PBA and P2-type TMO materials. The advantages and disadvantages of each material will be highlighted, providing a comprehensive understanding of their characteristics.

In the conclusion section, a summary of the performance of each material studied in this work will be presented. A comparison of different materials will be made to identify their relative strengths and weaknesses.

Lastly, the future work section will outline potential avenues for further research and development in the field of P2-type TMO and PBA materials. This will provide insights into the potential directions and advancements that can be pursued to improve the performance and applicability of these materials.

7.2 Discussion of PBA

In Chapter 4 and 5, the focus was on the characterization and electrochemical performance of PBA materials with different Na contents or different morphologies.

In the sub-work of PBA with different Na contents, it was found that the PBA sample with a high Na content exhibited the highest stability. This was attributed to the low interstitial water content and low vacancies rate in the high Na content PB. These factors indicated that increasing the Na content in PBA is an effective strategy for reducing interstitial water and vacancies, which are crucial for achieving high electrochemical performance. This observation was further supported by Fourier-transform infrared FTIR analysis, which confirmed the lower interstitial water content in Na-rich PB. Subsequently, in the electrochemical performance evaluation, the Na-rich PBA demonstrated the best performance. Furthermore, the synthesis environment was found to influence the morphology of PB, as depicted in Figure 4.3. Na-rich PBA exhibited a high surface area, providing more active sites for Na.

In the second sub-work of PB, the goal was to increase the surface area of PB. To achieve this, an etching method was employed. Interestingly, even with a similar process, different products were obtained. The re-heating process resulted in the formation of cage-like PBA structures with a high surface area, which in turn provided more active sites for Na.

Overall, the findings highlighted the importance of Na content and morphology in determining the electrochemical performance of PB. Increasing the Na content led to improve stability and performance, while modifying the morphology allowed for a higher surface area and enhanced active site availability. These insights contribute to a better understanding of PBA materials and provide valuable information for optimizing their electrochemical properties.

In term of electrochemical performance. The discharged capacities during the first cycle are 109 mAh/g (PB-0M), and 130 mAh/g (PB-4M). When the current density is increased, PB-0M shows the discharge capacity which is 62 mAh/g 5C. PB-4M has shown the discharge capacities of 110 mAh/g at 5C. When the test temperature increases to 80 ℃, all the samples except PB-4M become unstable. After a few charge/discharge cycles at 80 ℃, the specific capacity of PB-0M deteriorates to almost 0 mAh/g while the reversible capacity of PB-4M is more than 100 mAh at 5 C. For comparison, PB-4M and PB-2M have been tested for the long cycling performance at 80 ℃ for 500 cycles (Figure 4.12). PB-4M shows a high specific discharge capacity of 108 mAh/g and remains a reversible specific discharge capacity of 58 mAh/g after 500 cycles. Comparing with PB-4M, PB-2M shows the initial specific capacity is 98 mAh/g and the final specific discharge capacity is only 30 mAh/g. PB-4M with Na-rich content is a very stable PBA especially at high-temperature from the electrochemical performance mentioned above.

PB-A delivers a discharge capacity of 95 mAh/g at 0.2 C and 55 mAh/g at 10 C. In contrast, PB-C gives a high discharge capacity of 112 mAh/g at 0.2 C and 97 mAh/g at 10 C. The ability of PB-C to perform at high current density is due to the high number of exposed active sites and short migration distance of Na^+, leading to enhance ions diffusion rate and electron transfer dynamics. PB-A exposes its problem as it suffers with low-capacity retention of 70 % after 1000 cycles. On the contrary, PB-C shows a capacity

retention of more than 85 % after 1000 cycles. And it is almost no capacity fading from 50^{th} to 1000^{th} cycle. Thus, PB-C with a high surface area can operate in very long cycling.

7.3 Discussion of P2-Type Transition Metal Oxide

In Chapter 6, the focus was on the characterization and electrochemical performance of P2-type TMO materials, specifically NM, LNM, MNM, and LMNM. The key difference among these four samples lies in the substitution of elements.

Figure 6.1 illustrates the XRD patterns of these samples. The NM sample exhibited a pure P2-type structure, as indicated by the characteristic peaks observed below 50°, such as 15.8°, 32.0°, 35.9°, 39.5°, 43.5°, and 48.8°. No other impurity peaks were observed except for the presence of NiO. With the substitution of Li or Mg or both in the P2-type TMO structure, similar characteristic peaks were still observed in the XRD patterns of LNM, MNM, and LMNM samples. However, an additional peak appeared at 18.8° in the LNM sample, indicating the formation of a Li-contained O3 phase. The lattice parameters of each sample also changed, indicating the successful substitution of elements. Electron microscopy images of NM, LNM, MNM, and LMNM did not show any significant changes in morphology.

Overall, the characterization results revealed that the substitution of elements in P2-type TMO materials affected the crystal structure, lattice parameters, and the formation of additional phases. These findings provide valuable insights into the structural modifications achieved through element substitution and lay the foundation for studying the electrochemical performance of these materials.

The LMNM, LNM, MNM and NM show initial discharge capacities of 115 mAh/g, 127 mAh/g, 115 mAh/g and 135 mAh/g, respectively. Nevertheless, the substitution enables improved cycling performance. The NM delivers a specific discharge capacity of

103 mAh/g in the 4th cycle and maintains a specific discharge capacity of only 22 mAh/g after 100 cycles. By contrast, the LMNM, LNM and MNM exhibit capacity retentions of 75%, 77%, and 54%, respectively. Besides, the co-substitutions contribute to enhanced rate capability. LMNM, LNM, MNM and NM deliver discharge capacities of 61 mAh/g, 67 mAh/g, 53 mAh/g and 78 mAh/g at 2 C, respectively.

The introduction of Li doping in the LMNM material has been found to enhance the diffusion coefficient of Na^+ ions, leading to improved rate capabilities. On the other hand, Mg doping primarily serves to stabilize the crystal structure of the LMNM. GITT and CV measurements at various scan rates demonstrated that the substitution of Li in the LMNM resulted in enhanced Na^+ diffusion coefficients. This indicates that the mobility of Na^+ ions within the material is improved, leading to higher rate capabilities. These findings suggest that Li doping can effectively enhance the charge and discharge rates of the LMNM.

Additionally, in-situ X-ray Diffraction (XRD) measurements provided insights into the structural changes occurring during the charge and discharge processes. The results indicated that the substituted samples with Li doping exhibited smaller structural changes compared to the non-doped samples. This suggests that the introduction of Li helps to maintain the structural integrity of the LMNM material during cycling, contributing to its improved stability and long-term performance.

Overall, the combination of Li and Mg doping in the LMNM material offers promising benefits. Li doping enhances the Na^+ ion diffusion coefficient, improving the rate capabilities, while Mg doping contributes to the stabilization of the crystal structure. These findings pave the way for the development of advanced LMNM for high-performance energy storage applications.

7.4 Conclusions

In this study, PBA was synthesized using a precipitation method, with the regulation of its components or morphological modification. P2-type TMO was synthesized using a solid-state method, where elemental substitution was employed to modify the composition. The synthesized PBA and P2-type TMO were then used as cathode materials in SIBs, and their electrochemical performance was investigated. The synthesized PBA and P2-type TMO were then evaluated for their electrochemical performance in SIBs. This involved testing their charge and discharge performance, rate performance, cycling performance, and other relevant electrochemical properties.

A Na-rich PBA cathode material was prepared for SIBs, showing high thermal stability and improved charge/discharge performance at high temperatures and current densities. The high concentration of Na^+ ions reduced vacancies and interstitial water, leading to a nano-particle structure that enhanced Na^+ ion transportation. The PB-4M material exhibited excellent stability and durability, maintaining a specific capacity of 57 mAh/g after 500 cycles at 80 °C, with an efficiency close to 100%. Its lower water content and reduced vacancies contributed to its good thermal stability, preventing reactions with the electrolyte and maintaining stability even at elevated temperatures.

In the second sub-work of PBA, a cage-like porous structure material named PB-C was synthesized using a re-heating and acid-etching method. This process resulted in the formation of uniform PBA cubes and created a porous structure with hollow cavities and reduced water content. PB-C exhibited excellent electrochemical performance due to its large specific surface area, providing more active sites for reactions, with increased pseudocapacitance and the internal cavities facilitating ion diffusion. As a cathode material for sodium-ion batteries, PB-C exhibited promising results. It delivered a specific capacity of 112 mAh/g at a relatively low current rate of 0.2 C. Notably, even at

a high current density of 10 C, no significant specific capacity fading was observed. PB-C also demonstrated excellent cycling performance, with over 85% capacity retention after 1000 cycles, thanks to its unique cage-like structure.

P2-type $Na_{0.67}(Li_{0.5}Mg_{0.5})_{0.1}(Ni_{0.33}Mn_{0.67})_{0.9}O_2$ material was successfully synthesized, leveraging the synergistic effects of Li and Mg ions. Li substitution enhanced Na^+ ion diffusion, improving ion transport and rate capabilities. Mg substitution enhanced cycling stability, mitigating capacity fading over repeated cycles. Co-substitution of Li and Mg resulted in structural changes and improved performance. The synthesized material showed a reversible specific capacity of 86 mAh/g at 5 C with a cutoff voltage of 4.5 V and retained 74% capacity after 200 cycles, demonstrating good cycling stability.

By comparing these three electrode materials for SIBs, it becomes evident that all the strategies employed, including component regulation, surface modification, and element substitution have positive effects on the electrode materials. However, none of these strategies can be considered universally superior in all aspects of overall performance. Each strategy may excel in specific parameters such as high-voltage range cycling performance, high-temperature cycling performance, or long cycling life. Therefore, in material design, the choice of strategy should be aimed at achieving specific objectives based on the desired performance characteristics.

7.5 Future Work

The study of SIBs is still in the beginning stage. We hope we can synthesize the better cathode materials for SIBs and make it commercialization for SIBs. The large-scale synthesis of cathode materials for SIBs should be an interest topic in research or engineering.

Indeed, PBA and P2-type TMO have shown promise as cathode materials for SIBs, despite some limitations in their performance. PBA's long cycling life and stability in extreme conditions make it a suitable candidate for cathodes in energy storage systems for outdoor applications. P2-type TMO, with its high specific capacity and operating voltage, holds potential as a cathode material for high-energy-density applications in portable devices.

The study of SIBs is still in its early stages, and there is a growing interest in synthesizing improved cathode materials for SIBs with the aim of achieving commercialization. Large-scale synthesis of cathode materials for SIBs is an intriguing area of research and engineering. Scaling up the synthesis process and ensuring the reproducibility of the desired properties are essential steps towards realizing the practical application of SIBs.

Efforts to improve the performance of cathode materials for SIBs involve optimizing their specific capacities, enhancing their cycling stability, and expanding their operating voltage ranges. Additionally, the development of cost-effective and environmentally friendly synthesis methods is an important consideration for large-scale production.

Commercializing SIBs holds great potential for various applications, including portable electronic devices, electric vehicles, and energy storage systems. Advancements in cathode materials will play a crucial role in achieving the necessary performance characteristics, such as high energy density, long cycle life, and stability under different operating conditions.

In conclusion, the ongoing research and development of cathode materials for SIBs aim to overcome the current limitations and improve their performance for commercialization. Large-scale synthesis methods, along with advancements in material

design and engineering, will be critical in driving the progress and enabling the widespread adoption of SIBs for various applications.

REFERENCES

Avdeev, M., Mohamed, Z., Ling, C. D., Lu, J., Tamaru, M., Yamada, A., & Barpanda, P. (2013). Magnetic structures of $NaFePO_4$ maricite and triphylite polymorphs for sodium-ion batteries. *Inorganic Chemistry, 52*(15), 8685-8693. doi: https://doi.org/10.1021/ic400870x

Bai, P., He, Y., Zou, X., Zhao, X., Xiong, P., & Xu, Y. (2018). Elucidation of the Sodium-Storage Mechanism in Hard Carbons. *Advanced Energy Materials, 8*(15), 1703217. doi: https://doi.org/10.1002/aenm.201703217

Berthelot, R., Carlier, D., & Delmas, C. (2011). Electrochemical investigation of the P2–NaxCoO2 phase diagram. *Nature Materials, 10*(1), 74-80. doi: https://doi.org/10.1038/nmat2920

Bianchini, M., Brisset, N., Fauth, F., Weill, F., Elkaim, E., Suard, E., . . . Croguennec, L. (2014). $Na_3V_2(PO_4)_2F_3$ Revisited: A High-Resolution Diffraction Study. *Chemistry of Materials, 26*(14), 4238-4247. doi: https://doi.org/10.1021/cm501644g

Bianchini, M., Wang, J., Clément, R., & Ceder, G. (2018). A First-Principles and Experimental Investigation of Nickel Solubility into the P2-Na_xCoO_2 Sodium-Ion Cathode. *Advanced Energy Materials, 8*(26), 1801446. doi: https://doi.org/10.1002/aenm.201801446

Billaud, J., Clément, R. J., Armstrong, A. R., Canales-Vázquez, J., Rozier, P., Grey, C. P., & Bruce, P. G. (2014). β-$NaMnO_2$: a high-performance cathode for sodium-ion batteries. *Journal of the American Chemical Society, 136*(49), 17243-17248. doi: https://doi.org/10.1021/ja509704t.

Bommier, C., Surta, T. W., Dolgos, M., & Ji, X. (2015). New Mechanistic Insights on Na-Ion Storage in Nongraphitizable Carbon. *Nano Letters, 15*(9), 5888-5892. doi: http://doi.org/10.1021/acs.nanolett.5b01969

Braconnier, J.-J., Delmas, C., Fouassier, C., & Hagenmuller, P. (1980). Comportement electrochimique des phases Na_xCoO_{-2}. *Materials Research Bulletin, 15*(12), 1797-1804. doi: https://doi.org/10.1016/0025-5408(80)90199-3

Braconnier, J., Delmas, C., & Hagenmuller, P. (1982). Etude par desintercalation electrochimique des systemes Na_xCrO_2 et Na_xNiO_2. *Materials Research Bulletin, 17*(8), 993-1000. doi: https://doi.org/10.1016/0025-5408(82)90124-6

Brant, W. R., Schmid, S., Du, G., Brand, H. E. A., Pang, W. K., Peterson, V. K., . . . Sharma, N. (2014). In Situ Neutron Powder Diffraction Using Custom-made Lithium-ion Batteries. *Journal of Visualized Experiments*(93), e52284. doi: https://doi.org/doi:10.3791/52284

Buchholz, D., Vaalma, C., Chagas, L. G., & Passerini, S. (2015). Mg-doping for improved long-term cyclability of layered Na-ion cathode materials – The example of P2-type $Na_xMg_{0.11}Mn_{0.89}O_2$. *Journal of Power Sources, 282*, 581-585. doi: https://doi.org/10.1016/j.jpowsour.2015.02.069

Bunaciu, A. A., Udriştioiu, E. g., & Aboul-Enein, H. Y. (2015). X-Ray Diffraction: Instrumentation and Applications. *Critical Reviews in Analytical Chemistry, 45*(4), 289-299. doi: https://doi.org/10.1080/10408347.2014.949616

Buser, H. J., Schwarzenbach, D., Petter, W., & Ludi, A. (1977). The crystal structure of Prussian blue: $Fe_4[Fe(CN)_6]_3$. xH2O. *Inorganic Chemistry, 16*(11), 2704-2710. doi: http://doi.org/10.1021/ic50177a008

Cabana, J., Monconduit, L., Larcher, D., & Palacín, M. R. (2010). Beyond Intercalation-Based Li-Ion Batteries: The State of the Art and Challenges of Electrode Materials Reacting Through Conversion Reactions. *Advanced Energy Materials, 22*(35), E170-E192. doi: http://doi.org/10.1002/adma.201000717

Cao, M.-H., Wang, Y., Shadike, Z., Yue, J.-L., Hu, E., Bak, S.-M., . . . Fu, Z.-W. (2017). Suppressing the chromium disproportionation reaction in O3-type layered cathode materials for high capacity sodium-ion batteries. *Journal of Materials Chemistry A, 5*(11), 5442-5448. doi: https://doi.org/10.1039/C6TA10818K

Cao, X., Li, H., Qiao, Y., Li, X., Jia, M., Cabana, J., & Zhou, H. (2020). Stabilizing Reversible Oxygen Redox Chemistry in Layered Oxides for Sodium-Ion Batteries. *Advanced Energy Materials, 10*(15), 1903785. doi: https://doi.org/10.1002/aenm.201903785

Cao, Y., Xiao, L., Sushko, M. L., Wang, W., Schwenzer, B., Xiao, J., . . . Liu, J. (2012). Sodium ion insertion in hollow carbon nanowires for battery applications. *Nano Letters, 12*(7), 3783-3787. doi: https://doi.org/10.1021/nl3016957

Carlier, D., Cheng, J., Berthelot, R., Guignard, M., Yoncheva, M., Stoyanova, R., . . . Delmas, C. (2011). The P2-$Na_{2/3}Co_{2/3}Mn_{1/3}O_2$ phase: structure, physical properties and electrochemical behavior as positive electrode in sodium battery. *Dalton Transactions, 40*(36), 9306-9312. doi: https://doi.org/10.1039/C1DT10798D

Castillo-Martínez, E., Carretero-González, J., & Armand, M. (2014). Polymeric Schiff Bases as Low-Voltage Redox Centers for Sodium-Ion Batteries. *Angewandte Chemie International Edition, 53*(21), 5341-5345. doi: https://doi.org/10.1002/anie.201402402

Chen, B., Zhang, H., Xuan, J., Offer, G. J., & Wang, H. (2020). Seeing is Believing: In Situ/Operando Optical Microscopy for Probing Electrochemical Energy Systems. *Advanced Materials Technologies, 5*(10), 2000555. doi: https://doi.org/10.1002/admt.202000555

Chen, C., Han, Z., Liang, C., Feng, Y., Wang, P., & Wei, W. (2022). Electrochemically induced cleavage cracking at twin boundary of sodium layered oxide cathodes. *Acta Materialia, 238*, 118212. doi: https://doi.org/10.1016/j.actamat.2022.118212

Chen, T., Ouyang, B., Fan, X., Zhou, W., Liu, W., & Liu, K. (2022). Oxide cathodes for sodium-ion batteries: Designs, challenges, and perspectives. *Carbon Energy, 4*(2), 170-199. doi: https://doi.org/10.1002/cey2.153

Chen, Y., Woo, H. J., Rizwan, M., Yahya, R. b., Cui, D., Luo, D., . . . Wang, F. (2019). Nanoscale Morphology Control of Na-Rich Prussian Blue Cathode Materials for Sodium Ion Batteries with Good Thermal Stability. *ACS Applied Energy Materials, 2*(12), 8570-8579. doi: https://doi.org/10.1021/acsaem.9b01491

Cheng, F., Liang, J., Tao, Z., & Chen, J. (2011). Functional materials for rechargeable batteries. *Advanced Materials, 23*(15), 1695-1715. doi: https://doi.org/10.1002/adma.201003587

Cheng, X.-B., Zhang, R., Zhao, C.-Z., & Zhang, Q. (2017). Toward Safe Lithium Metal Anode in Rechargeable Batteries: A Review. *Chemical Reviews, 117*(15), 10403-10473. doi: https://doi.org/10.1021/acs.chemrev.7b00115

Cheng, X.-B., Zhao, C.-Z., Yao, Y.-X., Liu, H., & Zhang, Q. (2019). Recent Advances in Energy Chemistry between Solid-State Electrolyte and Safe Lithium-Metal Anodes. *Chem, 5*(1), 74-96. doi: https://doi.org/10.1016/j.chempr.2018.12.002

Cheng, Z., Zhao, B., Guo, Y.-J., Yu, L., Yuan, B., Hua, W., . . . Guo, Y.-G. (2022). Mitigating the Large-Volume Phase Transition of P2-Type Cathodes by Synergetic Effect of Multiple Ions for Improved Sodium-Ion Batteries. *Advanced Energy Materials, 12*(14), 2103461. doi: https://doi.org/10.1002/aenm.202103461

Chevrier, V. L., & Ceder, G. (2011). Challenges for Na-ion negative electrodes. *Journal of the Electrochemical Society, 158*(9), A1011-A1014. doi: https://doi.org/10.1149/1.3607983

Cölfen, H., & Mann, S. (2003). Higher-Order Organization by Mesoscale Self-Assembly and Transformation of Hybrid Nanostructures. *Angewandte Chemie International Edition, 42*(21), 2350-2365. doi: https://doi.org/10.1002/anie.200200562

Dai, K., Wu, J., Zhuo, Z., Li, Q., Sallis, S., Mao, J., . . . Yang, W. (2019). High Reversibility of Lattice Oxygen Redox Quantified by Direct Bulk Probes of Both Anionic and Cationic Redox Reactions. *Joule, 3*(2), 518-541. doi: https://doi.org/10.1016/j.joule.2018.11.014

Dang, C., Mu, Q., Xie, X., Sun, X., Yang, X., Zhang, Y., . . . Hou, C. (2022). Recent progress in cathode catalyst for nonaqueous lithium oxygen batteries: a review. *Advanced Composites and Hybrid Materials, 5*(2), 606-626. doi: https://doi.org/10.1007/s42114-022-00500-8

Darbar, D., Malkowski, T., Self, E. C., Bhattacharya, I., Venkatesh, M., Reddy, V., & Nanda, J. (2022). An overview of cobalt-free, nickel-containing cathodes for Li-ion batteries. *Materials Today Energy*, 101173. doi: https://doi.org/10.1016/j.mtener.2022.101173

Darwiche, A., Marino, C., Sougrati, M. T., Fraisse, B., Stievano, L., & Monconduit, L. (2012). Better Cycling Performances of Bulk Sb in Na-Ion Batteries Compared to Li-Ion Systems: An Unexpected Electrochemical Mechanism. *Journal of the American Chemical Society, 134*(51), 20805-20811. doi: https://doi.org/10.1021/ja310347x

Delmas, C. (2018). Sodium and Sodium-Ion Batteries: 50 Years of Research. *Advanced Energy Materials, 8*(17), 1703137. doi: https://doi.org/10.1002/aenm.201703137

Delmas, C., Braconnier, J.-J., Fouassier, C., & Hagenmuller, P. (1981). Electrochemical intercalation of sodium in NaxCoO$_2$ bronzes. *Solid State Ionics, 3*, 165-169.

Delmas, C., Cherkaoui, F., Nadiri, A., & Hagenmuller, P. (1987). A nasicon-type phase as intercalation electrode: NaTi$_2$(PO$_4$)$_3$. *Materials Research Bulletin, 22*(5), 631-639. doi: https://doi.org/10.1016/0025-5408(87)90112-7

Delmas, C., Fouassier, C., & Hagenmuller, P. (1980). Structural classification and properties of the layered oxides. *Physica B+C, 99*(1), 81-85. doi: https://doi.org/10.1016/0378-4363(80)90214-4

Didier, C., Guignard, M., Denage, C., Szajwaj, O., Ito, S., Saadoune, I., . . . Delmas, C. (2011). Electrochemical Na-Deintercalation from NaVO$_2$. *Electrochemical and Solid-State Letters, 14*(5), A75-A78.

Dreyer, S. L., Kondrakov, A., Janek, J., & Brezesinski, T. (2022). In situ analysis of gas evolution in liquid- and solid-electrolyte-based batteries with current and next-generation cathode materials. *Journal of Materials Research*, 3146-3168. doi: https://doi.org/10.1557/s43578-022-00586-2

Ellis, L. D., Hatchard, T. D., & Obrovac, M. N. (2012). Reversible Insertion of Sodium in Tin. *Journal of the Electrochemical Society, 159*(11), A1801. doi: https://doi.org/10.1149/2.037211jes

Fadley, C. S. (2010). X-ray photoelectron spectroscopy: Progress and perspectives. *Journal of Electron Spectroscopy and Related Phenomena, 178-179*, 2-32. doi: https://doi.org/10.1016/j.elspec.2010.01.006

Farina, A., Piergallini, R., Doldo, A., Salsano, E. P., & Abballe, F. (1991). The determination of C-H-N by an automated elemental analyzer. *Microchemical Journal, 43*(3), 181-190. doi: https://doi.org/10.1016/S0026-265X(10)80003-7

Feng, J., Luo, S.-h., Wang, J., Li, P., Yan, S., Li, J., . . . Liu, X. (2022). Stable Electrochemical Properties of Magnesium-Doped Co-Free Layered P2-Type Na$_{0.67}$Ni$_{0.33}$Mn$_{0.67}$O$_2$ Cathode Material for Sodium Ion Batteries. *ACS Sustainable Chemistry & Engineering, 10*(15), 4994-5004. doi: http://doi:10.1021/acssuschemeng.2c00197

Fouassier, C., Matejka, G., Reau, J.-M., & Hagenmuller, P. (1973). Sur de nouveaux bronzes oxygénés de formule Na$_x$CoO$_2$ ($x \leqslant 1$). Le système cobalt-oxygène-sodium. *Journal of Solid State Chemistry, 6*(4), 532-537. doi: https://doi.org/10.1016/S0022-4596(73)80011-8

Gao, J., Chen, Y., Meng, F., Ding, M., Weng, L., Xu, G., & He, X. (2022). Research on in-situ optical microscopic observation in lithium-ion batteries. *Energy Storage Science and Technology, 11*(1), 53-59. doi: https://doi.org/10.19799/j.cnki.2095-4239.2021.0212

Gao, L., Chen, J., Chen, Q., & Kong, X. (2022). The chemical evolution of solid electrolyte interface in sodium metal batteries. *Science Advances, 8*(6), eabm4606. doi: https://doi.org/doi:10.1126/sciadv.abm4606

Gao, Y., Zhang, H., Liu, X.-H., Yang, Z., He, X.-X., Li, L., . . . Chou, S.-L. (2021). Low-Cost Polyanion-Type Sulfate Cathode for Sodium-Ion Battery. *Advanced Energy Materials, 11*(42), 2101751. doi: https://doi.org/10.1002/aenm.202101751

Gonzalo, E., Zarrabeitia, M., Drewett, N. E., López del Amo, J. M., & Rojo, T. (2021). Sodium manganese-rich layered oxides: Potential candidates as positive electrode for Sodium-ion batteries. *Energy Storage Materials, 34*, 682-707. doi: https://doi.org/10.1016/j.ensm.2020.10.010

Gopalakrishnan, R., Goutam, S., Oliveira, L. M., Timmermans, J.-M., Omar, N., Messagie, M., . . . van Mierlo, J. (2016). A Comprehensive Study on Rechargeable Energy Storage Technologies. *Journal of Electrochemical Energy Conversion and Storage, 13*(4), 040801. doi: http://doi.org/10.1115/1.4036000

Grey, C. P., & Dupré, N. (2004). NMR Studies of Cathode Materials for Lithium-Ion Rechargeable Batteries. *Chemical Reviews, 104*(10), 4493-4512. doi: https://doi.org/10.1021/cr020734p

Guo, S., Sun, Y., Yi, J., Zhu, K., Liu, P., Zhu, Y., . . . Zhou, H. (2016). Understanding sodium-ion diffusion in layered P2 and P3 oxides via experiments and first-principles calculations: a bridge between crystal structure and electrochemical performance. *Npg Asia Materials, 8*, e266. doi: https://doi.org/0.1038/am.2016.53

Guo, Y., Li, H., & Zhai, T. (2017). Reviving Lithium-Metal Anodes for Next-Generation High-Energy Batteries. *Advanced Materials, 29*(29), 1700007. doi: http://doi.org/10.1002/adma.201700007

Guyomard, D., & Tarascon, J.-M. (1994). Rocking-chair or lithium-ion rechargeable lithium batteries. *Advanced Materials, 6*(5), 408-412. doi: http://doi.org/10.1002/adma.19940060516

Han, L., Yu, X.-Y., & Lou, X. W. (2016). Formation of Prussian-Blue-Analog Nanocages via a Direct Etching Method and their Conversion into Ni–Co-Mixed Oxide for Enhanced Oxygen Evolution. *Advanced Materials, 28*(23), 4601-4605. doi: https://doi.org/10.1002/adma.201506315

Han, M. H., Acebedo, B., Gonzalo, E., Fontecoba, P. S., Clarke, S., Saurel, D., & Rojo, T. (2015). Synthesis and Electrochemistry Study of P2- and O3-phase $Na_{2/3}Fe_{1/2}Mn_{1/2}O_2$. *Electrochimica Acta, 182*, 1029-1036. doi: https://doi.org/10.1016/j.electacta.2015.10.003

Han, M. H., Gonzalo, E., Casas-Cabanas, M., & Rojo, T. (2014). Structural evolution and electrochemistry of monoclinic $NaNiO_2$ upon the first cycling process. *Journal of Power Sources, 258*, 266-271. doi: https://doi.org/10.1016/j.jpowsour.2014.02.048

Han, X. G., Gong, Y. H., Fu, K., He, X. F., Hitz, G. T., Dai, J. Q., . . . Hu, L. B. (2017). Negating interfacial impedance in garnet-based solid-state Li metal batteries. *Nature Materials, 16*(5), 572–579. doi: http://doi.org/10.1038/Nmat4821

Hartmann, P., Bender, C. L., Vračar, M., Dürr, A. K., Garsuch, A., Janek, J., & Adelhelm, P. (2013). A rechargeable room-temperature sodium superoxide (NaO_2) battery. *Nature Materials, 12*(3), 228-232. doi: https://doi.org/10.1038/nmat3486

Hassanzadeh, N., & Sadrnezhaad, S. K. (2021). Magnetic stirring assisted hydrothermal synthesis of $Na_3MnCO_3PO_4$ cathode material for sodium-ion battery. *Ceramics International, 47*(19), 26929-26934. doi: https://doi.org/10.1016/j.ceramint.2021.06.104

Heber, M., Hofmann, K., & Hess, C. (2022). Raman Diagnostics of Cathode Materials for Li-Ion Batteries Using Multi-Wavelength Excitation. *Batteries, 8*(2), 10. doi: https://doi.org/10.3390/batteries8020010

Hou, D., Gabriel, E., Graff, K., Li, T., Ren, Y., Wang, Z., . . . Xiong, H. (2022). Thermal dynamics of P2-$Na_{0.67}Ni_{0.33}Mn_{0.67}O_2$ cathode materials for sodium ion batteries studied by in situ analysis. *Journal of Materials Research, 37*(6), 1156-1163. doi: https://doi.org/10.1557/s43578-022-00519-z

Hou, D., Xia, D., Gabriel, E., Russell, J. A., Graff, K., Ren, Y., . . . Xiong, H. (2021). Spatial and Temporal Analysis of Sodium-Ion Batteries. *ACS Energy Letters, 6*(11), 4023-4054. doi: https://doi.org/10.1021/acsenergylett.1c01868

Hovington, P., Timoshevskii, V., Burgess, S., Demers, H., Statham, P., Gauvin, R., & Zaghib, K. (2016). Can we detect Li K X-ray in lithium compounds using energy dispersive spectroscopy? *Scanning, 38*(6), 571-578. doi: https://doi.org/10.1002/sca.21302

Hu, H., Tang, K., Cao, S., Yang, X., & Wang, X. (2021). Synthesis and electrochemical properties of P2–$Na_{2/3}[Ni_{1/3}Mn_{2/3}]O_2$ microspheres as cathode materials for sodium-ion batteries. *Journal of Alloys and Compounds, 859*, 157768. doi: https://doi.org/10.1016/j.jallcom.2020.157768

Hu, M., Furukawa, S., Ohtani, R., Sukegawa, H., Nemoto, Y., Reboul, J., . . . Yamauchi, Y. (2012). Synthesis of Prussian Blue Nanoparticles with a Hollow Interior by Controlled Chemical Etching. *Angewandte Chemie International Edition, 51*(4), 984-988. doi: https://doi.org/10.1002/anie.201105190

Hu, M., Jiang, J.-S., Lin, C.-C., & Zeng, Y. (2010). Prussian blue mesocrystals: an example of self-construction. *CrystEngComm, 12*(10), 2679-2683. doi: https://doi.org/10.1039/C003523H

Huangfu, C., Liu, Z., Lu, X., Liu, Q., Wei, T., & Fan, Z. (2021). Strong oxidation induced quinone-rich dopamine polymerization onto porous carbons as ultrahigh-capacity organic cathode for sodium-ion batteries. *Energy Storage Materials, 43*, 120-129. doi: https://doi.org/10.1016/j.ensm.2021.08.043

Hwang, J.-Y., Myung, S.-T., & Sun, Y.-K. (2017). Sodium-ion batteries: present and future. *Chemical Society Reviews*, 3529-3614. doi: https://doi.org/10.1039/C6CS00776G

Irisarri, E., Ponrouch, A., & Palacin, M. R. (2015). Review—Hard Carbon Negative Electrode Materials for Sodium-Ion Batteries. *Journal of the Electrochemical Society, 162*(14), A2476. doi: http://doi:10.1002/10.1149/2.0091514jes

Isayev, A. I. (2010). *Encyclopedia of Polymer Blends, Volume 1: Fundamentals*: John Wiley & Sons.

Jian, Z., Han, W., Lu, X., Yang, H., Hu, Y. S., Zhou, J., . . . Chen, D. (2013). Superior Electrochemical Performance and Storage Mechanism of $Na_3V_2(PO_4)_3$ Cathode for Room‐Temperature Sodium‐Ion Batteries. *Advanced Energy Materials, 3*(2), 156-160. doi: https://doi.org/10.1002/aenm.201200558

Jiang, W., Qi, W., Pan, Q., Jia, Q., Yang, C., & Cao, B. (2021). Potassium ions stabilized hollow Mn-based prussian blue analogue nanocubes as cathode for high performance sodium ions battery. *International Journal of Hydrogen Energy, 46*(5), 4252-4258. doi: https://doi.org/10.1016/j.ijhydene.2020.10.260

Kerman, K., Luntz, A., Viswanathan, V., Chiang, Y.-M., & Chen, Z. (2017). Review—Practical Challenges Hindering the Development of Solid State Li Ion Batteries. *Journal of the Electrochemical Society, 164*(7), A1731-A1744. doi: http://doi.org/10.1149/2.1571707jes

King, P., Ramsey, M., McMillan, P., & Swayze, G. (2004). Laboratory Fourier transform infrared spectroscopy methods for geologic samples. In *Infrared Spectroscopy in Geochemistry, Exploration, and Remote Sensing* (Vol. 33, pp. 57-91).

Kobayashi, T., Zhao, W., Rajendra, H. B., Yamanaka, K., Ohta, T., & Yabuuchi, N. (2019). Nanosize Cation-Disordered Rocksalt Oxides: Na_2TiO_3-$NaMnO_2$ Binary System. *Small*, e1902462. doi: https://doi.org/10.1002/smll.201902462

Komaba, S., Nakayama, T., Ogata, A., Shimizu, T., Takei, C., Takada, S., . . . Nakai, I. (2009). Electrochemically reversible sodium intercalation of layered $NaNi_{0.5}Mn_{0.5}O_2$ and $NaCrO_2$. *ECS Transactions, 16*(42), 43-55. doi: https://doi.org/10.1149/1.3112727

Kubota, K., Asari, T., Yoshida, H., Yaabuuchi, N., Shiiba, H., Nakayama, M., & Komaba, S. (2016). Understanding the structural evolution and redox mechanism of a $NaFeO_2$ – $NaCoO_2$ solid solution for sodium‐ion batteries. *Advanced Functional Materials, 26*(33), 6047-6059. doi: https://doi.org/10.1002/adfm.201601292

Kuwata, N., Matsuda, Y., Okawa, T., Hasegawa, G., Kamishima, O., & Kawamura, J. (2022). Ion dynamics of the $Li_xMn_2O_4$ cathode in thin-film solid-state batteries revealed by in situ Raman spectroscopy. *Solid State Ionics, 380*, 115925. doi: https://doi.org/10.1016/j.ssi.2022.115925

Lacey, S. D., Wan, J., Cresce, A. v. W., Russell, S. M., Dai, J., Bao, W., . . . Hu, L. (2015). Atomic Force Microscopy Studies on Molybdenum Disulfide Flakes as Sodium-

Ion Anodes. *Nano Letters, 15*(2), 1018-1024. doi: https://doi.org/10.1021/nl503871s

Law, M., & Balaya, P. (2018). $NaVPO_4F$ with high cycling stability as a promising cathode for sodium-ion battery. *Energy Storage Materials, 10*, 102-113. doi: https://doi.org/10.1016/j.ensm.2017.08.007

Lee, H.-W., Wang, R. Y., Pasta, M., Lee, S. W., Liu, N., & Cui, Y. (2014). Manganese hexacyanomanganate open framework as a high-capacity positive electrode material for sodium-ion batteries. *Nature Communications, 5*, 5280.

Lee, M., Hong, J., Lopez, J., Sun, Y., Feng, D., Lim, K., . . . Bao, Z. (2017). High-performance sodium–organic battery by realizing four-sodium storage in disodium rhodizonate. *Nature Energy, 2*, 861-868. doi: https://doi.org/10.1038/s41560-017-0014-y

Lee, W., Muhammad, S., Sergey, C., Lee, H., Yoon, J., Kang, Y. M., & Yoon, W. S. (2020). Advances in the Cathode Materials for Lithium Rechargeable Batteries. *Angewandte Chemie-International Edition, 59*(7), 2578-2605. doi: http://doi.org/10.1002/anie.201902359

Lei, Z.-Q., Guo, Y.-J., Wang, E.-H., He, W.-H., Zhang, Y.-Y., Xin, S., . . . Guo, Y.-G. (2022). Layered Oxide Cathode-Electrolyte Interface towards Na-Ion Batteries: Advances and Perspectives. *Chemistry – An Asian Journal, 17*(12), e202200213. doi: https://doi.org/10.1002/asia.202200213

Li, J., Ji, Y., Song, H., Chen, S., Ding, S., Zhang, B., . . . Pan, F. (2022). Insights Into the Interfacial Degradation of High-Voltage All-Solid-State Lithium Batteries. *Nano-Micro Letters, 14*(1), 191. doi: https://doi.org/10.1007/s40820-022-00936-z

Li, J., Risthaus, T., Wang, J., Zhou, D., He, X., Ehteshami, N., . . . Li, J. (2020). The effect of Sn substitution on the structure and oxygen activity of $Na_{0.67}Ni_{0.33}Mn_{0.67}O_2$ cathode materials for sodium ion batteries. *Journal of Power Sources, 449*, 227554. doi: https://doi.org/10.1016/j.jpowsour.2019.227554

Li, J., Wang, J., He, X., Zhang, L., Senyshyn, A., Yan, B., . . . Li, J. (2019). P2 – Type $Na_{0.67}Mn_{0.8}Cu_{0.1}Mg_{0.1}O_2$ as a new cathode material for sodium-ion batteries: Insights of the synergetic effects of multi-metal substitution and electrolyte optimization. *Journal of Power Sources, 416*, 184-192. doi: https://doi.org/10.1016/j.jpowsour.2019.01.086

Li, L., Nie, P., Chen, Y., & Wang, J. (2019). Novel acetic acid induced Na-rich Prussian blue nanocubes with iron defects as cathodes for sodium ion batteries. *Journal of Materials Chemistry A, 7*(19), 12134-12144. doi: http://doi.org/10.1039/C9TA01965K

Li, S., Dong, Y., Xu, L., Xu, X., He, L., & Mai, L. (2014). Effect of carbon matrix dimensions on the electrochemical properties of $Na_3V_2(PO_4)_3$ nanograins for high‐performance symmetric sodium‐ion batteries. *Advanced Materials, 26*(21), 3545-3553. doi: https://doi.org/10.1002/adma.201305522

Li, W.-J., Chou, S.-L., Wang, J.-Z., Kang, Y.-M., Wang, J.-L., Liu, Y., . . . Dou, S.-X. (2015). Facile Method To Synthesize Na-Enriched $Na_{1+x}FeFe(CN)_6$ Frameworks as Cathode with Superior Electrochemical Performance for Sodium-Ion Batteries. *Chemistry of Materials, 27*(6), 1997-2003. doi: https://doi.org/10.1021/cm504091z

Li, X., Wu, D., Zhou, Y.-N., Liu, L., Yang, X.-Q., & Ceder, G. (2014). O3-type $Na(Mn_{0.25}Fe{=}Co_{0.25}Ni_{0.25})O_2$: A quaternary layered cathode compound for rechargeable Na ion batteries. *Electrochemistry Communications, 49*, 51-54. doi: https://doi.org/10.1016/j.elecom.2014.10.003

Li, Y., Hu, Y.-S., Titirici, M.-M., Chen, L., & Huang, X. (2016). Hard Carbon Microtubes Made from Renewable Cotton as High-Performance Anode Material for Sodium-Ion Batteries. *Advanced Energy Materials, 6*(18), 1600659. doi: https://doi.org/10.1002/aenm.201600659

Li, Y., Wu, F., Li, Y., Liu, M., Feng, X., Bai, Y., & Wu, C. (2022). Ether-based electrolytes for sodium ion batteries. *Chemical Society Reviews, 51*(11), 4484-4536. doi: http://doi.org/10.1039/D1CS00948F

Li, Z.-Y., Ma, X., Sun, K., He, L., Li, Y., & Chen, D. (2022). $Na_{2/3}Li_{1/9}[Ni_{2/9}Li_{1/9}Mn_{2/3}]O_2$: A High-Performance Solid-Solution Reaction Layered Oxide Cathode Material for Sodium-Ion Batteries. *ACS Applied Energy Materials, 5*(1), 1126-1135. doi: http://doi:10.1021/acsaem.1c03483

Li, Z., Zhang, Y., Zhang, J., Cao, Y., Chen, J., Liu, H., & Wang, Y. (2022). Sodium-Ion Battery with a Wide Operation-Temperature Range from −70 to 100 °C. *Angewandte Chemie International Edition, 61*(13), e202116930. doi: https://doi.org/10.1002/anie.202116930

Lin, C.-C., Liu, H.-Y., Kang, J.-W., Yang, C.-C., Li, C.-H., Chen, H.-Y. T., . . . Chen, H.-Y. (2022). In-situ X-ray studies of high-entropy layered oxide cathode for sodium-ion batteries. *Energy Storage Materials, 51*, 159-171. doi: https://doi.org/10.1016/j.ensm.2022.06.035

Liu, B., Zhang, J.-G., & Xu, W. (2018). Advancing Lithium Metal Batteries. *Joule, 2*(5), 833-845. doi: https://doi.org/10.1016/j.joule.2018.03.008

Liu, J., Didier, C., Sale, M., Sharma, N., Guo, Z., Peterson, V. K., & Ling, C. D. (2020). Elucidation of the high-voltage phase in the layered sodium ion battery cathode material P3–$Na_{0.5}Ni_{0.25}Mn_{0.75}O_2$. *Journal of Materials Chemistry A, 8*(40), 21151-21162. doi: https://doi.org/10.1039/D0TA06600A

Liu, M., & Li, X. (2022). Mechanical properties measurement of materials and devices at micro- and nano-scale by optical methods: A review. *Optics and Lasers in Engineering, 150*, 106853. doi: https://doi.org/10.1016/j.optlaseng.2021.106853

Liu, Q., Hu, Z., Chen, M., Zou, C., Jin, H., Wang, S., . . . Dou, S.-X. (2020). The Cathode Choice for Commercialization of Sodium-Ion Batteries: Layered Transition Metal Oxides versus Prussian Blue Analogs. *Advanced Functional Materials, 30*(14), 1909530. doi: https://doi.org/10.1002/adfm.201909530

Liu, Y., Qiao, Y., Zhang, W., Li, Z., Ji, X., Miao, L., . . . Huang, Y. (2015). Sodium storage in Na-rich NaxFeFe(CN)$_6$ nanocubes. *Nano Energy, 12*, 386-393. doi: https://doi.org/10.1016/j.nanoen.2015.01.012

Liu, Y., Shen, Q., Zhao, X., Zhang, J., Liu, X., Wang, T., . . . Fan, L. Z. (2019). Hierarchical Engineering of Porous P2 - $Na_{2/3}Ni_{1/3}Mn_{2/3}O_2$ Nanofibers Assembled by Nanoparticles Enables Superior Sodium - Ion Storage Cathodes. *Advanced Functional Materials, 30*(6), 1907837. doi: https://doi.org/10.1002/adfm.201907837

Liu, Z., Hu, Y.-Y., Dunstan, M. T., Huo, H., Hao, X., Zou, H., . . . Grey, C. P. (2014). Local structure and dynamics in the Na ion battery positive electrode material $Na_3V_2(PO_4)_2F_3$. *Chemistry of Materials, 26*(8), 2513-2521. doi: https://doi.org/10.1021/cm403728w

Lu, Y., Wang, L., Cheng, J., & Goodenough, J. B. (2012). Prussian blue: a new framework of electrode materials for sodium batteries. *Chemical Communications (Cambridge, United Kingdom), 48*(52), 6544-6546. doi: https://doi.org/10.1039/c2cc31777j

Lu, Z., & Dahn, J. R. (2001). In Situ X-Ray Diffraction Study of P2-$Na_{2/3}[Ni_{1/3}Mn_{2/3}]O_2$. *Journal of the Electrochemical Society, 148*(11), A1225. doi: http://doi.org/10.1149/1.1407247

Lu, Z., Donaberger, R. A., & Dahn, J. R. (2000). Superlattice Ordering of Mn, Ni, and Co in Layered Alkali Transition Metal Oxides with P2, P3, and O3 Structures. *Chemistry of Materials, 12*(12), 3583-3590. doi: http://doi:10.1021/cm000359m

Ma, C., Alvarado, J., Xu, J., Clément, R. J., Kodur, M., Tong, W., . . . Meng, Y. S. (2017). Exploring Oxygen Activity in the High Energy P2-Type $Na_{0.78}Ni_{0.23}Mn_{0.69}O_2$ Cathode Material for Na-Ion Batteries. *Journal of the American Chemical Society, 139*(13), 4835-4845. doi: http://doi:10.1021/jacs.7b00164

Ma, X., Chen, H., & Ceder, G. (2011). Electrochemical Properties of Monoclinic $NaMnO_2$. *Journal of the Electrochemical Society, 158*(12), A1307. doi: https://doi.org/10.1149/2.035112jes

Maeda, Y., Kitta, M., & Kuratani, K. (2022). Microscopic electrochemical analysis of all-solid-state Li-ion batteries using conductive atomic force microscopy as a nano current collector probe. *Japanese Journal of Applied Physics, 61*(SL), SL1002. doi: https://doi.org/10.35848/1347-4065/ac665e

Marbella, L. E., Evans, M. L., Groh, M. F., Nelson, J., Griffith, K. J., Morris, A. J., & Grey, C. P. (2018). Sodiation and Desodiation via Helical Phosphorus Intermediates in High-Capacity Anodes for Sodium-Ion Batteries. *Journal of the American Chemical Society, 140*(25), 7994-8004. doi: https://doi.org/10.1021/jacs.8b04183

Megahed, S., & Scrosati, B. (1994). Lithium-ion rechargeable batteries. *Journal of Power Sources, 51*(1), 79-104. doi: https://doi.org/10.1016/0378-7753(94)01956-8

Meinshausen, M., Meinshausen, N., Hare, W., Raper, S. C., Frieler, K., Knutti, R., . . . Allen, M. R. (2009). Greenhouse-gas emission targets for limiting global warming to 2 ℃ . [41.577]. *Nature, 458*(7242), 1158-1162. doi: https://doi.org/10.1038/nature08017

Moreau, P., Guyomard, D., Gaubicher, J., & Boucher, F. (2010). Structure and Stability of Sodium Intercalated Phases in Olivine FePO4. *Chemistry of Materials, 22*(14), 4126-4128. doi: 10.1021/cm101377h

Mu, L., Ben, L., Hu, Y.-S., Li, H., Chen, L., & Huang, X. (2016). Novel 1.5 V anode materials, $ATiOPO_4$ (A = NH4, K, Na), for room-temperature sodium-ion batteries. *Journal of Materials Chemistry A, 4*(19), 7141-7147. doi: https://doi.org/10.1039/C6TA00891G

Mu, L., Xu, S., Li, Y., Hu, Y. S., Li, H., Chen, L., & Huang, X. (2015). Prototype sodium‐ion batteries using an air‐stable and Co/Ni‐free O3‐layered metal oxide cathode. *Advanced Materials, 27*(43), 6928-6933. doi: https://doi.org/10.1002/adma.201502449

Naderi, M. (2015). Chapter Fourteen - Surface Area: Brunauer–Emmett–Teller (BET). In S. Tarleton (Ed.), *Progress in Filtration and Separation* (pp. 585-608). Oxford: Academic Press.

Nagpure, S. C., Downing, R. G., Bhushan, B., Babu, S. S., & Cao, L. (2011). Neutron depth profiling technique for studying aging in Li-ion batteries. *Electrochimica Acta, 56*(13), 4735-4743. doi: https://doi.org/10.1016/j.electacta.2011.02.037

Nanba, Y., Iwao, T., Boisse, B. M. d., Zhao, W., Hosono, E., Asakura, D., . . . Harada, Y. (2016). Redox potential paradox in Na_xMO_2 for sodium-ion battery cathodes. *Chemistry of Materials, 28*(4), 1058-1065. doi: https://doi.org/10.1021/acs.chemmater.5b04289

Ng, C., Ding, J., & Gan, L. (2001). Microstructural changes induced by thermal treatment of cobalt (II) hexacyanoferrate (III) compound. *Journal of Solid State Chemistry, 156*(2), 400-407. doi: http://doi.org/10.1006/jssc.2000.9013

Ni, Q., Bai, Y., Wu, F., & Wu, C. (2017). Polyanion-Type Electrode Materials for Sodium-Ion Batteries. *Advanced Science, 4*(3), 1600275. doi: https://doi.org/10.1002/advs.201600275

Niu, Y., Xu, M., Shen, B., Dai, C., & Li, C. M. (2016). Exploration of $Na_7Fe_{4.5}(P_2O_7)_4$ as a cathode material for sodium-ion batteries. *Journal of Materials Chemistry A, 4*(42), 16531-16535. doi: http://doi.org/10.1039/C6TA05780B

Oh, S.-M., Myung, S.-T., Hassoun, J., Scrosati, B., & Sun, Y.-K. (2012). Reversible NaFePO4 electrode for sodium secondary batteries. *Electrochemistry Communications, 22*, 149-152. doi: https://doi.org/10.1016/j.elecom.2012.06.014

Olesik, J. W. (1991). Elemental Analysis Using ICP-OES and ICP/MS. *Analytical Chemistry, 63*(1), 12A-21A. doi: https://doi.org/10.1021/ac00001a711

Pan, H., Lu, X., Yu, X., Hu, Y.-S., Li, H., Yang, X.-Q., & Chen, L. (2013). Sodium Storage and Transport Properties in Layered Na2Ti$_3$O$_7$ for Room-Temperature Sodium-Ion Batteries. *Advanced Energy Materials, 3*(9), 1186-1194. doi: https://doi.org/10.1002/aenm.201300139

Pavan, A. F., & Ling, C. D. (2022). Phase Formation and Degradation of Na_2ZrO_3 under CO_2 Cycling Studied by Ex Situ and In Situ Diffraction. *Inorganic Chemistry, 61*(17), 6555-6561. doi: https://doi.org/10.1021/acs.inorgchem.2c00384

Pecher, O., Carretero-González, J., Griffith, K. J., & Grey, C. P. (2017). Materials' Methods: NMR in Battery Research. *Chemistry of Materials, 29*(1), 213-242. doi: https://doi.org/10.1021/acs.chemmater.6b03183

Pei, Q., Lu, M., Liu, Z., Li, D., Rao, X., Liu, X., & Zhong, S. (2022). Improving the $Na_{0.67}Ni_{0.33}Mn_{0.67}O_2$ Cathode Material for High-Voltage Cyclability via Ti/Cu Codoping for Sodium-Ion Batteries. *ACS Applied Energy Materials, 5*(2), 1953-1962. doi: http://doi:10.1021/acsaem.1c03466

Peng, B., Chen, Y., Wang, F., Sun, Z., Zhao, L., Zhang, X., . . . Zhang, G. (2022). Unusual Site-Selective Doping in Layered Cathode Strengthens Electrostatic Cohesion of Alkali-Metal Layer for Practicable Sodium-Ion Full Cell. *Advanced Materials, 34*(6), 2103210. doi: https://doi.org/10.1002/adma.202103210

Piernas-Muñoz, M. J., Castillo-Martínez, E., Gómez-Cámer, J., & Rojo, T. (2016). Optimizing the electrolyte and binder composition for Sodium Prussian Blue, $Na_{1-x}Fe_{x+(1/3)}(CN)_6 \cdot yH_2O$, as cathode in sodium ion batteries. *Electrochimica Acta, 200*, 123-130. doi: https://doi.org/10.1016/j.electacta.2016.02.188

Qi, X., Wu, L., Li, Z., Xiang, Y., Liu, Y., Huang, K., . . . Zhang, X. (2022). Superstructure Variation and Improved Cycling of Anion Redox Active Sodium Manganese Oxides Due to Doping by Iron. *Advanced Energy Materials, n/a*(n/a), 2202355. doi: https://doi.org/10.1002/aenm.202202355

Qi, Y., Tong, Z., Zhao, J., Ma, L., Wu, T., Liu, H., . . . Hu, Y.-S. (2018). Scalable Room-Temperature Synthesis of Multi-shelled $Na_3(VOPO_4)_2F$ Microsphere Cathodes. *Joule, 2*(11), 2348-2363. doi: https://doi.org/10.1016/j.joule.2018.07.027

Qian, J., Wu, C., Cao, Y., Ma, Z., Huang, Y., Ai, X., & Yang, H. (2018). Prussian Blue Cathode Materials for Sodium-Ion Batteries and Other Ion Batteries. *Advanced Energy Materials, 8*(17), 1702619. doi: https://doi.org/10.1002/aenm.201702619

Qiu, S., Xiao, L., Sushko, M. L., Han, K. S., Shao, Y., Yan, M., . . . Liu, J. (2017). Manipulating Adsorption–Insertion Mechanisms in Nanostructured Carbon Materials for High-Efficiency Sodium Ion Storage. *Advanced Energy Materials, 7*(17), 1700403. doi: https://doi.org/10.1002/aenm.201700403

Ren, H., Li, Y., Ni, Q., Bai, Y., Zhao, H., & Wu, C. (2022). Unraveling Anionic Redox for Sodium Layered Oxide Cathodes: Breakthroughs and Perspectives. *Advanced Materials, 34*(8), 2106171. doi: https://doi.org/10.1002/adma.202106171

Rinaldo, Raccichini, Alberto, Varzi, Stefano, Passerini, . . . Scrosati. (2015). The role of graphene for electrochemical energy storage. *Nature Materials*, 271-279. doi: https://doi.org/10.1038/nmat4170

Risthaus, T., Zhou, D., Cao, X., He, X., Qiu, B., Wang, J., . . . Li, J. (2018). A high-capacity P2 $Na_{2/3}Ni_{1/3}Mn_{2/3}O_{-2}$ cathode material for sodium ion batteries with oxygen activity. *Journal of Power Sources, 395*, 16-24. doi: https://doi.org/10.1016/j.jpowsour.2018.05.026

Roberts, S., Chen, L., Kishore, B., Dancer, C. E. J., Simmons, M. J. H., & Kendrick, E. (2022). Mechanism of gelation in high nickel content cathode slurries for sodium-ion batteries. *Journal of Colloid and Interface Science, 627*, 427-437. doi: https://doi.org/10.1016/j.jcis.2022.07.033

Rong, X., Hu, E., Lu, Y., Meng, F., Zhao, C., Wang, X., . . . Chen, L. (2019). Anionic Redox Reaction-Induced High-Capacity and Low-Strain Cathode with Suppressed Phase Transition. *Joule, 3*(2), 503-517. doi: https://doi.org/10.1016/j.joule.2018.10.022

Rong, X., Liu, J., Hu, E., Liu, Y., Wang, Y., Wu, J., . . . Huang, X. (2018). Structure-Induced Reversible Anionic Redox Activity in Na Layered Oxide Cathode. *Joule, 2*(1), 125-140. doi: https://doi.org/10.1016/j.joule.2017.10.008

Rozier, P., Sathiya, M., Paulraj, A.-R., Foix, D., Desaunay, T., Taberna, P.-L., . . . Tarascon, J.-M. (2015). Anionic redox chemistry in Na-rich $Na_2Ru_{1-y}Sn_yO_3$ positive electrode material for Na-ion batteries. *Electrochemistry Communications, 53*, 29-32. doi: https://doi.org/10.1016/j.elecom.2015.02.001

Saadatkhah, N., Carillo Garcia, A., Ackermann, S., Leclerc, P., Latifi, M., Samih, S., . . . Chaouki, J. (2020). Experimental methods in chemical engineering: Thermogravimetric analysis—TGA. *The Canadian Journal of Chemical Engineering, 98*(1), 34-43. doi: https://doi.org/10.1002/cjce.23673

Saadoune, I., Maazaz, A., Menetrier, M., & Delmas, C. (1996). On the $Na_xNi_{0.6}Co_{0.4}o_2$ system: physical and electrochemical studies. *Journal of Solid State Chemistry, 122*(1), 111-117. doi: https://doi.org/10.1006/jssc.1996.0090

Senguttuvan, P., Rousse, G., Seznec, V., Tarascon, J.-M., & Palacín, M. R. (2011). $Na_2Ti_3O_7$: Lowest Voltage Ever Reported Oxide Insertion Electrode for Sodium Ion Batteries. *Chemistry of Materials, 23*(18), 4109-4111. doi: https://doi.org/10.1021/cm202076g

Senthilkumar, B., Johnson, C. S., & Senguttuvan, P. (2022). Layered Na-Ion Transition-Metal Oxide Electrodes for Sodium-Ion Batteries. In *Transition Metal Oxides for Electrochemical Energy Storage* (pp. 101-119).

Shadike, Z., Zhao, E., Zhou, Y.-N., Yu, X., Yang, Y., Hu, E., . . . Yang, X.-Q. (2018). Advanced Characterization Techniques for Sodium-Ion Battery Studies. *Advanced Energy Materials, 8*(17), 1702588. doi: https://doi.org/10.1002/aenm.201702588

Shen, Q., Liu, Y., Jiao, L., Qu, X., & Chen, J. (2021). Current state-of-the-art characterization techniques for probing the layered oxide cathode materials of sodium-ion batteries. *Energy Storage Materials, 35*, 400-430. doi: https://doi.org/10.1016/j.ensm.2020.11.002

Shen, X., Wu, S., Liu, Y., Wang, K., Xu, Z., & Liu, W. (2009). Morphology syntheses and properties of well-defined Prussian blue nanocrystals by a facile solution approach. *Journal of Colloid and Interface Science, 329*(1), 188-195. doi: https://doi.org/10.1016/j.jcis.2008.09.067

Shi, C., Wang, L., Chen, X. a., Li, J., Wang, S., Wang, J., & Jin, H. (2022). Challenges of layer-structured cathodes for sodium-ion batteries. *Nanoscale Horizons, 7*(4), 338-351. doi: https://doi.org/10.1039/D1NH00585E

Shraer, S. D., Luchinin, N. D., Trussov, I. A., Aksyonov, D. A., Morozov, A. V., Ryazantsev, S. V., . . . Fedotov, S. S. (2022). Development of vanadium-based polyanion positive electrode active materials for high-voltage sodium-based batteries. *Nature Communications, 13*(1), 4097. doi: https://doi.org/10.1038/s41467-022-31768-5

Šić, E., Melzi d'Eril, M., Schutjajew, K., Graczyk-Zajac, M. J., Breitzke, H., Riedel, R., . . . Buntkowsky, G. (2022). SiCN Ceramics as Electrode Materials for Sodium/Sodium Ion Cells – Insights from 23Na In-Situ Solid-State NMR. *Batteries & Supercaps, 5*(7), e202200066. doi: https://doi.org/10.1002/batt.202200066

Skoog, D. A., Holler, F. J., & Crouch, S. R. (2007). *Instrumental analysis* (Vol. 47): Brooks/Cole, Cengage Learning Belmont.

Somerville, J. W., Sobkowiak, A., Tapia-Ruiz, N., Billaud, J., Lozano, J. G., House, R. A., . . . Bruce, P. G. (2019). Nature of the "Z"-phase in layered Na-ion battery cathodes. *Energy & Environmental Science, 12*(7), 2223-2232. doi: https://doi.org/10.1039/C8EE02991A

Song, J., Wang, L., Lu, Y., Liu, J., Guo, B., Xiao, P., . . . Goodenough, J. B. (2015). Removal of interstitial H_2O in hexacyanometallates for a superior cathode of a sodium-ion battery. *Journal of the American Chemical Society, 137*(7), 2658-2664. doi: http://doi.org/10.1021/ja512383b

Stevens, D. A., & Dahn, J. R. (2000). High Capacity Anode Materials for Rechargeable Sodium - Ion Batteries. *Journal of the Electrochemical Society, 147*(4), 1271. doi: https://dx.doi.org/10.1149/1.1393348

Sun, J., Xue, W., Zhang, L., Dai, L., Bi, J., Yao, F., . . . Zhu, J. (2022). Gradient Supramolecular Preorganization Endows the Derived N/P Dual-Doped Carbon Nanosheets with Tunable Storage Performance toward Sodium-Ion Batteries. *Industrial & Engineering Chemistry Research, 61*(20), 6997-7008. doi: https://doi.org/10.1021/acs.iecr.2c00878

Syed Mohd Fadzil, S. A. F., Woo, H. J., Azzahari, A. D., Winie, T., & Kufian, M. Z. (2023). Sodium-rich prussian blue analogue coated by poly(3,4-ethylenedioxythiophene) polystyrene sulfonate as superior cathode for sodium-

ion batteries. *Materials Today Chemistry, 30*, 101540. doi: https://doi.org/10.1016/j.mtchem.2023.101540

Takeda, Y., Nakahara, K., Nishijima, M., Imanishi, N., Yamamoto, O., Takano, M., & Kanno, R. (1994). Sodium deintercalation from sodium iron oxide. *Materials Research Bulletin, 29*(6), 659-666. doi: https://doi.org/10.1016/0025-5408(94)90122-8

Tan, X., Mo, R., Xu, J., Li, X., Yin, Q., Shen, L., & Lu, Y. (2022). High Performance Sodium Ion Anodes Based on Sn_4P_3 Encapsulated within Amphiphilic Graphene Tubes. *Advanced Energy Materials, 12*(2), 2102345. doi: https://doi.org/10.1002/aenm.202102345

Tapia-Ruiz, N., Dose, W. M., Sharma, N., Chen, H., Heath, J., Somerville, J. W., . . . Bruce, P. G. (2018). High voltage structural evolution and enhanced Na-ion diffusion in P2-$Na_{2/3}Ni_{1/3-x}Mg_xMn_{2/3}O_2$ ($0 \leqslant x \leqslant 0.2$) cathodes from diffraction, electrochemical and ab initio studies. *Energy & Environmental Science, 11*(6), 1470-1479. doi: http://doi.org/10.1039/C7EE02995K

Tarascon, J., & Hull, G. (1986). Sodium intercalation into the layer oxides $Na_xMo_2O_4$. *Solid State Ionics, 22*(1), 85-96. doi: https://doi.org/10.1016/0167-2738(86)90062-7

Tian, H., Shao, H., Chen, Y., Fang, X., Xiong, P., Sun, B., . . . Wang, G. (2019). Ultra-stable sodium metal-iodine batteries enabled by an in-situ solid electrolyte interphase. *Nano Energy, 57*, 692-702. doi: https://doi.org/10.1016/j.nanoen.2018.12.084

Urtubia, A., Pérez-correa, J. R., Pizarro, F., & Agosin, E. (2008). Exploring the applicability of MIR spectroscopy to detect early indications of wine fermentation problems. *Food Control, 19*(4), 382-388. doi: https://doi.org/10.1016/j.foodcont.2007.04.017

Vanaphuti, P., Yao, Z., Liu, Y., Lin, Y., Wen, J., Yang, Z., . . . Wang, Y. (2022). Achieving High Stability and Performance in P2-Type Mn-Based Layered Oxides with Tetravalent Cations for Sodium-Ion Batteries. *Small, 18*(19), 2201086. doi: https://doi.org/10.1002/smll.202201086

Wang, B., Han, Y., Wang, X., Bahlawane, N., Pan, H., Yan, M., & Jiang, Y. (2018). Prussian Blue Analogs for Rechargeable Batteries. *iScience, 3*, 110-133. doi: https://doi.org/10.1016/j.isci.2018.04.008

Wang, C., Liu, L., Zhao, S., Liu, Y., Yang, Y., Yu, H., . . . Chen, J. (2021). Tuning local chemistry of P2 layered-oxide cathode for high energy and long cycles of sodium-ion battery. *Nature Communications, 12*(1), 2256. doi: https://doi.org/10.1038/s41467-021-22523-3

Wang, C., Wang, R., Huang, Z., Chu, M., Ji, W., Chen, Z., . . . Xiao, Y. (2022). Unveiling the migration behavior of lithium ions in NCM/Graphite full cell via in operando neutron diffraction. *Energy Storage Materials, 44*, 1-9. doi: https://doi.org/10.1016/j.ensm.2021.09.032

Wang, H., Liu, F., Yu, R., & Wu, J. (2022). Unraveling the reaction mechanisms of electrode materials for sodium-ion and potassium-ion batteries by in situ transmission electron microscopy. *Interdisciplinary Materials, 1*(2), 196-212. doi: https://doi.org/10.1002/idm2.12008

Wang, J., He, X., Zhou, D., Schappacher, F., Zhang, X., Liu, H., . . . Sofy, M. S. (2016). O3-type $Na[Fe_{1/3}Ni_{1/3}Ti_{1/3}]O_2$ cathode material for rechargeable sodium ion batteries. *Journal of Materials Chemistry A, 4*(9), 3431-3437. doi: https://doi.org/10.1039/C5TA10520J

Wang, K., Xu, Y., Li, Y., Dravid, V., Wu, J., & Huang, Y. (2019). Sodium storage in hard carbon with curved graphene platelets as the basic structural units. *Journal of Materials Chemistry A, 7*(7), 3327-3335. doi: https://doi.org/10.1039/C8TA11510A

Wang, L., Song, J., Qiao, R., Wray, L. A., Hossain, M. A., Chuang, Y.-D., . . . Lee, J.-J. (2015). Rhombohedral Prussian white as cathode for rechargeable sodium-ion batteries. *Journal of the American Chemical Society, 137*(7), 2548-2554. doi: https://doi.org/10.1021/ja510347s

Wang, Q., Madsen, A., Owen, J. R., & Weller, M. T. (2013). Direct hydrofluorothermal synthesis of sodium transition metal fluorosulfates as possible Na-ion battery cathode materials. *Chemical Communications (Cambridge, United Kingdom), 49*(21), 2121-2123. doi: https://doi.org/10.1039/C3CC38897B

Wang, S., Li, H., Zhang, W., Zheng, J., Li, S., Hu, J., . . . Zhang, Z. (2021). Ultra-High-Rate $Na_3V(PO_3)_3N$ Cathode with Superior Stability for Fast-Charging Sodium-Ion Batteries. *ACS Applied Energy Materials, 4*(9), 10136-10144. doi: https://doi.org/10.1021/acsaem.1c02042

Wang, W., Gang, Y., Hu, Z., Yan, Z., Li, W., Li, Y., . . . Dou, S.-X. (2020). Reversible structural evolution of sodium-rich rhombohedral Prussian blue for sodium-ion batteries. *Nature Communications, 11*(1), 980. doi: https://doi.org/10.1038/s41467-020-14444-4

Wang, Y., Xiao, R., Hu, Y.-S., Avdeev, M., & Chen, L. (2015). P2-$Na_{0.6}[Cr_{0.6}Ti_{0.4}]O_2$ cation-disordered electrode for high-rate symmetric rechargeable sodium-ion batteries. *Nature Communications, 6*(1), 6954. doi: https://doi.org/10.1038/ncomms7954

Wang, Y., Yu, X., Xu, S., Bai, J., Xiao, R., Hu, Y.-S., . . . Huang, X. (2013). A zero-strain layered metal oxide as the negative electrode for long-life sodium-ion batteries. *Nature Communications, 4*(1), 2365. doi: https://doi.org/10.1038/ncomms3365

Wei, X., Wang, X., An, Q., Han, C., & Mai, L. (2017). Operando X-ray Diffraction Characterization for Understanding the Intrinsic Electrochemical Mechanism in Rechargeable Battery Materials. *Small Methods, 1*(5), 1700083. doi: https://doi.org/10.1002/smtd.201700083

Whiteside, A., Fisher, C. A., Parker, S. C., & Islam, M. S. (2014). Particle shapes and surface structures of olivine $NaFePO_4$ in comparison to $LiFePO_4$. *Physical*

Chemistry Chemical Physics, 16(39), 21788-21794. doi: https://doi.org/10.1021/nl3016957

Wilde, R. E., Ghosh, S. N., & Marshall, B. J. (1970). Prussian blues. *Inorganic Chemistry, 9*(11), 2512-2516. doi: https://doi.org/10.1021/ic50093a027

Winter, M., Barnett, B., & Xu, K. (2018). Before Li Ion Batteries. *Chemical Reviews, 118*(23), 11433-11456. doi: http://doi.org/10.1021/acs.chemrev.8b00422

Wood, V. (2018). X-ray tomography for battery research and development. *Nature Reviews Materials, 3*(9), 293-295. doi: https://doi.org/10.1038/s41578-018-0053-4

Wu, D., Li, X., Xu, B., Twu, N., Liu, L., & Ceder, G. (2015). $NaTiO_2$: a layered anode material for sodium-ion batteries. *Energy & Environmental Science, 8*(1), 195-202. doi: https://doi.org/10.1039/C4EE03045A

Wu, X., Deng, W., Qian, J., Cao, Y., Ai, X., & Yang, H. (2013). Single-crystal $FeFe(CN)_6$ nanoparticles: a high capacity and high rate cathode for Na-ion batteries. *Journal of Materials Chemistry A, 1*(35), 10130-10134. doi: http://doi.org/10.1039/c3ta12036h

Wu, X., Ma, J., Ma, Q., Xu, S., Hu, Y.-S., Sun, Y., . . . Huang, X. (2015). A spray drying approach for the synthesis of a $Na_2C_6H_2O_4$/CNT nanocomposite anode for sodium-ion batteries. *Journal of Materials Chemistry A, 3*(25), 13193-13197. doi: http://doi:10.1002/10.1039/C5TA03192C

Wu, X., Wu, C., Wei, C., Hu, L., Qian, J., Cao, Y., . . . Yang, H. (2016). Highly Crystallized $Na_2CoFe(CN)_6$ with Suppressed Lattice Defects as Superior Cathode Material for Sodium-Ion Batteries. *ACS Applied Materials & Interfaces, 8*(8), 5393-5399. doi: http://doi.org/10.1021/acsami.5b12620

Xia, F., Tie, D., Wang, J., Song, H., Wen, W., Ye, X., . . . Zhao, Y. (2021). Ultrahigh rate and durable sodium-ion storage at a wide potential window via lanthanide doping and perovskite surface decoration on layered manganese oxides. *Energy Storage Materials, 42*, 209-218. doi: https://doi.org/10.1016/j.ensm.2021.07.020

Xiao, J., Gao, H., Tang, K., Long, M., Chen, J., Liu, H., & Wang, G. (2022). Manipulating Stable Layered P2-Type Cathode via a Co-Substitution Strategy for High Performance Sodium Ion Batteries. *Small Methods, 6*(3), 2101292. doi: https://doi.org/10.1002/smtd.202101292

Xu, G.-L., Liu, X., Zhou, X., Zhao, C., Hwang, I., Daali, A., . . . Amine, K. (2022). Native lattice strain induced structural earthquake in sodium layered oxide cathodes. *Nature Communications, 13*(1), 436. doi: https://doi.org/10.1038/s41467-022-28052-x

Xu, J., Lee, D. H., Clément, R. J., Yu, X., Leskes, M., Pell, A. J., . . . Meng, Y. S. (2014). Identifying the Critical Role of Li Substitution in P2–$Na_x[Li_yNi_zMn_{1-y-z}]O_2$ ($0<x, y, z<1$) Intercalation Cathode Materials for High-Energy Na-Ion Batteries. *Chemistry of Materials, 26*(2), 1260-1269. doi: https://doi.org/10.1021/cm403855t

Xu, Y., Chang, M., Fang, C., Liu, Y., Qiu, Y., Ou, M., . . . Huang, Y. (2019). In Situ FTIR-Assisted Synthesis of Nickel Hexacyanoferrate Cathodes for Long-Life Sodium-Ion Batteries. *ACS Applied Materials & Interfaces, 11*(33), 29985-29992. doi: http://doi.org/10.1021/acsami.9b10312

Yabuuchi, N., Kajiyama, M., Iwatate, J., Nishikawa, H., Hitomi, S., Okuyama, R., . . . Komaba, S. (2012). P2-type $Na_x[Fe_{1/2}Mn_{1/2}]O_2$ mP2-type Nax[Fe1/2Mn1/2]O2 made from earth-abundant elements for rechargeable Na batteriesbatteries. *Nature Materials, 11*(6), 512-517. doi: https://doi.org/10.1038/nmat3309

Yabuuchi, N., Kubota, K., Dahbi, M., & Komaba, S. (2014). Research development on sodium-ion batteries. *Chemical Reviews, 114*(23), 11636-11682. doi: https://doi.org/10.1021/cr500192f

Yan, X., Yang, Y., Liu, E., Sun, L., Wang, H., Liao, X.-Z., . . . Ma, Z.-F. (2017). Improved cycling performance of prussian blue cathode for sodium ion batteries by controlling operation voltage range. *Electrochimica Acta, 225*, 235-242. doi: https://doi.org/10.1016/j.electacta.2016.12.121

Yang, C., Xin, S., Mai, L. Q., & You, Y. (2021). Materials Design for High-Safety Sodium-Ion Battery. *Advanced Energy Materials, 11*(2), 2000974. doi: https://doi.org/10.1002/aenm.202000974

Yang, D., Xu, J., Liao, X.-Z., Wang, H., He, Y.-S., & Ma, Z.-F. (2015). Prussian blue without coordinated water as a superior cathode for sodium-ion batteries. *Chemical Communications (Cambridge, United Kingdom), 51*(38), 8181-8184. doi: https://doi.org/10.1039/C5CC01180A

Yang, L., del Amo, J. M. L., Shadike, Z., Bak, S.-M., Bonilla, F., Galceran, M., . . . Adelhelm, P. (2020). A Co- and Ni-Free P2/O3 Biphasic Lithium Stabilized Layered Oxide for Sodium-Ion Batteries and its Cycling Behavior. *Advanced Functional Materials, 30*(42), 2003364. doi: https://doi.org/10.1002/adfm.202003364

Yang, L., Kuo, L.-Y., López del Amo, J. M., Nayak, P. K., Mazzio, K. A., Maletti, S., . . . Adelhelm, P. (2021). Structural Aspects of P2-Type $Na_{0.67}Mn_{0.6}Ni_{0.2}Li_{0.2}O_2$ (MNL) Stabilization by Lithium Defects as a Cathode Material for Sodium-Ion Batteries. *Advanced Functional Materials, 31*(38), 2102939. doi: https://doi.org/10.1002/adfm.202102939

Yang, L., Luo, S.-h., Wang, Y., Zhan, Y., Wang, Q., Zhang, Y., . . . Teng, F. (2021). Cu-doped layered P2-type $Na_{0.67}Ni_{0.33-x}Cu_xMn_{0.67}O_2$ cathode electrode material with enhanced electrochemical performance for sodium-ion batteries. *Chemical Engineering Journal, 404*, 126578. doi: https://doi.org/10.1016/j.cej.2020.126578

Yang, X., & Rogach, A. L. (2020). Anodes and Sodium-Free Cathodes in Sodium Ion Batteries. *Advanced Energy Materials, 10*(22), 2000288. doi: https://doi.org/10.1002/aenm.202000288

Yoshida, H., Yabuuchi, N., & Komaba, S. (2013). $NaFe_{0.5}Co_{0.5}O_2$ as high energy and power positive electrode for Na-ion batteries. *Electrochemistry Communications, 34*, 60-63. doi: https://doi.org/10.1016/j.elecom.2013.05.012

Yoshida, H., Yabuuchi, N., Kubota, K., Ikeuchi, I., Garsuch, A., Schulz-Dobrick, M., & Komaba, S. (2014). P2-type $Na_{2/3}Ni_{1/3}Mn_{2/3-x}TixO_2$ as a new positive electrode for higher energy Na-ion batteries. *Chemical Communications (Cambridge, United Kingdom), 50*(28), 3677-3680. doi: http://doi.org/10.1039/c3cc49856e

You, Y., Wu, X.-L., Yin, Y.-X., & Guo, Y.-G. (2014). High-quality Prussian blue crystals as superior cathode materials for room-temperature sodium-ion batteries. *Energy & Environmental Science, 7*(5), 1643-1647. doi: https://doi.org/10.1039/C3EE44004D

You, Y., Yu, X., Yin, Y., Nam, K.-W., & Guo, Y.-G. (2015). Sodium iron hexacyanoferrate with high Na content as a Na-rich cathode material for Na-ion batteries. *Nano Research, 8*(1), 117-128. doi: https://doi.org/10.1007/s12274-014-0588-7

Yousaf, M., Naseer, U., Imran, A., Li, Y., Aftab, W., Mahmood, A., . . . Jiang, Y. (2022). Visualization of battery materials and their interfaces/interphases using cryogenic electron microscopy. *Materials Today, 58*, 238-274. doi: https://doi.org/10.1016/j.mattod.2022.06.022

Zakaria, M. B., & Chikyow, T. (2017). Recent advances in Prussian blue and Prussian blue analogues: synthesis and thermal treatments. *Coordination Chemistry Reviews, 352*, 328-345. doi: https://doi.org/10.1016/j.ccr.2017.09.014

Zeng, X., Li, M., Abd El-Hady, D., Alshitari, W., Al-Bogami, A. S., Lu, J., & Amine, K. (2019). Commercialization of Lithium Battery Technologies for Electric Vehicles. *Advanced Energy Materials, 9*(27), 1900161. doi: http://doi.org/10.1002/aenm.201900161

Zhang, F., Liao, J., Xu, L., Wu, W., & Wu, X. (2021). Stabilizing P2-Type Ni–Mn Oxides as High-Voltage Cathodes by a Doping-Integrated Coating Strategy Based on Zinc for Sodium-Ion Batteries. *ACS Applied Materials & Interfaces, 13*(34), 40695-40704. doi: http://doi:10.1021/acsami.1c12062

Zhang, L., Tsolakidou, C., Mariyappan, S., Tarascon, J.-M., & Trabesinger, S. (2021). Unraveling gas evolution in sodium batteries by online electrochemical mass spectrometry. *Energy Storage Materials, 42*, 12-21. doi: https://doi.org/10.1016/j.ensm.2021.07.005

Zhang, L., Wang, J., Schuck, G., Xi, F., Du, L., Winter, M., . . . Li, J. (2020). Stabilizing P3-Type Oxides as Cathodes for High-Rate and Long-Life Sodium Ion Batteries by Disordered Distribution of Transition Metals. *Small Methods, 4*(10), 2000422. doi: https://doi.org/10.1002/smtd.202000422

Zhang, T., Ji, H., Hou, X., Ji, W., Fang, H., Huang, Z., . . . Xiao, Y. (2022). Promoting the performances of P2-type sodium layered cathode by inducing Na site rearrangement. *Nano Energy, 100*, 107482. doi: https://doi.org/10.1016/j.nanoen.2022.107482

Zhang, W. Y., Zhao, Y. G., Guo, Z. P., Qiao, P. T., Cui, L., Luo, L. B., . . . Li, J. Q. (2005). Effect of Ti doping on the electrical transport and magnetic properties of

layered compound $Na_{0.8}CoO_2$. *Solid State Communications, 135*(8), 480-484. doi: https://doi.org/10.1016/j.ssc.2005.05.047

Zhao, B., Ran, R., Liu, M., & Shao, Z. (2015). A comprehensive review of $Li_4Ti_5O_{12}$-based electrodes for lithium-ion batteries: The latest advancements and future perspectives. *Materials Science and Engineering: R: Reports, 98*, 1-71. doi: https://doi.org/10.1016/j.mser.2015.10.001

Zhao, C., Ding, F., Lu, Y., Chen, L., & Hu, Y.-S. (2020). High-Entropy Layered Oxide Cathodes for Sodium-Ion Batteries. *Angewandte Chemie International Edition, 59*(1), 264-269. doi: https://doi.org/10.1002/anie.201912171

Zhao, C., Liu, L., Qi, X., Lu, Y., Wu, F., Zhao, J., . . . Chen, L. (2018). Solid‐State Sodium Batteries. *Advanced Energy Materials*, 1703012. doi: http://doi.org/10.1002/aenm.201703012

Zhao, C., Wang, Q., Lu, Y., Hu, Y.-S., Li, B., & Chen, L. (2017). Review on anionic redox for high-capacity lithium- and sodium-ion batteries. *Journal of Physics D: Applied Physics, 50*(18), 183001. doi: https://doi.org/10.1088/1361-6463/aa646d

Zhao, C., Wang, Q., Yao, Z., Wang, J., Sánchez-Lengeling, B., Ding, F., . . . Hu, Y.-S. (2020). Rational design of layered oxide materials for sodium-ion batteries. *Science, 370*(6517), 708-711. doi: https://doi.org/10.1126/science.aay9972

Zhao, J., Zhou, G., Yan, K., Xie, J., Li, Y., Liao, L., . . . Cui, Y. (2017). Air-stable and freestanding lithium alloy/graphene foil as an alternative to lithium metal anodes. *Nature Nanotechnology, 12*, 993. doi: http://doi:10.1002/10.1038/nnano.2017.129

Zhao, L., Pan, H.-L., Hu, Y.-S., Li, H., & Chen, L.-Q. (2012). Spinel lithium titanate ($Li_4Ti_5O_{12}$) as novel anode material for room-temperature sodium-ion battery. *Chinese Physics B, 21*(2), 028201.

Zhao, L., Zhao, J., Hu, Y.-S., Li, H., Zhou, Z., Armand, M., & Chen, L. (2012). Disodium Terephthalate ($Na_2C_8H_4O_4$) as High Performance Anode Material for Low-Cost Room-Temperature Sodium-Ion Battery. *Advanced Energy Materials, 2*(8), 962-965. doi: https://doi.org/10.1002/aenm.201200166

Zhao, Q., Lu, Y., & Chen, J. (2016). Advanced Organic Electrode Materials for Rechargeable Sodium‐Ion Batteries. *Advanced Energy Materials*, 1601792. doi: https://doi.org/10.1002/aenm.201601792Citations

Zhao, W., Kirie, H., Tanaka, A., Unno, M., Yamamoto, S., & Noguchi, H. (2014). Synthesis of metal ion substituted P2-$Na_{2/3}Ni_{1/3}Mn_{2/3}O_2$ cathode material with enhanced performance for Na ion batteries. *Materials Letters, 135*(Complete), 131-134. doi: https://doi.org/10.1016/j.matlet.2014.07.153

Zhou, A., Cheng, W., Wang, W., Zhao, Q., Xie, J., Zhang, W., . . . Li, J. (2020). Hexacyanoferrate-Type Prussian Blue Analogs: Principles and Advances Toward High-Performance Sodium and Potassium Ion Batteries. *Advanced Energy Materials, n/a*(n/a), 2000943. doi: https://doi.org/10.1002/aenm.202000943

Zhou, D., Wang, J., Liu, X., He, X., Sun, F., Murzin, V., . . . Li, J. (2020). Operando X-ray absorption spectroscopy investigations on $NaxNi_{1/3}Fe_{1/3}Mn_{1/3}O_2$ positive electrode materials for sodium and sodium ion batteries. *Journal of Power Sources, 473*, 228557. doi: https://doi.org/10.1016/j.jpowsour.2020.228557

Zhou, W., Li, Y., Xin, S., & Goodenough, J. B. (2017). Rechargeable Sodium All-Solid-State Battery. *ACS Central Science, 3*(1), 52-57. doi: http://doi.org/10.1021/acscentsci.6b00321

Zhu, R., Liu, C., Feng, J., & Guo, Z. (2018). In Situ Observation of Lithium Dendrite of Different Graphite Electrodes. *ECS Transactions, 85*(13), 347. doi: https://doi.org/10.1149/08513.0347ecst

Zuo, W., Qiu, J., Liu, X., Ren, F., Liu, H., He, H., . . . Yang, Y. (2020). The stability of P2-layered sodium transition metal oxides in ambient atmospheres. *Nature Communications, 11*(1), 3544. doi: https://doi.org/10.1038/s41467-020-17290-6